

BOSTON UNIVERSITY  
GRADUATE SCHOOL OF ARTS AND SCIENCES

Dissertation

**A PRECISION MEASUREMENT OF THE TOP QUARK MASS**

by

**KEVIN MATTHEW BLACK**

B.A., Wesleyan University, 1999

M.A., Boston University, 2001

Submitted in partial fulfillment of the  
requirements for the degree of  
Doctor of Philosophy

2005

Approved by

First Reader

---

Meenakshi Narain, Ph.D.  
Associate Professor of Physics

Second Reader

---

Ulrich Heintz, Ph.D.  
Associate Professor of Physics

## Acknowledgments

ACKNOWLEDGEMENTS GO HERE

# A PRECISION MEASUREMENT OF THE TOP QUARK MASS

(Order No.           )

KEVIN MATTHEW BLACK

Boston University Graduate School of Arts and Sciences, 2005

Major Professor: Meenakshi Narain, Associate Professor of Physics

## ABSTRACT

This dissertation describes the measurement of the top quark mass using events recorded during a  $\approx 230 \text{ pb}^{-1}$  exposure of the DØ detector to proton-anti-proton collisions at a center of mass energy of 1.96 TeV. The Standard Model of particle physics predicts that the top quark will decay into a bottom quark and a W boson close to 100% of the time. The bottom quark will hadronize (bind with another quark) and produce a jet of hadronic particles. The W bosons can decay either into a charged lepton and a neutrino or a pair of quarks. This dissertation focuses on the top quark events in which one W decays hadronically and the other decays leptonically. Two methods of identifying top quark events from the large number of events produced are used. The first is based on the unique topology of the final state particles of a heavy particle. By using the topological information of the event, the top events can be efficiently extracted from the background. The second method relies on the identification of the remnants of the long lived bottom quarks that are expected to be produced in the decay of almost every top quark. Because the largest background processes do not contain bottom quarks, this is an extremely efficient way to select the events retaining about 60% of the top quark events and removing almost 90% of the background. A kinematic fit to the top quark mass is performed on the top quark candidate events using the final state particles that are seen in the detector.

A likelihood technique is then used to extract the most likely value of the top quark mass and signal fraction. The result for the topological selection is  $m_{top} = 169.9 \pm 5.8$  (statistical)  $+8.0 -7.8$  (systematic) GeV while the results on the sample selected from identification of a b quark in the event is  $m_{top} = 170.6 \pm 4.2$  (statistical)  $+6.3 -6.8$  (systematic).

# Contents

<b>1</b>	<b>INTRODUCTION</b>	<b>1</b>
<b>2</b>	<b>PHENOMENOLOGY AND MOTIVATION</b>	<b>4</b>
2.1	A Brief Review of the Standard Model . . . . .	4
2.2	The Role of the Top Quark Mass in the Standard Model . . . . .	9
2.3	The Role of the Top Quark Mass Beyond the Standard Model . . . . .	15
2.3.1	Supersymmetry . . . . .	16
2.3.2	New Top Strong Interactions . . . . .	17
2.4	Top Production at the Tevatron . . . . .	18
2.5	Top Quark Decay . . . . .	20
2.6	Lepton + Jets Mode . . . . .	22
2.7	Previous Top Quark Measurements . . . . .	24
<b>3</b>	<b>EXPERIMENTAL APPARATUS</b>	<b>27</b>
3.1	Accelerator . . . . .	27
3.2	Overview of the DØ Detector . . . . .	30
3.3	Coordinate System . . . . .	32

3.4	Central Tracking . . . . .	35
3.4.1	Silicon Micro-strip Tracker . . . . .	35
3.4.2	Central Fiber Tracker . . . . .	39
3.4.3	Solenoid . . . . .	40
3.4.4	Forward and Central Pre-showers . . . . .	41
3.5	The Calorimeter . . . . .	43
3.6	Muon Detectors . . . . .	46
3.6.1	Drift Tubes . . . . .	48
3.6.2	Scintillators . . . . .	51
3.7	Triggering . . . . .	51
3.7.1	Trigger Architecture . . . . .	51
3.7.2	L1 Trigger Elements . . . . .	53
3.7.3	L2 Trigger Overview . . . . .	54
3.7.4	The Silicon Track Trigger . . . . .	55
3.7.5	Level 3 Trigger and Data Acquisition System . . . . .	61
<b>4</b>	<b>EVENT RECONSTRUCTION</b>	<b>63</b>
4.1	Central Tracking Reconstruction . . . . .	63
4.1.1	Clustering . . . . .	64
4.1.2	Tracking . . . . .	65
4.2	Calorimeter Reconstruction . . . . .	68
4.3	Muon Reconstruction . . . . .	69
4.3.1	Hit Finding . . . . .	70
4.3.2	Segment Finding . . . . .	70
4.3.3	Track Fitting . . . . .	71
4.4	Primary Vertex Reconstruction . . . . .	72

4.5	Particle Identification . . . . .	73
4.5.1	Electrons . . . . .	73
4.5.2	Muon Identification . . . . .	80
4.6	Jet Identification . . . . .	81
4.6.1	Jet Reconstruction . . . . .	81
4.6.2	Jet Selection . . . . .	83
4.6.3	Jet Energy Scale . . . . .	84
4.6.4	Jet Energy Resolution . . . . .	86
4.7	Missing Transverse Momentum . . . . .	87
4.8	Secondary Verticies . . . . .	88
<b>5</b>	<b>EVENT SIMULATION</b>	<b>91</b>
5.1	Introduction . . . . .	91
5.2	Simulated Signal . . . . .	92
5.3	Simulated Background . . . . .	93
<b>6</b>	<b>EVENT SELECTION</b>	<b>95</b>
6.1	Topological Analysis . . . . .	96
6.1.1	Muon + Jet Pre-selection . . . . .	96
6.1.2	Electron + Jet Pre-selection . . . . .	99
6.2	Topological Likelihood . . . . .	100
6.2.1	Variables . . . . .	101
6.2.2	Distributions . . . . .	102
6.2.3	Correlations . . . . .	102
6.2.4	Forming the Discriminant . . . . .	106
6.3	Analysis with b-jet identification . . . . .	110
6.3.1	Flavor Composition . . . . .	112



6.3.2	Tagging Probabilities . . . . .	116
6.4	Event Yield and Sample Composition . . . . .	117
<b>7</b>	<b>METHODS FOR THE TOP QUARK MASS MEASUREMENT</b>	<b>120</b>
7.1	Kinematic Fitting . . . . .	120
7.1.1	Fit Description . . . . .	121
7.1.2	Fit Performance . . . . .	123
7.2	Likelihood Fitting . . . . .	130
7.2.1	Fit Description . . . . .	130
7.2.2	Ensemble Tests . . . . .	135
<b>8</b>	<b>RESULTS WITH COLLIDER DATA</b>	<b>145</b>
8.1	Results with the Topological Selection . . . . .	145
8.2	Results with the Tagged Selection . . . . .	148
8.3	Systematic Uncertainty . . . . .	151
8.3.1	Jet Energy Scale Uncertainty . . . . .	151
8.3.2	Gluon Radiation . . . . .	157
8.3.3	Event Model . . . . .	159
8.3.4	Trigger Bias . . . . .	160
8.3.5	Limited Monte Carlo Statistics . . . . .	162
8.3.6	Calibration . . . . .	163
8.3.7	Jet Resolution . . . . .	163
8.3.8	b Tagging . . . . .	163
8.4	Systematic Uncertainty Summary . . . . .	165
8.5	Cross Checks . . . . .	165
8.6	Events . . . . .	167

<b>9</b>	<b>SUMMARY AND OUTLOOK</b>	<b>174</b>
9.1	Summary . . . . .	174
9.2	Outlook . . . . .	175
9.2.1	Short Term . . . . .	175
9.2.2	Intermediate Term . . . . .	177
9.2.3	Long Term . . . . .	178
<b>6</b>	<b>Bibliography</b>	<b>179</b>

# List of Figures

2.1	Top quark one loop contribution to the W and Z boson masses. . . .	11
2.2	Higgs boson loop contribution to the W and Z boson masses. . . . .	11
2.3	Lines of constant Higgs mass on a plot of $m_W$ versus $m_t$ . . . . .	12
2.4	$\chi^2$ fit for the the prediction of the mass of the Higgs boson from pre- cision electroweak data. . . . .	14
2.5	Top quark production via the strong interaction at hadron colliders. .	18
2.6	Parton Distribution Functions at the scale $m_t$ , relevant for top pro- duction. . . . .	21
2.7	Final state branching ratios for top quark pairs. . . . .	21
2.8	The lepton + jets final state. . . . .	23
2.9	W boson + multiple jets background. . . . .	24
2.10	World average of the top quark mass measurements. . . . .	25
2.11	Measured top pair production at two center-of-mass energies compared to theoretical predictions. . . . .	26
3.1	Overview of the Fermilab accelerator complex. . . . .	28
3.2	Cross-Section of the DØ Detector. . . . .	30
3.3	Difference in definition of detector and physics $\eta$ . . . . .	34
3.4	Cross-Section of the Central Tracking Region of DØ . . . . .	36
3.5	3D representation of the Silicon Micro-strip Tracker. . . . .	36

3.6	Schematic of a silicon strip detector and its operation principle. . . .	38
3.7	Cross Section of a SMT barrel . . . . .	38
3.8	Cross Section of the CFT. . . . .	40
3.9	The forward and central pre-shower detectors. . . . .	42
3.10	Cross Section of a Quarter of the Calorimeter . . . . .	44
3.11	Schematic view of a Calorimeter Cell. . . . .	44
3.12	$-\langle \frac{dE}{dX} \rangle$ as a function of muon momentum on Copper. . . . .	47
3.13	Overview of the muon system at DØ. . . . .	49
3.14	Muon Drift Tube Cross-Section. . . . .	50
3.15	Level 1 and L2 Trigger Architecture: The horizontal arrows denote information flow. . . . .	52
3.16	Conceptual Design of the Silicon Track Trigger. . . . .	56
3.17	Schematic view of a STT Crate. The overlaid cross-section of the silicon micro-strip detector shows the sectors which are processed by the crate. . . . .	58
3.18	Overview of the Level 3 Trigger and Data Acquisition System. . . .	62
4.1	Inputs to the electron likelihood [65]. . . . .	77
4.2	Electron Likelihood efficiency as a function of mis-identification rate [65]. . . . .	79
4.3	Jet energy Corrections. . . . .	85
6.1	$\mathcal{A}$ distributions (top left), $H'_{T2}$ distributions (top right), $K'_{Tmin}$ distri- butions (bottom left) and $\cancel{E}_T$ distributions (bottom right) for $t\bar{t}$ and background. . . . .	103
6.2	$\mathcal{A}$ versus $m_t$ (top left), $H'_{T2}$ versus $m_t$ (top right), $K'_{Tmin}$ versus $m_t$ (bottom left) and $\cancel{E}_T$ versus $m_t$ (bottom right) for $t\bar{t}$ . . . . .	105

6.3	$\mathcal{A}$ versus $H'_{T2}$ (top left), $\mathcal{A}$ versus $K'_{Tmin}$ (top right), $\mathcal{A}$ versus $\cancel{E}_T$ (middle left), $H'_{T2}$ versus $\cancel{E}_T$ (middle right), $K'_{Tmin}$ versus $H'_{T2}$ (lower left), and $K'_{Tmin}$ versus $\cancel{E}_T$ (lower right) for $t\bar{t}$ . . . . .	107
6.4	$\mathcal{A}$ fit (top left), $H'_{T2}$ fit (top right), $K'_{Tmin}$ fit (bottom left) and $\cancel{E}_T$ fit (bottom right) . . . . .	108
6.5	Discriminant for $t\bar{t}$ and background. . . . .	111
6.6	Lowest order diagrams for the flavor creation process. . . . .	113
6.7	One of the lowest order diagrams for b excitation. . . . .	114
6.8	An example of gluon splitting in the fragmentation process. . . . .	115
6.9	Sources of W+heavy flavor jets at the Tevatron. . . . .	116
7.1	W boson invariant mass without parton level corrections (top left), W boson invariant mass with parton level corrections (top right), Z invariant mass with and without parton level corrections (bottom) . .	125
7.2	$\chi^2$ rank of the correct permutation (left), $\chi^2$ for the correct permutation (right), and the distribution for of the lowest $\chi^2$ solution (bottom). .	126
7.3	$\chi^2$ rank of the correct permutation consistent with the tag (s) (left) and the distribution for the lowest $\chi^2$ permutation consistent with the tag (s). . . . .	127
7.4	Fit mass of parton matched events in the correct permutation (left) and the invariant mass of the three jets from the hadronically decaying top quark (right). . . . .	128
7.5	Fit mass of all events that pass the event selection in the lowest $\chi^2$ (red/dashed) compared to the fit mass for parton matched events in the correct permutation. . . . .	129

7.6	Comparison of the fit mass resolution in the lowest $\chi^2$ permutation consistent with the b-jet identification of two jets to that without any requirement on the b-jet identification. . . . .	130
7.7	Templates for the Topological Analysis (in order from top right to left bottom 150, 160, 165, 170, 175, 180, 185, 190, 200 GeV, the W+jets template is the extreme bottom). . . . .	133
7.8	Templates for the Tagged Analysis (in order from top right to left bottom 150, 160, 165, 170, 175, 180, 185, 190, 200 GeV, the W+jets template is the extreme bottom). . . . .	134
7.9	Comparison between the W+jets and multijet fit mass distribution. .	135
7.10	The most likely statistical uncertainty as a function of the requirement on the discriminant. . . . .	139
7.11	The extracted top quark mass for 200 ensemble tests using the topological event selection. . . . .	139
7.12	Calibration curve obtained from ensemble tests using the topological event selection. . . . .	140
7.13	Pull distribution of the 170 GeV ensembles fit with a Gaussian. . . .	141
7.14	Expected statistical uncertainty in the topological analysis from the 170 GeV ensembles. . . . .	141
7.15	The extracted top quark mass for 200 ensemble tests using the tagged event selection . . . . .	142
7.16	Calibration curve obtained from ensemble tests using the tagged event selection. . . . .	143
7.17	Pull distribution of the 170 GeV ensembles fit with a Gaussian with unit width. . . . .	144

7.18	Expected statistical uncertainty in the tagged analysis from the 170 GeV ensembles. . . . .	144
8.1	The likelihood curve from the fit of the topologically selected events (left). The distribution of fit masses of the topologically selected events (right). The red curve is the expectation from background only events (normalized to the fraction preferred by the fit) while the blue curve is the sum of the expectation from signal and background for the mass point closest to the fit result. . . . .	146
8.2	The distribution of the topological discriminant of the preselected events (without requirement on the topological discriminant). The red curve shows the expected distribution from background only and the blue curve is the expected distribution from signal and background (normalized to the number of data events with the signal to background returned from the likelihood fit). . . . .	147
8.3	The distribution of statistical uncertainties from ensemble tests of the $t\bar{t}$ sample with input mass of 170 GeV. The result in data is marked by the large arrow. . . . .	147
8.4	The likelihood curve from the fit of the tagged event selection (left). The distribution of fit masses of the events (right). The red curve is the expectation from background only events (normalized to the fraction preferred by the fit) while the blue curve is the sum of the expectation from signal and background for the mass point closest to the fit result. . . . .	149

8.5	The distribution of the topological discriminant of the tagged events. The red curve shows the expected distribution from background only and the blue curve is the expected distribution from signal and back- ground (normalized to the number of data events with the signal to background returned from the likelihood fit). . . . .	150
8.6	The distribution of statistical uncertainties from ensemble tests from a $t\bar{t}$ sample with input mass of 170 GeV. The result in data on the tagged sample is marked by the large arrow. . . . .	150
8.7	Fit mass versus discriminant value for the topological selection (left) and the tagged selection (right). . . . .	151
8.8	The jet energy scale deviation $\Delta S$ as a function of jet $\eta$ (det) for Monte Carlo (left) and for data (right) after basic JES correction (top), after JES+parton-level corrections, after eta-dependent adjustments (bottom). . . . .	154
8.9	$\Delta S_{data} - \Delta S_{MonteCarlo}$ as a function of $\gamma p_T$ . Displayed band shows relative JES error used to estimate JES uncertainty. . . . .	155
8.10	Variation of the fit mass distribution with the $\pm 1\sigma$ contours for signal (left) and background (right). . . . .	156
8.11	Jet $p_T$ spectrum for jets from the primary partons (blue) and gluons (red). . . . .	158
8.12	Fit mass distribution for events with (red) and without (blue) gluon radiation. . . . .	159
8.13	Fit mass distribution for W+light jet events (red) and W+heavy flavor (blue). . . . .	165



# List of Tables

2.1	List of the fundamental fermions and their properties. . . . .	5
2.2	The Standard Model gauge bosons and their basic properties. . . . .	6
3.1	Tevatron Run II Parameters. . . . .	34
3.2	Silicon Micro-strip Detector Overview. . . . .	37
3.3	CFT geometry parameters. . . . .	39
3.4	Parameters of the Calorimeter. . . . .	43
3.5	Resolution Terms for the Calorimeter. . . . .	46
3.6	Parameters of the Muon Drift Tubes. . . . .	56
4.1	Electron Requirement Efficiencies . . . . .	78
4.2	Jet Energy Resolution. . . . .	87
4.3	Requirements on the Construction and Selection of Secondary Vertices. . . . .	90
5.1	Overview of the $t\bar{t}$ lepton + jets samples used in the analysis. . . . .	93
5.2	Main Generation Parameters for $t\bar{t}$ and W+jets simulation. . . . .	94
5.3	Overview of the $t\bar{t}$ samples used in the analysis. . . . .	94
6.1	Muon Event Selection Efficiency per Requirement [82]. . . . .	98
6.2	Electron Event Selection Efficiency per requirement [82]. . . . .	100

6.3	Efficiencies for requirements after event preselection. The efficiencies quoted are relative to all previous requirements. . . . .	111
6.4	Flavor composition in the W + Jet sample [86], [22]. . . . .	114
6.5	Probability for signal and background events to be tagged corrected in data [86]. . . . .	117
6.6	Topological Event Yield. . . . .	118
6.7	Expected Sample Composition for Topological Analysis. . . . .	118
6.8	Tagged Event Yield. . . . .	119
6.9	Expected Sample Composition for Tagged Analysis. . . . .	119
7.1	Summary of the Topological Ensemble Tests . . . . .	143
7.2	Summary of the Tagged Ensemble Tests . . . . .	143
8.1	Fit results for variations of the topological discriminant requirement. . . . .	148
8.2	Likelihood Values for the Tagged Analysis. . . . .	149
8.3	Summary of the Systematic Uncertainty for the Topological Selection. . . . .	166
8.4	Summary of the Systematic Uncertainty for the Tagged Selection. . . . .	166
8.5	Fit results for variations of the topological discriminant requirement. . . . .	167
8.6	Summary of the Fit Results with the Topological and Tagged Fit Results. . . . .	167
8.7	Events in the Topological Selection. . . . .	168
8.8	Events in the Topological Selection- continued. . . . .	169
8.9	Events in the Topological Selection- continued. . . . .	170
8.10	Events in the Topological Selection- continued. . . . .	171
8.11	List of the Tagged Events. . . . .	172
8.12	List of the Tagged Events-continued. . . . .	173

# Chapter 1

## INTRODUCTION

*'The effort to understand the universe is one of the very few things that lifts human life a little above the level of farce, and gives it some of the grace of tragedy.'*

Stephen Weinberg

The Standard Model of particle physics is the theory which cohesively binds the amalgamation of all of the last century's data of elementary particles and their interactions. First developed in the 1960's by Glashow, Weinberg, and Salam [1], it has withstood close to four decades of experimental tests and describes nature remarkably at the precision level [2] where for the most precise measurements data and the standard model agree to better than 0.1 %. However, most high-energy physicists are not completely satisfied with the Standard Model. Despite its remarkable success, it has a large set of input parameters that cannot be derived by the model which seem to have a somewhat bewildering range of values. To test our understanding of elementary particles and their interactions we must probe nature with increasing scrutiny, building progressively larger and more complicated experiments. As well, the tools to analyze the data from these experiments have become increasingly complex. Both result in large collaborations of people to design, build, and execute the experiments.

This dissertation describes an analysis carried out the highest energy accelerator ever built, where colliding beams of protons and anti-protons counter rotate in a four-mile ring at the Fermi Lab National Accelerator outside of Chicago, IL. The design of the accelerator allows for collisions to occur at two points around the ring. At one of these points sits the DØ detector acting as a massive electronic eye allowing the collisions to be observed and analyzed to probe nature at the smallest distance scales currently accessible. Because of the large center-of-mass energy, one can also produce exotic particles with extraordinary properties. The goal of this dissertation is to measure the mass, as accurately as possible, of the heaviest elementary particle ever discovered: the top quark.

The dissertation begins in Chapter 2 which serves a dual purpose: an introduction to both the Standard Model of particle physics and the phenomenological role that the top quark plays in that model. As well, the chapter briefly reviews the previous work done on the subject and specifies how a more precise top quark mass measurement can increase our understanding in particle physics. Chapter 3 introduces the tools which are needed to perform the measurement. Briefly reviewing the accelerator which allows the production of the top quark, Chapter 3 focuses mainly on the DØ detector which is used to analyze the particles produced in the collisions. After describing the detector, Chapter 4 describes how one reconstructs the particles and objects from digital information from the detector to extract the detailed properties of the event. Chapter 5 describes the simulation process and lists all the simulated events that were used in this analysis. In Chapter 6, the way in which the events that are most likely contain top quarks are selected is described. Chapter 7 deals with the tools for analyzing these events and extracting information about the top quark mass. The results of the experiment and the analysis are presented in Chapter 8. Finally, Chapter 9 contains a summary of the results found here and an outlook for future

prospects.

Throughout the dissertation, natural units are used. This system of units is defined by setting  $\hbar = c = 1$ . In this system of units, one can take a single unit to express mass, energy, and momentum. In high energy physics the most convenient unit is the GeV which is used throughout the dissertation.

## Chapter 2

# PHENOMENOLOGY AND MOTIVATION

*'God could cause us considerable embarrassment by revealing all the secrets of nature to us: we should not know what to do for sheer apathy and boredom'*

Johann Wolfgang von Goethe

This chapter reviews the role of the top quark in the context of the Standard Model and other models of particle physics and presents the motivation for the measurement. As well, this chapter reviews previous experimental measurements of the top quark mass.

### 2.1 A Brief Review of the Standard Model

The Standard Model of particle physics is a description of nature at distance scales of  $\approx 10^{-15} \text{ m}$ <sup>a</sup>. Developed in the 1960's and 70's, the model has been verified to a high degree of precision at many experiments since that time and provides a very

---

<sup>a</sup>What follows is a relatively simple and brief description of the Standard Model for a more complete review see, for example [3], [4], or [5].

good description of all currently observed phenomena. The Standard Model is a quantum field theory which describes the most basic constituents of matter and their interactions. The particles of the Standard Model can be divided into two classes: the spin  $\frac{1}{2}$  fermions which compose matter and the integer spin bosons which provide the interaction between the fermions. Table 2.1 lists the fundamental fermions and a few of their most important properties [6].

Name	Symbol	Charge	Mass (MeV)	Interactions
electron	e	-1	0.511	electromagnetic, weak, gravity
electron neutrino	$\nu_e$	0	$< 0.000003$	weak, gravity
up quark	u	$\frac{2}{3}$	$\approx 3$	electromagnetic, weak, strong, gravity
down quark	d	$-\frac{1}{3}$	$\approx 5$	electromagnetic, weak, strong, gravity
muon	$\mu$	-1	105.7	electromagnetic, weak, gravity
muon neutrino	$\mu_\nu$	0	$< 0.19$	weak, gravity
charm quark	c	$\frac{2}{3}$	$\approx 1200$	electromagnetic, weak, strong, gravity
strange quark	s	$-\frac{1}{3}$	$\approx 100$	electromagnetic, weak, strong, gravity
tau	$\tau$	-1	1777	electromagnetic, weak, gravity
tau neutrino	$\nu_\tau$	0	$< 18.2$	weak, gravity
bottom quark	b	$-\frac{1}{3}$	$\approx 4500$	electromagnetic, weak, strong, gravity
top quark	t	$\frac{2}{3}$	$\approx 178,000$	electromagnetic, weak, strong, gravity

Table 2.1: List of the fundamental fermions and their properties.

There are several things to note about Table 2.1. First, the division of the table into three sub-tables is not arbitrary. These three divisions reflect the fact that, evidently, the fundamental fermions come in three families or three generations. Those in the first generation including the electron, up, and down quarks constitute all of the ordinary matter that we are familiar with. However, there exist two heavier copies of the first generation with similar properties and interactions and they are distinguished by their larger masses.

Each generation of leptons has one charged lepton and a neutral neutrino. Until quite recently, the standard model assumed that the neutrinos had zero masses and

hence did not feel the gravitational interactions. Recently experiments indicate that the masses of the neutrinos are non-zero [7]. However, the two interactions which neutrino do take part in are very weak (discussed below). So weak in fact that neutrinos cannot be directly detected in the experiment described in this thesis. However, since neutrinos do carry momentum and energy their presence can be inferred in particle interactions by looking for significant 'missing' energy or momentum.

Quarks are distinguished from leptons in two fundamental ways. First, the charge of the quarks is seen to be come in fractional amounts. Secondly, the quarks are the the only fermions which feel the strong interactions. These strong interactions bind the quarks into nucleons and other more exotic hadrons (see below).

The third class of elementary particles are the gauge bosons which are responsible for the interactions between the fermions. Table 2.1 gives an overview of the Standard Model bosons and their properties [6]. In quantum field theory, the interactions between the fermions take place via exchange of the force carrying bosons. Therefore, another way of describing the force between the fermions is to describe the coupling which takes place between the fermions and the gauge bosons.

Name	Symbol	Charge	Spin	Mass (GeV)
Photon	$\gamma$	0	1	0
Z	Z	0	1	91.2
$W^\pm$	$W^\pm$	$\pm 1$	1	80.4
Gluon	g	0	1	0
Higgs	H	unknown	0	$> 114.4$

Table 2.2: The Standard Model gauge bosons and their basic properties.

The photon is the carrier of the electromagnetic force and 'mediates' the interactions between electrically charged particles. Because the photon is massless, the interaction is long range and falls off like  $1/r^2$ . Besides gravity, which holds us to the



earth, all of the interactions that we have with our environment, all of chemistry and biology, are dictated by the quantum version of electromagnetism or 'QED' (quantum electrodynamics).

The weak interactions are mediated by the heavy W and Z particles and have an effective interaction which operates at only relatively small distances. This is the force that is responsible for radioactive decay. One of the most attractive features of the Standard Model is that it treats the electromagnetic and weak forces in a unified manner. This leads to the two forces being referred to as the 'electroweak' force.

The strong force (quantum chromodynamics or 'QCD') is mediated by the gluons. The photon couples to particles that have electric charge. In an analogous manner, the gluons couple to objects which possess a 'color' charge. Unlike electromagnetism which has only two types of charge (positive and negative), the strong interaction has three color charges referred to as 'red', 'green', and 'blue'. For anti-quarks they are 'anti-red', 'anti-green', and 'anti-blue'. Like the weak interactions, the strong force is a short ranged interaction however this is not caused by having heavy gauge bosons but rather by another characteristic of the strong force. The gluons themselves are colored particles, and hence interact with each other. This leads to the following remarkable behavior. As the energy of the interaction between the quarks increases, the strength of the interaction decreases. For high energy interactions ( $E \approx 10 \text{ GeV}$ ) the quarks behave like free particles. At lower energies the interactions grow in strength. So strong, in fact, that individual quarks are not seen in nature. Except for brief moments in high energy collisions they are bound so strongly to other quarks that they form composite particles.

Even in high energy collisions, the quarks do not remain free for very long. Within a time scale typical of strong interactions ( $\approx 10^{-24} \text{ s}$ ), the interactions will have enough energy to produce a quark-anti-quark pair which will bind with the original

quark. In fact this process can continue such that a high energy quark will quickly produce a large number of quark-anti-quark pairs which will form composite particles. This process is referred to as fragmentation or hadronization. Hence, in high energy collisions of hadronic particles, although it is the quarks and gluons which are the fundamental participants in the interaction, only the composite hadrons are available to the experimenter. Because of conservation of momentum and energy, the hadrons which are produced form a collimated jet of hadronic particles which are created from the quark which initiated the process.

The Standard Model has one final gauge boson: the Higgs particle. The interactions of the Standard Model are introduced by demanding a gauge symmetry. In order to preserve this symmetry, it turns out that this requires the corresponding boson to have zero mass. This is the case for the photon and the gluons. However, the carriers of the weak interaction (the  $W^\pm$  and the  $Z$ ) have manifestly non-zero masses. The Higgs mechanism is the Standard Model's way of avoiding this problem. By introducing a new scalar field, it turns out that one can construct the interactions with the  $W^\pm$  and the  $Z$  such that they acquire mass. In a similar way, the fermions can acquire mass. This process explicitly breaks the symmetry of the interactions, and hence is called electroweak symmetry breaking. For a detailed description of this mechanism see [3], for example. However, despite decades of direct and indirect searches the associated Higgs particle predicted by the Standard Model has yet to be discovered.

The remaining of the four known forces is gravity. Currently, there is no quantum theory of gravity and hence it has not been discussed here in the context of particle interactions. If the theory of gravity is similar to the other forces (that is a quantum gauge theory), a graviton with zero mass and spin 2 is predicted. However, because gravity is some forty-one orders of magnitude weaker than the electromagnetic force

the graviton has yet to be observed (if it exists). On the other hand, because gravity is so much weaker it does not play an important role in the dynamics of the particles studied here <sup>b</sup>.

## 2.2 The Role of the Top Quark Mass in the Standard Model

The top quark plays an important role in the electroweak sector of the Standard Model through precision tests of electroweak theory. At lowest order (so called ‘tree-level’), all the electroweak quantities depend upon just three parameters [5]:  $g$ ,  $g'$ , and  $\nu$ .  $g$  and  $g'$  are the couplings of the electromagnetic and weak interactions and  $\nu$  is the vacuum-expectation value of the Higgs field. It is typical to use the three best-measured electroweak quantities to determine the values of these parameters [9] (in units where  $\hbar$  and  $c$  are equal to 1) :

$$\alpha = \frac{1}{4\pi} \frac{g^2 g'^2}{g^2 + g'^2} = \frac{1}{13.03599911(46)} \quad (2.1)$$

$$\frac{G_F}{(hc)^3} = \frac{1}{\sqrt{2}\nu^2} = 1.16637(1) \times 10^{-5} \text{ GeV}^{-2} \quad (2.2)$$

$$M_Z = \frac{1}{2} \sqrt{g^2 + g'^2} \nu = 91.1876(21) \text{ GeV} \quad (2.3)$$

where  $\alpha$  is the electromagnetic coupling at low energies,  $G_F$  is the Fermi constant,  $M_Z$  is the mass of the Z boson, and the numbers with parentheses are the uncertainties on these quantities. However, because of higher order quantum corrections (known as loop contributions or radiative corrections) the parameters of the other Standard

---

<sup>b</sup>Actually, there *are* recent theories which elevate the role of gravity in particle physics, see [8]. However, these are models beyond the scope of the material presented here.

Model particles also contribute to any process. The relative importance of these corrections depends on the functional form of the correction as well as value of the physical parameter. Because of the large mass of the top quark, there are many radiative corrections in which the top quark plays a pivotal role. Here, we only discuss what is generally considered the most important aspect of the top quark mass in electroweak physics: its role in the prediction of the mass of the hypothetical Higgs boson. For a more complete catalog of the role of the top quark in the Standard Model see [10] and [11].

The Standard Model predicts that at tree level the mass of the W boson and the Z boson are related via:

$$\frac{m_W}{m_Z} = \frac{g'}{\sqrt{g'^2 + g^2}} \equiv \cos \theta_W \quad (2.4)$$

where  $\theta_W$  is the weak mixing angle. It is convenient to re-write these equations and to express the mass of the W boson in terms of the other measured quantities. At tree-level this can be written as:

$$m_W^2 = \frac{\pi\alpha}{\sqrt{2}G_F \sin^2 \theta_W} \quad (2.5)$$

Higher level corrections lead to modifications of this expression which can then be written as [9] :

$$m_W^2 = \frac{\pi\alpha}{\sqrt{2}G_F \sin^2 \theta_W (1 - \Delta r)} \quad (2.6)$$

where  $\Delta r$  contains the higher order corrections. The contribution from the top quark can be written to first order as: [9]

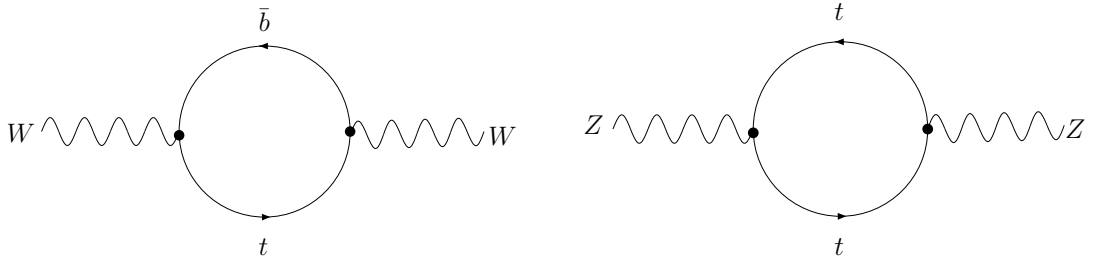


Figure 2.1: Top quark one loop contribution to the W and Z boson masses.

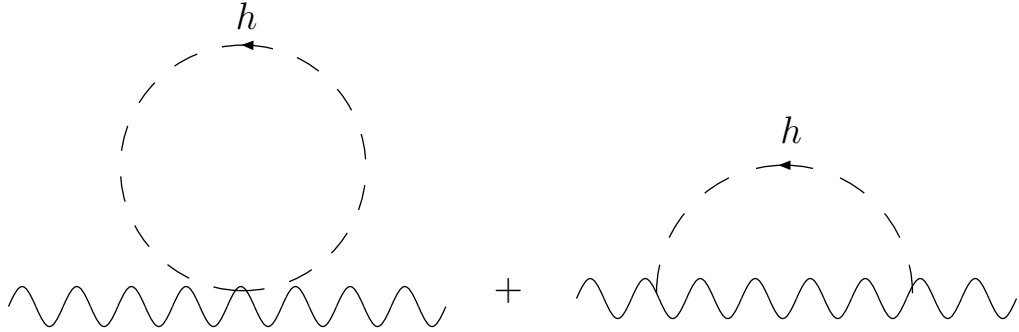


Figure 2.2: Higgs boson loop contribution to the W and Z boson masses.

$$(\Delta r)_{top} \approx -\frac{3G_F m_t^2}{8\sqrt{2}\pi^2} \frac{1}{\tan^2 \theta_W} \quad (2.7)$$

which are depicted as Feynman diagrams in Fig. 2.1.

The Higgs boson also contributes to  $\Delta r$  via radiative corrections and to the first order the correction can be written:

$$(\Delta r)_{Higgs} \approx \frac{11G_F m_Z^2 \cos^2 \theta_W}{24\sqrt{2}\pi^2} \ln \frac{m_h^2}{m_Z^2} \quad (2.8)$$

which at one loop has the contributions shown in Fig. 2.2.

The most striking difference between the two contributions is that while the W boson mass has a contribution from the top quark mass which scales as the top

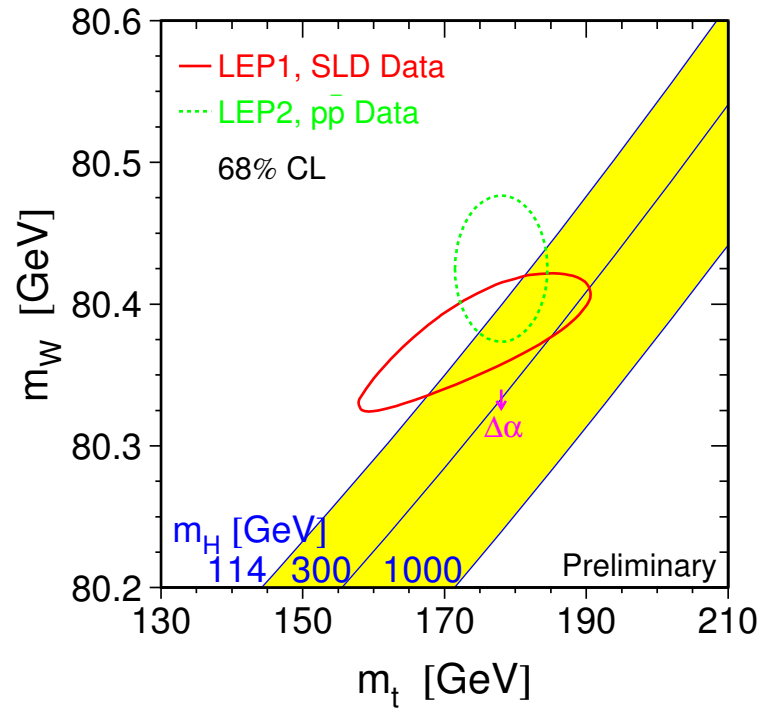


Figure 2.3: Lines of constant Higgs mass on a plot of  $m_W$  versus  $m_t$ .

quark's mass squared, the contribution from the W boson mass is only logarithmically dependent on the Higgs boson mass. Due to the corrections from  $\Delta r$  due to the Higgs boson and the top quark, in order to predict  $M_W$  the values of the Higgs boson mass and the top quark mass must be known as well. As mentioned in the previous section, the Higgs boson has yet to be observed. However, one can turn the argument around and find an expression for the prediction of the Higgs boson mass from the equations above. A graphical representation of this relationship is shown in Fig. 2.3 provided by Ref. [2]. The diagonal bands are lines of constant Higgs mass ranging from the current lower bound on  $m_h$  to the currently predicted upper bounds [6], around 1 TeV. The dashed ellipse is a 68% confidence level from direct measurements of  $m_W$  and  $m_t$ . The solid ellipse is a 68% confidence level from indirect constraints on precision electroweak data [2]. Hence, precision measurements of  $m_W$  and  $m_t$  can be used to make a prediction for  $m_h$ . One can already see that direct measurements prefer a light Higgs boson as indicated in a  $\chi^2$  fit from all electroweak data shown in Fig. 2.4 also from Ref. [2]. Note, however, that because of the one-loop diagrams in Fig. 2.2 the dependence of  $\Delta r$  depends only logarithmically on the mass of the Higgs boson. The different curves represent different values of  $\alpha$ , the electromagnetic coupling constant. Although this is one of the better known electroweak observables the contribution from strong interactions at low energies currently has a noticeable affect on the prediction.

Although the contribution to  $\Delta r$  from the top quark is rather strong (quadratically dependent), the contribution from the Higgs boson mass is rather weak (logarithmic). Thus, in order to significantly constrain the Standard Model prediction of the Higgs boson mass the uncertainty on both the top quark mass and the W boson mass must be rather small. With precision measurements, the top quark mass can be used to test the predictions of the Standard Model.

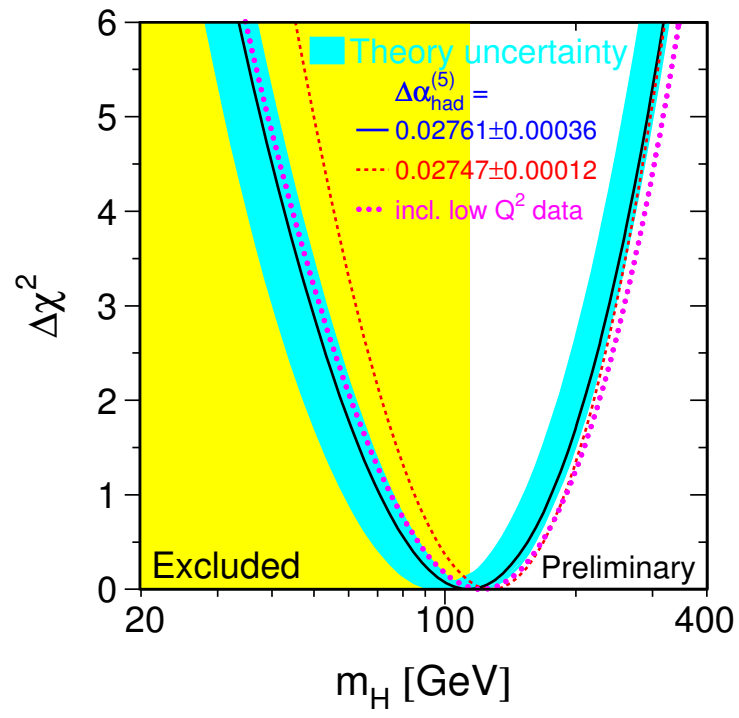


Figure 2.4:  $\chi^2$  fit for the prediction of the mass of the Higgs boson from precision electroweak data.



## 2.3 The Role of the Top Quark Mass Beyond the Standard Model

There is little doubt that the Standard Model is a correct theory for energies up to  $\approx 1$  TeV. However, it has always been known that it can not be a complete theory. For example, at some energy scale gravitational interactions will become important and these are not presently considered in the Standard Model. There is general consensus, therefore, that the model is incomplete.

In particular, the Standard Model has a large number of input parameters which cannot be predicted: masses of fermions, strength of the interactions, seemingly arbitrary number of generations, etc. From an experimental point of view, perhaps the most compelling argument against the Standard Model as the 'ultimate' theory is the large amount of 'fine-tuning' of the parameters. The most famous and striking example comes from radiative corrections to the Higgs mass. Just as there are radiative corrections to the W and Z masses as discussed in the previous section, if the Higgs boson exists there are radiative corrections to its mass as well. The physical Higgs boson mass can be written as [5]:

$$m_h^2 = m_{h0}^2 + \frac{\lambda}{4\pi^2} \Lambda^2 + \text{counterterm} \quad (2.9)$$

where  $m_{h0}$  is the Higgs mass at tree level or the 'bare' mass,  $\lambda$  is a coupling constant and  $\Lambda$  is the cut-off scale of the Standard Model. The problem arises because of two facts:

- Unitary constraints require the Higgs boson mass to be less than  $\approx 1$  TeV[6].
- The correction factor  $\Lambda$  has a quadratic contribution to the physical Higgs mass.

If the cut-off scale is as high as the Planck Scale,  $\approx 10^{19}$  GeV (where gravity

becomes important), then one needs a cancellation of parameters of extraordinary precision in order to retain a light Higgs boson (the quadratic divergence to the cut-off scale requires the introduction of the counter-term). If the cut-off scale is significantly closer to the electroweak scale where the Higgs mass is favored both by theory and experiment, then a new theory replaces the Standard Model at energies that are almost accessible by today's experiments. Either way, the Standard Model will need a replacement. This is generally known as the 'hierarchy' problem.

Because of its large mass, the top quark may play an important role in testing other theories as well. A complete review of these theories is beyond the scope of this work. Instead, a brief summary of the role the top quark may play in two such theories is presented: supersymmetry, and models which predict new strong interactions for the top quark.

### 2.3.1 Supersymmetry

One way of avoiding the large radiative corrections which lead to the hierarchy problem is to introduce new particles which cancel the contributions from the known standard model particles. In order for this cancellation to occur, a special symmetry must exist between the known particles and their supersymmetric partners which relates fermions to boson. Along with this property, supersymmetric theories have many other features which many consider quite favorable [12]. However, as of this writing no supersymmetric particles have been discovered. Fairly stringent constraints have already been placed on many of the most important parameters of the theory. In particular, the minimal supersymmetric model (MSSM) seems to favor a light Higgs boson [13]. This can be seen from the expression for the lightest supersymmetric Higgs boson mass at one loop in the MSSM [14]:

$$m_h^2 < m_Z^2 \cos^2 2\beta + \frac{3G_F}{\sqrt{2}\pi} m_t^4 \ln \frac{\tilde{m}_t}{m_t} \quad (2.10)$$

where  $\tan \beta = \frac{\nu_1}{\nu_2}$  ( $\nu_1$  and  $\nu_2$  are the vacuum expectation values of the two physical Higgs bosons), and  $\tilde{m}_t$  is the mass of the top's supersymmetric partner, the stop. The strong dependence on the top quark mass can be seen from this equation. In fact general models of supersymmetry predict a light Higgs boson with  $m_h < 130$  GeV [12]. As well, since the value of  $m_t$  it appears that the stop mass may be relatively light and should be within experimental reach if they exist [13]. Hence, the large value of  $m_t$  has many important consequences for supersymmetric theories. If supersymmetry were to be discovered the self-consistency of different models could be tested with the precise knowledge of the top quark mass.

### 2.3.2 New Top Strong Interactions

There are also models of electroweak symmetry which do not invoke a Higgs particle. The most famous of these is a class of models called Technicolor [15] [16]. Rather than introducing an elementary scalar field which breaks the electroweak symmetry and gives mass to the W and Z bosons, this idea posits that new strong dynamics exist. The symmetry breaking scheme in Technicolor is caused by the dynamics of the new strong interaction. Technicolor also predicts that 'techni-mesons' which take the place of a fundamental scalar (like the Higgs boson), are the longitudinal components of the W and Z bosons giving them their masses. The original Technicolor concept needed modification to explain several experimental constraints, one of which is the large top quark mass [17] amongst others. In order to explain the large top quark mass, a class of models known as TopColor has been developed [18]. In Topcolor models, a still new strong interaction which preferentially couples to the third generation is

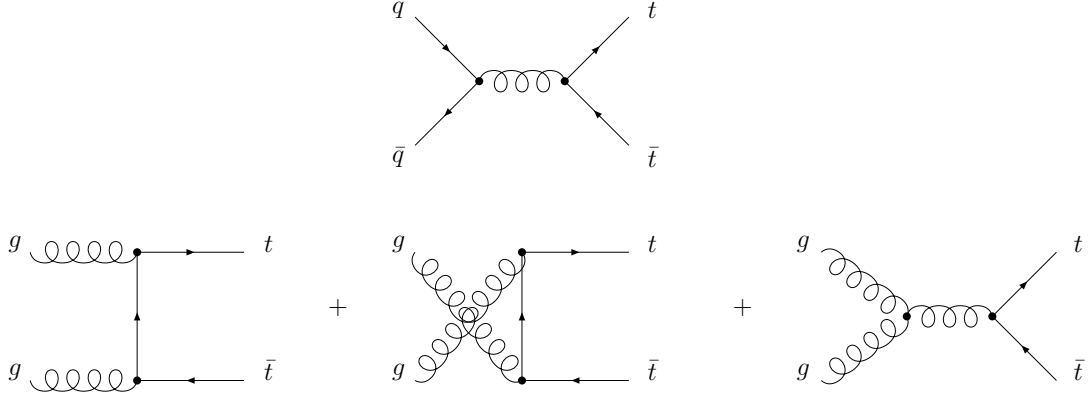


Figure 2.5: Top quark production via the strong interaction at hadron colliders.

posited. Experimentally, this would result in bound states of the top quark (which are absent in the standard model where the top decays before hadronization occurs). If this theory is correct, experiments should be able to reveal the existence of these top-mesons. The absence of such mesons could indicate that topcolor is incorrect and perhaps that the electroweak interactions are not broken by strong interactions.

## 2.4 Top Production at the Tevatron

Although protons and anti-protons are collided at the Tevatron, the energies are high enough that during a hard scattering event the particles get close enough together to 'see' the parton substructure: as a collection of quarks and gluons. The top quark is primarily produced in pairs by the strong interaction at hadron colliders. The lowest order diagrams for top quark production are shown in Fig. 2.5. There are two contributions shown: one from quark-anti-quark annihilation (the upper diagram) and gluon-gluon fusion (the lower set of diagrams). If the proton four-momentum is given by  $P_1$  and the anti-proton four momentum is  $P_2$  in the center of momentum frame we can write the momenta as (following [9]):

$$P_1 = (E, 0, 0, p) \quad (2.11)$$

$$P_2 = (E, 0, 0, -p) \quad (2.12)$$

adding the two four-vectors and squaring:

$$S \equiv (P_1 + P_2)^2 = (2E)^2 \quad (2.13)$$

on the other hand:

$$(P_1 + P_2)^2 = P_1^2 + P_2^2 + 2P_1 \cdot P_2 \approx 2P_1 \cdot P_2 \quad (2.14)$$

where the mass of the proton has been neglected ( $P_1^2 = P_2^2 = m_p^2$ ) in the approximation above. Comparing equation 2.13 with 2.14 we can trivially conclude:

$$S \approx 2P_1 \cdot P_2 \quad (2.15)$$

As mentioned earlier, it is the partons of the proton and anti-proton that we need to consider. If the parton from the quark has momentum fraction  $x_1$  and the parton of the anti-proton has momentum fraction  $x_2$  of the anti-proton we can define the square of the total energy in the partonic subprocess as:

$$\hat{s} = (x_1 P_1 + x_2 P_2)^2 \approx 2x_1 x_2 P_1 \cdot P_2 = x_1 x_2 S \quad (2.16)$$

Since there has to be at least enough energy to produce a  $t\bar{t}$  pair at rest we must

have  $\hat{s} \geq 4m_t^2$ . Therefore, in order to produce a  $t\bar{t}$  pair we must have [9]:

$$x_1 x_2 \geq \frac{4m_t^2}{S} \quad (2.17)$$

Now, the probability of finding a parton with momentum-fraction  $x$  must fall off with increasing  $x$ . If we make the simplifying approximation that  $x_1 \approx x_2 = x$  we find:

$$x = \frac{2m_t}{\sqrt{S}} \quad (2.18)$$

The distribution of fraction of the momentum of the up quarks, down quarks, and gluons is shown in figure 2.6 from Ref. [19]. At a center-of-mass energy of the Tevatron (1.96 TeV) the typical momentum fraction of a parton is  $\approx 0.18$ . From figure 2.6 that the probability of finding a quark-anti-quark pair above the threshold for top pair production is significantly higher. Next to leading order calculations from Ref. [20] predict a pair production cross-section of  $6.70 \text{ pb} \pm 10\%$  with quark-anti-quark annihilation accounting for about 85% of the cross-section.

## 2.5 Top Quark Decay

Unlike the other quarks, the top quark is expected to decay before it has a chance to hadronize. In the Standard Model, the top quark is predicted to decay to a W boson and a bottom quark with a branching ratio which is  $\approx 1$  [21]. The bottom quark will hadronize, forming a hadronic jet of particles with 100% probability. However, the W boson can decay either leptonically into a charged lepton and the corresponding neutrino or it can decay hadronically. The quarks from the hadronically decaying W boson will also hadronize and form jets of hadronic particles.

To a good approximation, each decay is equally probable [6]. However, for the

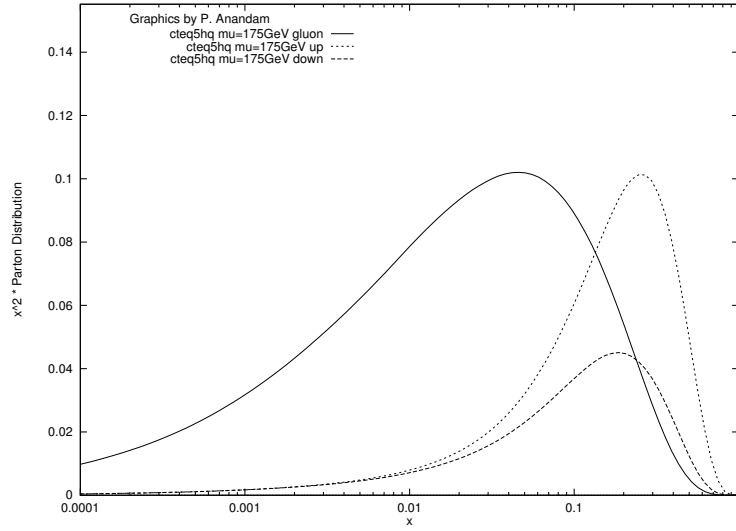


Figure 2.6: Parton Distribution Functions at the scale  $m_t$ , relevant for top production.

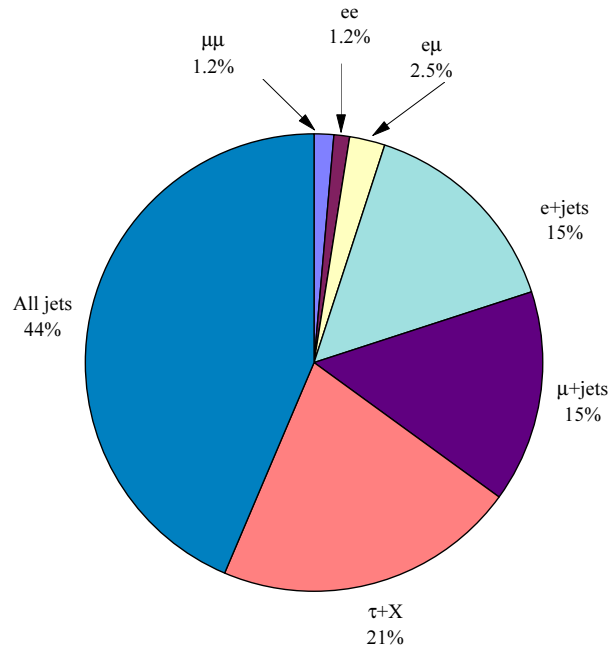


Figure 2.7: Final state branching ratios for top quark pairs.

hadronic decays there are three possible colors and hence the probability to decay into a quark of any color is enhanced by a factor of three. Hence, the probability for the W boson to decay into any of the three charged leptons and the corresponding neutrino is  $\approx \frac{1}{9}$  while the probability for the W to decay into two quarks is  $\approx \frac{2}{3}$ . Figure 2.7 shows the branching ratio of the top quark pair decay modes.

## 2.6 Lepton + Jets Mode

In the case where one W decays leptonically, and the other decays hadronically there will be one charged lepton and multiple jets. For this reason this mode is labeled the 'lepton + jets' mode<sup>c</sup>. Since the tau decays relatively quickly into either hadronic or leptonic final states, it is more difficult to identify it experimentally and hence this mode is typically not considered part of the lepton + jets decay. In the work presented here, the charged lepton refers to only the electron or muon. Figure 2.8 shows the production and decay of a top and anti-top quark into the lepton + jets final state.

In the lepton + jets decay mode, one can directly detect the presence of the high energy lepton and several high energy jets. However, the neutrino which is very weakly interacting will pass through the detector without interacting. We can still infer its presence though. To a very good approximation, the total momentum transverse to the beam line before the collision is zero. Therefore, after the collision the total transverse momentum must be zero as well. The presence of a neutrino can be inferred when the final state particles' momentum that is seen by the detector appears to significantly non-zero. Unfortunately, this technique cannot be used in the direction parallel to the beam since many low energy particles escape down the

---

<sup>c</sup>Though, strictly speaking there are actually two leptons in the final state - the charged lepton and the neutrino.



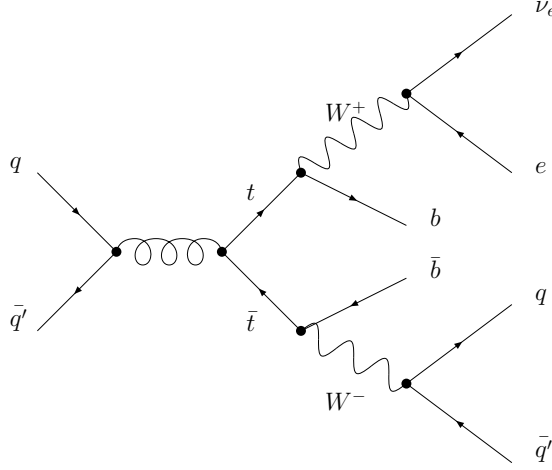


Figure 2.8: The lepton + jets final state.

beam pipe undetected. Therefore, the experimental signature of this mode is one high energy lepton, several high energy jets, and a significant 'missing' transverse momentum. Nominally, in this mode there are four jets. However, due to gluon radiation of either one of the initial or final state quarks there can be other jets in the event.

There are two major backgrounds to this channel. One is W boson production with multiple jets from either initial state gluon radiation or jets from 'spectator' quarks. The spectator quarks are partons from either the proton or anti-proton which do not take part directly in the hard scattering interaction but are broken apart from the disintegration of the proton or anti-proton. One expects a similar final state with a charged lepton and neutrino from the W boson decay along with multiple jets. This represents the dominant background. Figure 2.9 shows one of many diagrams that contributes to this process. The cross-section for this process is estimated by next-to-leading order calculations to be  $12.27 \pm 0.065$  [22] pb. The second background is from multi-jet events where a jet is misidentified as a charged lepton in conjunction

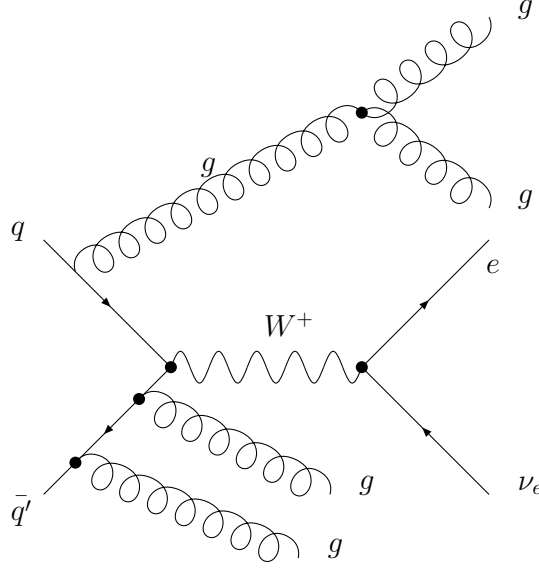


Figure 2.9: W boson + multiple jets background.

with significant mis-measurement of the momentum balance in the event. The details of these backgrounds and how they can be separated from the signal are discussed in Chapter five.

## 2.7 Previous Top Quark Measurements

The top quark was discovered in 1995 by the CDF and DØ collaborations [23] [24] with production cross sections of  $6.5 \pm_{1.4}^{1.7}$  pb and  $5.7 \pm 1.6$  pb, respectively. In the lepton + jets mode CDF [26] [27] measured a mass of  $176.1 \pm 5.1 \pm 5.3$  GeV while DØ measured  $173.3 \pm 5.2 \pm 4.9$  GeV, where the first error is statistical and the second is systematic. When both W bosons decay into a lepton and a neutrino the decay mode is called 'dilepton'. In this mode both CDF[28] and DØ [29] also measured the mass finding  $167.4 \pm 10.3 \pm 4.8$  GeV and  $168.4 \pm 12.3 \pm 3.6$  GeV, respectively. In the case where both W bosons decay hadronically, the mode is called

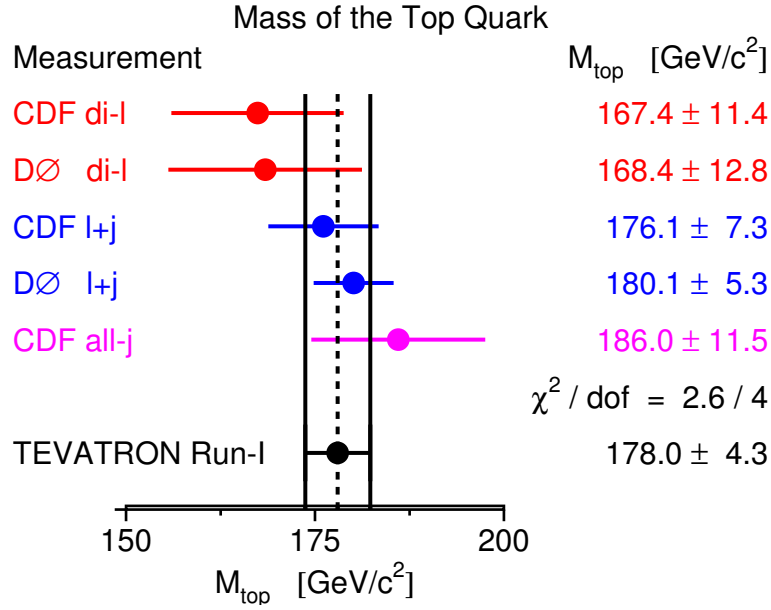


Figure 2.10: World average of the top quark mass measurements.

'all jets'. Again, both CDF[28] and DØ [30] measured the mass in this decay mode. In the all jets mode, CDF measured a mass of  $186.0 \pm 10.0 \pm 5.7$  GeV while DØ found a mass of  $176.1 \pm_{13.4}^{17.1}$  GeV. Finally, a recently published measurement of a new analysis of the same data led the DØ collaboration to measure a mass of  $180.1 \pm 3.6 \pm 4.0$  GeV in the lepton + jets channel. Figure 2.10 shows an overview of the previous mass measurements and the current world average [32] (note that the DØ all jets top mass result is still preliminary and has yet to be included in the world average). Finally, Fig. 2.11 shows the results of the cross-section analysis at both DØ and CDF compared to theoretical predictions at the two center-of-mass energies that the experiments have been run at.

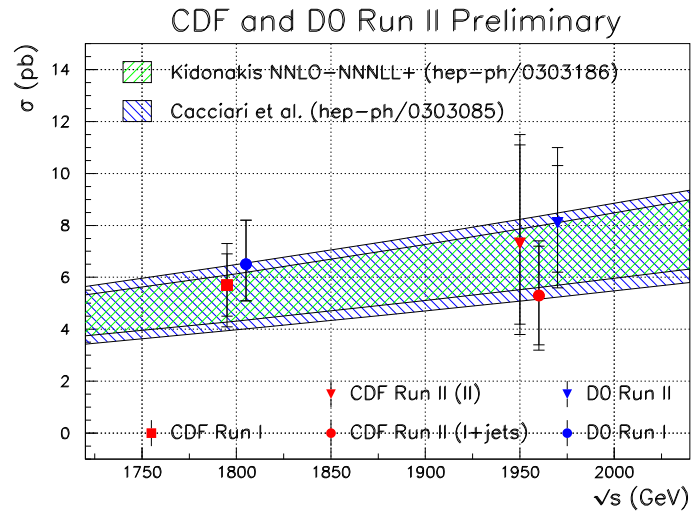


Figure 2.11: Measured top pair production at two center-of-mass energies compared to theoretical predictions.

## Chapter 3

# EXPERIMENTAL APPARATUS

*'Faith is a fine invention  
When Gentleman can see  
But Microscopes are prudent  
In an Emergency'*  
Emily Dickinson

In this chapter the experimental apparatus was used to perform the measurement is described including: the accelerator, the DØ Detector, and the triggering and data acquisition system (DAQ).

### 3.1 Accelerator

Currently, the only place in the world which can produce the top quark is Fermi National Accelerator Laboratory (Fermilab) which is located outside of Chicago, IL. The laboratory has facilities for various experimental programs ranging from Neutron therapy for cancer, fixed target experiments, and the highest center-of-mass (C.M.) collider physics program in the world. An overview of the accelerator focusing on its

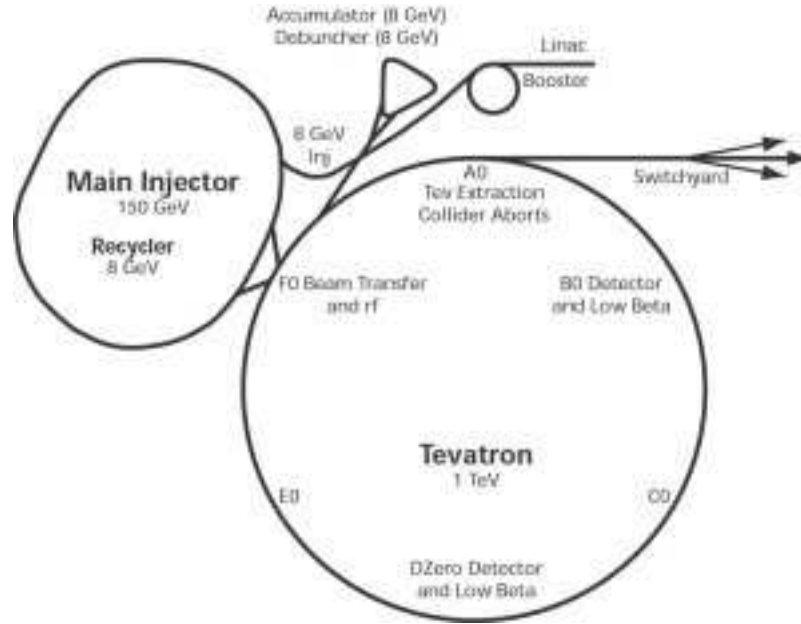


Figure 3.1: Overview of the Fermilab accelerator complex.

most important features and parameters is presented. What follows is an extremely simplified presentation of an very intricate instrument; for a more detailed description see Ref. [33].

The accelerator complex consists of a chain of accelerators which increases the energy of beam particles [34] ultimately accelerating protons and anti-protons to an energy of 0.98 TeV. The accelerator chain can be conceptually divided into four stages: particle production, pre-acceleration, acceleration to collision energies, and particle storage. An overview of the accelerator is shown in Fig. 3.1.

The proton source is a magnetron [35] which consists of a container which has a cathode on the inner wall and an anode on the outer wall immersed in a uniform magnetic field. Pressurized hydrogen gas is injected at one end. The cathode serves as the active surface for producing  $H^-$  ions which then form a dense plasma inside the magnetron. On the opposing end, an extractor plate accelerates the negative ions

out of the source while a magnetic field is used to steer electrons and other ions out of the  $H^-$  source. Both the hydrogen injection and the extraction voltage are pulsed at 15 Hz to match the frequency of the first bunched accelerator (the Linac).

Before the  $H^-$  ions reach the Linac they are pre-accelerated by a Cockcroft-Walton generator [36] to 750 KeV. The Linac [37] is approximately 80 meters long and consists of a series of five radio frequency (RF) tanks. Each tank consists of a series of alternating RF accelerating cavities and drift tubes. The Linac raises the beam energy to 400 MeV. The ions are lead from the Linac to the first of three synchrotrons: the Booster [38]. The Booster is a 8 GeV proton synchrotron that is 151 meters in diameter and contains 96 dipole/quadrupole magnets and 17 RF cavities. After being accelerated to 8 GeV the protons are extracted to the Main Injector [39]. The Main Injector is a second synchrotron with a circumference of approximately 3 km that serves two purposes. First it is used to raise the energy of the beam from 8 GeV to 150 GeV for injection into the final synchrotron: the Tevatron. Secondly, the Main Injector is used to accelerate protons to 120 GeV. These protons are extracted and collided into a nickel target. Of the many secondary particles that are created, a number of anti-protons are also created (approximately 1 for every 100 protons). The anti-protons are accumulated and stored for latter insertion into the Tevatron.

The final synchrotron, the Tevatron [40], accelerates protons and anti-protons inserted from the Main Injector up to 0.98 TeV <sup>a</sup>. With a radius of 1 km, 774 dipole magnets and 216 quadrupole magnets, the Tevatron is currently the world's largest and highest energy particle accelerator in operation. Protons are accelerated in one direction while anti-protons are accelerated in the opposite direction around the ring. The Tevatron currently operates in a '36 on 36' mode where 36 bunches of protons

---

<sup>a</sup>The original design specified an energy of 1 TeV. However, magnet stability dictated that the operation point of the Tevatron had to be lowered slightly.

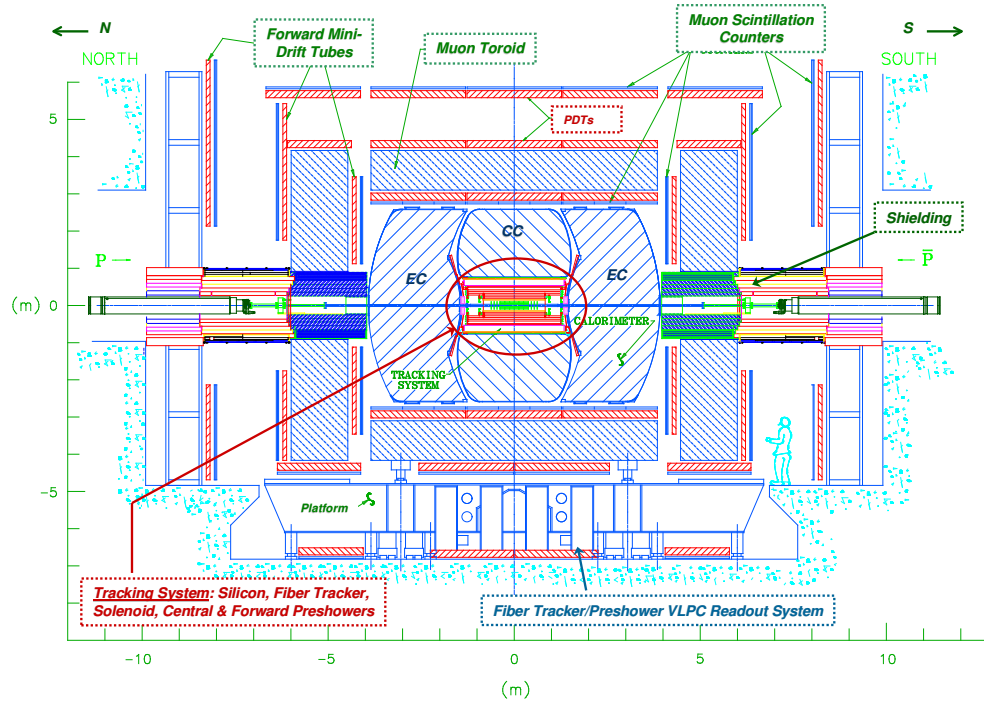


Figure 3.2: Cross-Section of the DØ Detector.

and 36 bunches of anti-protons counter circulate. In each proton bunch there are approximately  $10^{11}$  protons and in each anti-proton bunch approximately  $10^{10}$  protons. There are currently two luminous regions where the bunches are made to collide every 396 ns. One of these regions has the label DØ and that is where one of two large collider detectors at Fermi Lab is located.

## 3.2 Overview of the DØ Detector

The DØ Detector [41] is a large multipurpose collider detector constructed to study proton-anti-proton collisions at the Tevatron. An overview of the detector is shown in Fig. 3.2. The design of the detector closely reflects the prime physics goals of the experiment: the production of high mass states and the study of high  $p_T$  phe-



nomenon. These include, but are not limited to, the study of the W and Z bosons, searches for the Higgs Boson, new phenomena searches, and the study of the top quark. At a  $p\bar{p}$  collider these goals require excellent lepton identification, precision energy measurements, and the ability to identify the decay products of these particles such as bottom quarks.

The DØ detector is hermetic and covers nearly all  $4\pi$  surrounding the interaction region. In Fig. 3.2, the beam pipe pierces the DØ detector and the nominal collision point is at the center of the figure. Particles produced in the collision and their decay products are detected and their properties measured by a series of sub-detectors that are radially layered outward from the collision point. The detector has three main elements:

1. A central tracker immersed inside a 2 Tesla magnetic field.
2. A sampling calorimeter.
3. A muon detector.

The tracking detectors are positioned closest to the interaction point and have the finest segmentation. They are designed to measure the three dimensional trajectories of the charged particles passing through them. The presence of the magnetic field bends the trajectory of charged particles and allows a measurement of the particles' momenta. Surrounding the tracker is the calorimeter. This device measures the energy of the particles and is the backbone of the DØ detector. The tracking detectors are built out of light low Z material to introduce as little interactions as possible while still detecting their presence. In contrast, the calorimeter is constructed out of dense and thick material to absorb most of the particles which enter it. Indeed, only muons which have great penetrating power, and neutrinos which traverse the detector without interacting have a significant probability of penetrating the calorimeter. Precisely

because muons have such penetrating power, a separate detector system outside of the calorimeter is used to detect the presence and location of muons.

### 3.3 Coordinate System

The beam axis defines the z-axis and the direction of the protons is taken to point in the positive direction. The y-axis points vertically upward (from the ground) and forms a right handed coordinate system which points horizontally (level with ground). The  $\phi$  and  $\theta$  angles are the azimuthal and polar angles, respectively, with  $\theta = 0$  along the beam pipe. Because of the approximate axial symmetry of the detector, it is convenient to define the polar coordinates  $r$  and  $\phi$ .

$$r = \sqrt{x^2 + y^2} \quad (3.1)$$

$$\phi = \tan \frac{y}{x} \quad (3.2)$$

Since most of the particles of interest are ultra-relativistic it is convenient to use  $\eta$ , or the pseudo-rapidity, in place of  $\theta$ .  $\eta$  is related to the polar angle by:

$$\eta = -\ln \left[ \tan \left( \frac{\theta}{2} \right) \right] \quad (3.3)$$

It is simply the high-energy approximation of the true rapidity  $y$ :

$$y = \frac{1}{2} \ln \left( \frac{E + p_z}{E - p_z} \right) \quad (3.4)$$

where  $E$  is the energy of the particle, and  $p_z$  is the longitudinal momentum.

Rapidity is convenient for two reasons: rapidity intervals are Lorentz invariant

and particle multiplicity is approximately constant in rapidity. The former quality is important when discussing physics processes while latter is a guiding principle for the design of the detector.

Often it is convenient to use 'transverse' momentum rather than momentum. This is simply the portion of the momentum vector which is projected onto a plane transverse to the beam axis, defined by:

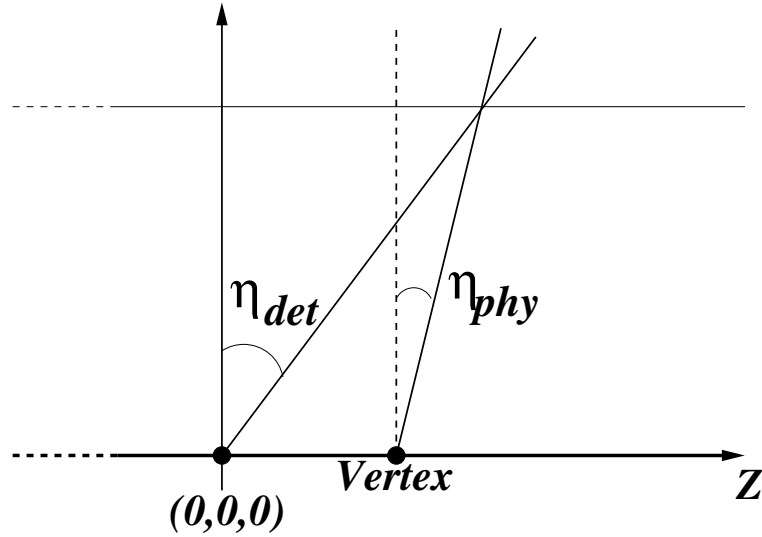
$$P_T = p \sin \theta \quad (3.5)$$

This is particularly useful in a  $p\bar{p}$  collider since the longitudinal momentum of the partons is not known. At the high energies achieved by the Tevatron, the hard scattering events take place between the partons which constitute the proton and anti-proton. The partons carry a fraction of the total momentum which is not known on an event by event basis. Further, many of the remnants of the collision escape down the uninstrumented beam pipe. However, the transverse momentum of the  $p\bar{p}$  system is essentially zero so one can apply conservation of momentum in the transverse plane.

Since the beam length in  $z$  is about 30cm, collisions do not always occur at the nominal center of the detector. Hence, when reconstructing the direction and transverse momentum of final state objects a correction for the  $z$  position is necessary, see Fig. 3.3. However, for discussing the position of the detector it is most convenient to speak of the 'detector'  $\eta$  or the  $\eta$  assuming a particle trajectory from the nominal center of the detector. Unless otherwise noted, when discussing detector elements the  $\eta$  referred to will be the detector  $\eta$ . Similarly, when referring to reconstructed physics objects such as electrons, jets, and muons the eta referred to is the 'physics'  $\eta$  which is simply the  $\eta$  of the object without reference to the detector.

Center of Mass Energy	1.96 TeV
Radius	1 km
Peak Luminosity	$\approx 70 \times 10^{30} \frac{1}{cm^2 s}$
Number of Bunches	36 p, 36 $\bar{p}$
Bunch Length	50 cm
Transverse Beam Radius	$\approx 40 \mu m$
$\bar{p}$ Stacking Rate	6-10 $\frac{mA}{h}$
RF Frequency	53 MHz
Period between Beam Crossings	396 ns

Table 3.1: Tevatron Run II Parameters.

Figure 3.3: Difference in definition of detector and physics  $\eta$ .

## 3.4 Central Tracking

The central tracker is composed of four elements: a Silicon Microstrip Tracker (SMT) [42], a Central Fiber Tracker (CFT) [43], a solenoid magnet [44], and pre-shower detectors [45].

As particles exit the beam pipe they progressively encounter the SMT and the CFT and finally penetrate the solenoid and exit the tracking region. A cross-section of the central tracker is shown in Fig. 3.4. Charged particles interact with the tracking detectors and leave a pattern of 'hits' in the various layers of the detectors. From these hits, a track can be reconstructed representing the trajectory of the charged particle. Since the entire tracking region is immersed in a highly uniform magnetic field, the charged particles' trajectories are bent. By measuring the curvature of the track, one can make a measurement of the particle's momentum. As well, tracks in the central tracker can be used to aid in identification of charged particles by matching the tracks with information from the other sub-detectors.

### 3.4.1 Silicon Micro-strip Tracker

A representation of the SMT is shown in Fig. 3.5 which straddles the beam pipe. The SMT detector is constructed in three modules : six barrels which instrument the central detector, twelve F disks interspersed along the barrels, and four H disks which cover the far forward region. Each barrel has four layers, two double sided layers and two single sided layers. The active part of the silicon sensor is a series of parallel strips. The barrel module detectors are 12 cm long with 50  $\mu\text{m}$  strip pitch. The double sided detectors have one side where the strips are parallel to the beam (axial) while the strips on the other side are placed at an angle (either at 2° or 90° with respect to the beam). A cross-section of the barrels is shown in Fig. 3.7.

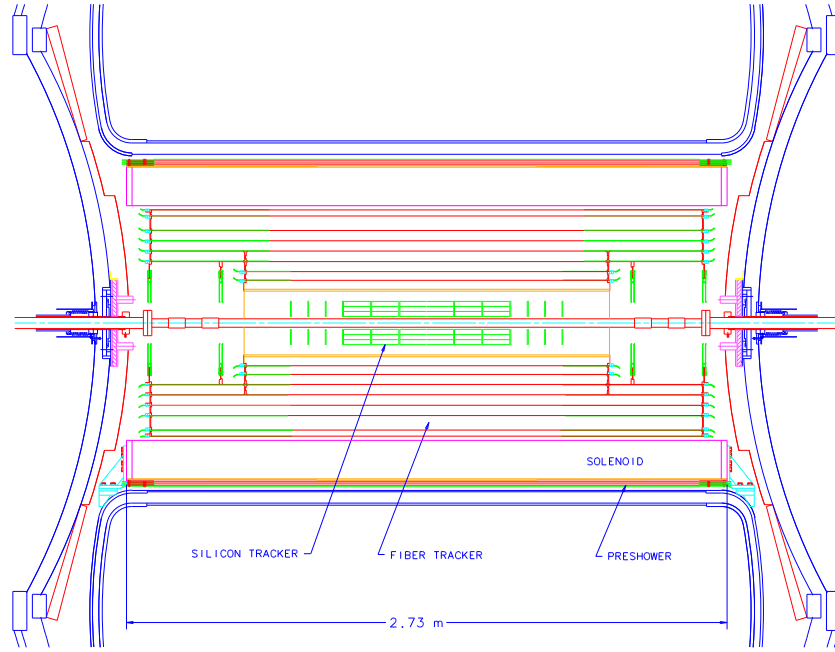


Figure 3.4: Cross-Section of the Central Tracking Region of DØ .

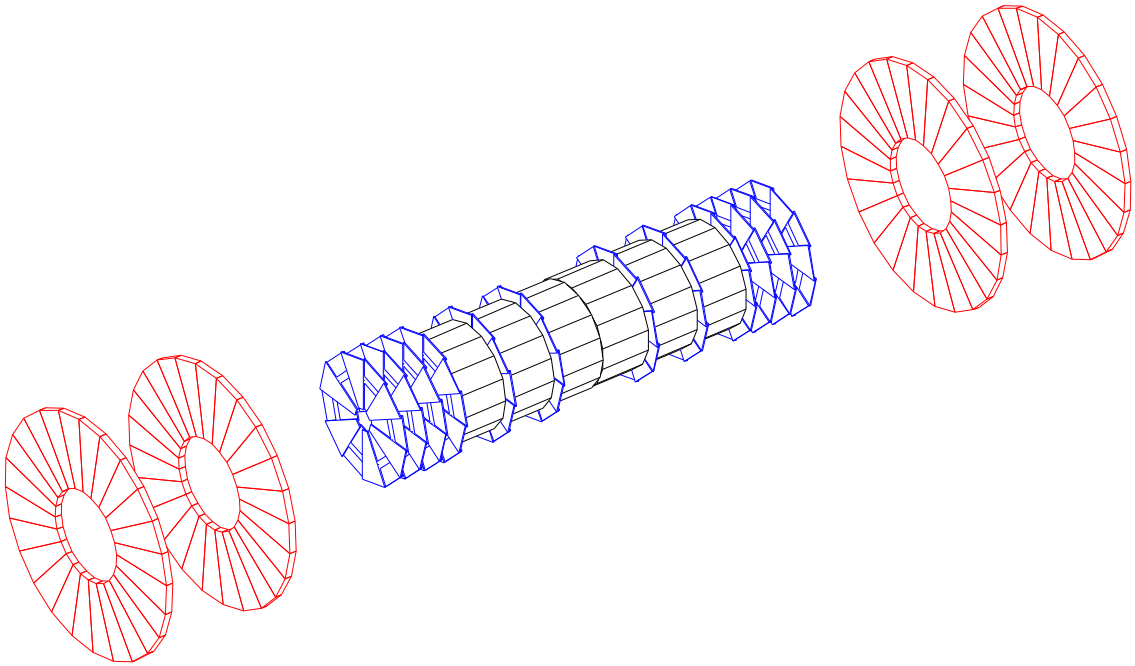


Figure 3.5: 3D representation of the Silicon Micro-strip Tracker.

The pitch of the strips was chosen so that the position resolution would be approximately 10 microns. The length of the barrel region is dictated by the fact that the interaction point has a wide distribution along the beam axis with  $\sigma_z = 28 \text{ cm}$ . The barrels extend  $\pm 38 \text{ cm}$  from the center of the detector. The SMT covers the eta range of  $|\eta| < 3$ .

	Barrels	F-Disks	H-Disks
Channels	387072	258048	147456
Modules	432	144	96
Silicon Area	$1.3 \text{ m}^2$	$0.4 \text{ m}^2$	$1.3 \text{ m}^2$
Inner Radius	$2.7 \text{ cm}$	$2.6 \text{ cm}$	$9.5 \text{ cm}$
Outer Radius	$9.4 \text{ cm}$	$10.5 \text{ cm}$	$26 \text{ cm}$

Table 3.2: Silicon Micro-strip Detector Overview.

The detectors are fabricated on n-type silicon wafers that are  $300 \mu\text{m}$  thick as shown in Fig. 3.6. The strips are formed by  $p^+$  implants along the length of the detector. A thin dielectric layer between the strips and an aluminum coating forms a capacitor which is AC coupled to the readout electronics. A radiation hard polysilicon resistor is used to bias the sensor. The sensors operate essentially as reverse biased diodes. When a charged particle passes through the sensor, electron/hole pairs are created. The electrons are then accelerated toward the positive voltage. The  $p^+$  silicon is separated from the aluminum readout strip by a silicon oxide layer which forms a capacitor. As electrons rush towards the  $p^+$  region, an image charge is formed on the aluminum which is collected and stored in an analog pipeline in a readout chip in an array of switched capacitors. The signal is buffered, digitized, and read out by a chip which is bonded onto the sensor.

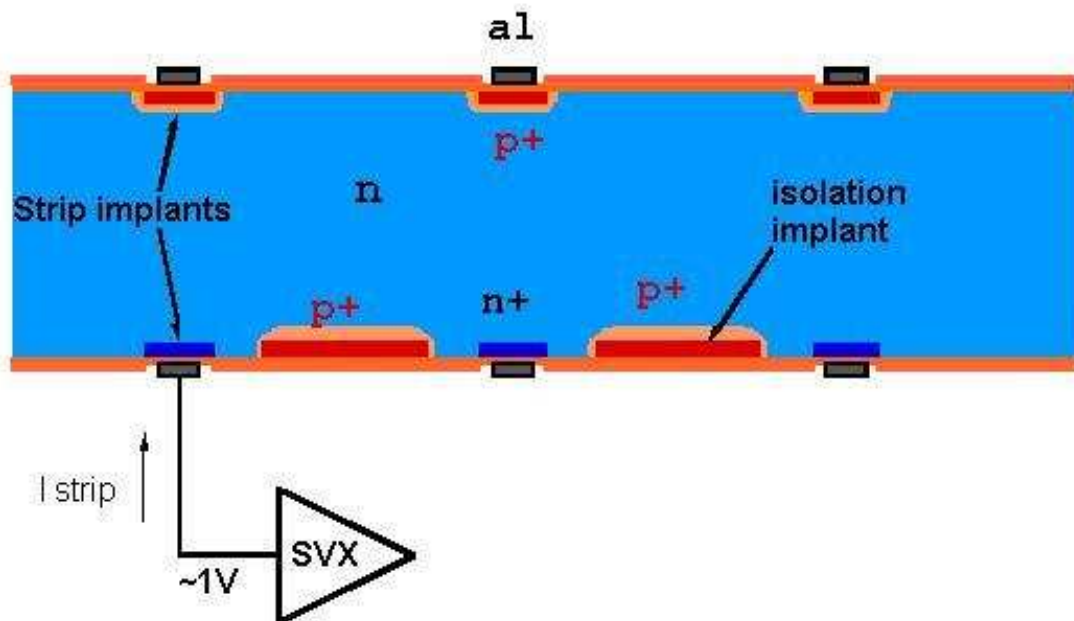


Figure 3.6: Schematic of a silicon strip detector and its operation principle.

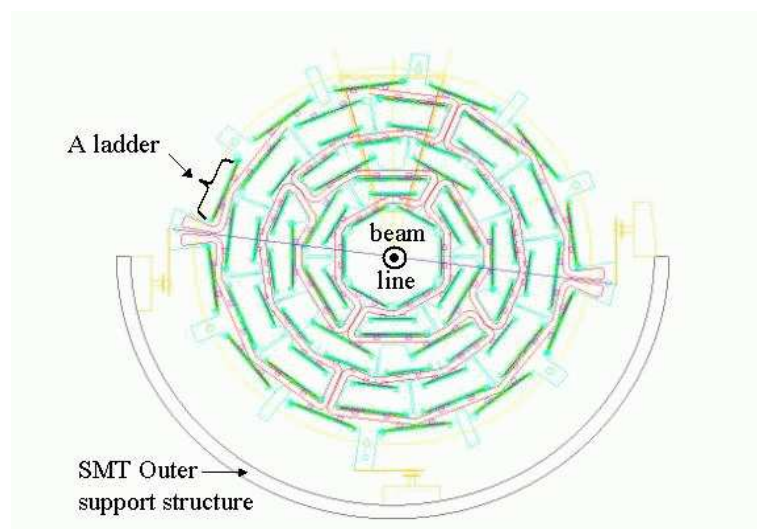


Figure 3.7: Cross Section of a SMT barrel



### 3.4.2 Central Fiber Tracker

The CFT consists of scintillating fibers mounted on eight concentric cylinders. A cross-section of the CFT is shown in Fig. 3.8. Each cylinder supports doublet layers: one parallel to the beam and one that is oriented at a stereo angle of  $2^\circ$  with respect to the beam. The scintillating fibers are 860 microns thick and between 1.7 - 2.6 meters long. They are organized and mounted in 128 fiber ribbons which consist of two singlet layers. The CFT is further organized into 80 sectors for readout and trigger purposes. Table 3.4.2 gives some characteristics of the CFT parameters.

Layer	Radius (cm)	# fibers	Fiber pitch ( $\mu m$ )
A	20.1	2560	985.606
B	25.0	3200	981.300
C	29.9	3840	978.105
D	34.8	4480	976.101
E	39.7	5120	974.598
F	44.6	5760	973.429
G	49.5	6400	972.297
H	51.5	7040	919.610

Table 3.3: CFT geometry parameters.

The scintillation process is a multi step process. The fibers are 99% polystyrene (by weight) and contain two organic scintilating dyes: paraterphenyl (PHP) and 3-hydroxyflavone (3HF) [43]. The polystyrene absorbs energy from the ionizing radiation incident upon it. The relaxation time of polystyrene is slow so the organic dye PHP is added to the fiber. Through dipole interaction the PHP molecules are excited which then decay promptly back to their ground state radiating a photon within a few nanoseconds. However, since PHP emits light with a very short emission wavelength ( $\approx 340\text{ nm}$ ) the optical path length is very short, on the order of a few hundred microns. Therefore, a second dye (3HF) is used as a wavelength shifter by absorbing the light from the de-excitation of the PHP molecule and to a longer wavelength of  $\approx$

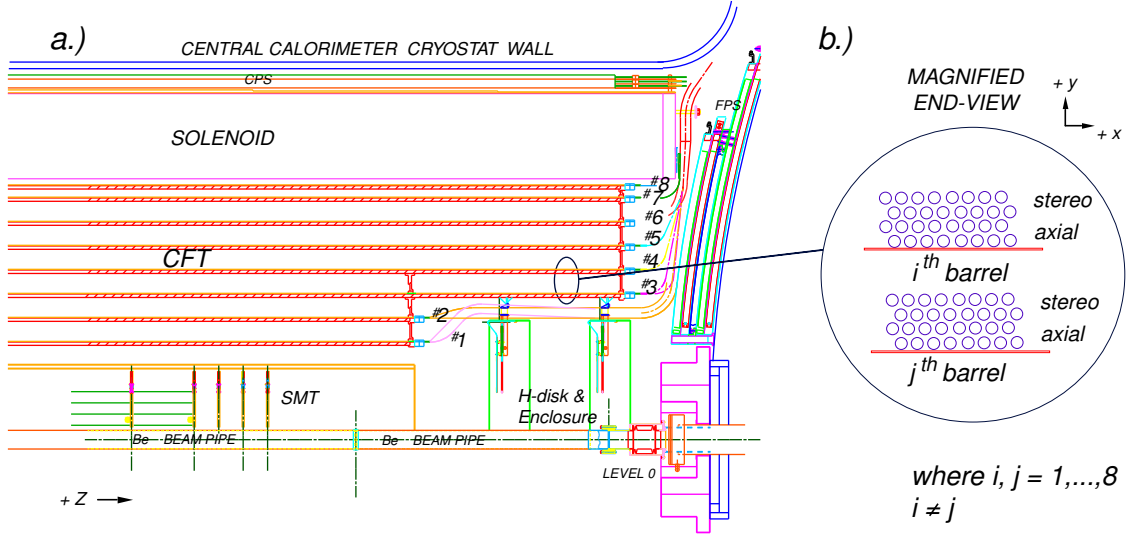


Figure 3.8: Cross Section of the CFT.

530 nm. This second dye was chosen since the optical path length in polystyrene is maximized in this region and is on the order of several meters. The long optical path length allows the scintillation light to travel the necessary distance to be detected.

One end of the fiber is coated with a reflecting material while the other end is attached to a clear fiber waveguide. This light travels down the fiber into the waveguide where a solid state photo-detector detects the photons. This photon detector has a high quantum efficiency, greater than 70%, and can detect a signal that consists of only a few photons. The CFT extends out to  $|\eta| < 2$ .

### 3.4.3 Solenoid

The solenoid immerses the tracking region around the beam pipe in a 2 Tesla highly uniform axial magnetic field. By bending the trajectory of the particles, the curvature of the track can be measured and the momentum of the charged particles can be ascertained. The solenoid is 2.73m in length and 1.42m in diameter [44]. The magnet runs at a current of 4825 A and stores 5.6 MJ of energy. In order to maintain such

a high current the magnet must be superconducting. The solenoid is constructed of two grades of superconducting high purity aluminum stabilized multi-filamentary Cu-NbTi cable and operates at 4.7 K.

### 3.4.4 Forward and Central Pre-showers

A general guiding principle of large collider detectors is to minimize the amount of material in the inner tracker. The presence of such material can cause the particles produced in the collisions to interact with the detector material and to lose energy in the process. The solenoid magnet discussed in the previous section represents the most significant amount of material in the inner tracking chamber. It is convenient to describe the amount of material in terms of the amount of energy a particle loses as it passes through it. The radiation length  $X_0$  is defined by the mean distance over which a high energy particle loses all but  $\frac{1}{e}$  of its energy [6]. The solenoid presents a significant amount of material to the particles exiting the tracking volume before entering the calorimeter which ranges from  $\approx 0.8$  to  $2.0 X_0$  depending on the glancing angle of the particle. If the particle has a larger value of  $\eta$  then it must propagate through more matter than a particle at normal incidence.

In order to accommodate the extra material that the solenoid introduces pre-shower detectors are installed just outside of the magnet and before the calorimeter. The purpose of these detectors is to help restore the electromagnetic energy resolution and particle identification. The detectors consist of lead absorbers and plastic scintillating tiles. Additional lead in varying thickness surrounds the solenoid to make the radiation length approximately  $2.0 X_0$  for all particle trajectories.

The central pre-shower consists of a layer of lead, and three layers of triangular scintillating strips. One layer is oriented parallel to the beam while the other two layers are oriented at a stereo angle of  $\pm 20^\circ$  with respect to the beam. Each of the

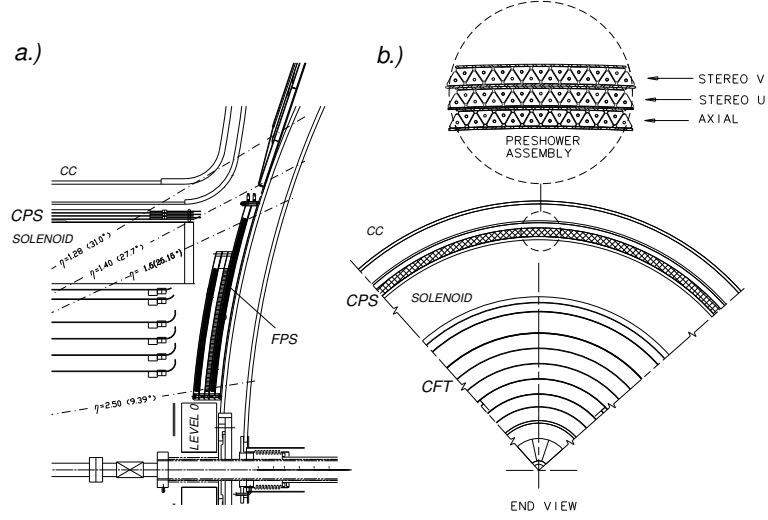


Figure 3.9: The forward and central pre-shower detectors.

three layers is divided into octants for purposes of construction and triggering. The triangular strips have a base of  $9.0\text{mm}$  and a height of  $4.5\text{mm}$ . The scintillation light is collected and sent through fibers to readout electronics.

The forward pre-shower is designed to aid electron identification in the forward region of the detector and covers the region:  $1.5 < |\eta| < 2.5$ . The placement of the detector matches the electromagnetic calorimeter in the end cap calorimeter discussed in the next section. Figure 3.9 shows a cross-section of the DØ forward tracking region and indicates the position of the forward and central pre-showers. The detector is comprised of four layers of scintillators of similar design to the central pre-shower. The layout has two layers of scintillators at opposing stereo angles of  $22^\circ$  followed by an absorbing layer of lead with a thickness equivalent to 2.0 radiation lengths. Another two layers of scintillators with the same stereo angles are mounted between the lead and the cryostat of the end cap calorimeter.

### 3.5 The Calorimeter

The calorimeter [41] , as shown in Fig. 3.2, encloses the central tracker and is divided in three major assemblies: one central calorimeter (CC) and two end calorimeters (EC). As shown in Fig. 3.10 the calorimeter is composed of a large number of modules. Each of these modules consists of interleaved layers of absorber plates and signal boards. The active material of the calorimeter, liquid argon, fills the gap between the two layers. A schematic of the calorimeter cell is shown in Fig. 3.11. The central calorimeter extends out to  $|\eta| < 1.2$  while the end calorimeters cover the region  $1.1 < |\eta| < 4.5$ . The central calorimeter is roughly toroidal and consists of several layers of cells: 32 electromagnetic (EM) layers, 16 fine-hadronic (FH) layers, and 16 course-hadronic (CH) layers. As is indicated by their names, the EM layers are constructed to contain electromagnetic showers while the hadronic layers measure and contain the hadronic showers. Like the central calorimeter, the EC is composed of layers of three types of modules, however the geometry is quite different as shown in Fig. 3.10. In both the CC the cells have dimension of  $\Delta\eta \times \Delta\phi = 0.1 \times 0.1$  except in the third EM layer where the shower maximum occurs and the segmentation is twice as fine. Table 3.4 indicates many of the most important parameters of the calorimeter.

Module Type	EM	FH	CH
Rapidity Coverage	$\pm 1.2$	$\pm 1.0$	$\pm 0.6$
Number of Modules	32	16	16
Absorber	Ur	U-Nb	Cu
Absorber Thickness ( <i>mm</i> )	3	6	46.5
Argon gap ( <i>mm</i> )	2.3	2.3	2.3
Total Radiation Lengths	20.5	96.0	3.2
Total Nuclear Absorption lengths	0.76	3.2	3.2

Table 3.4: Parameters of the Calorimeter.

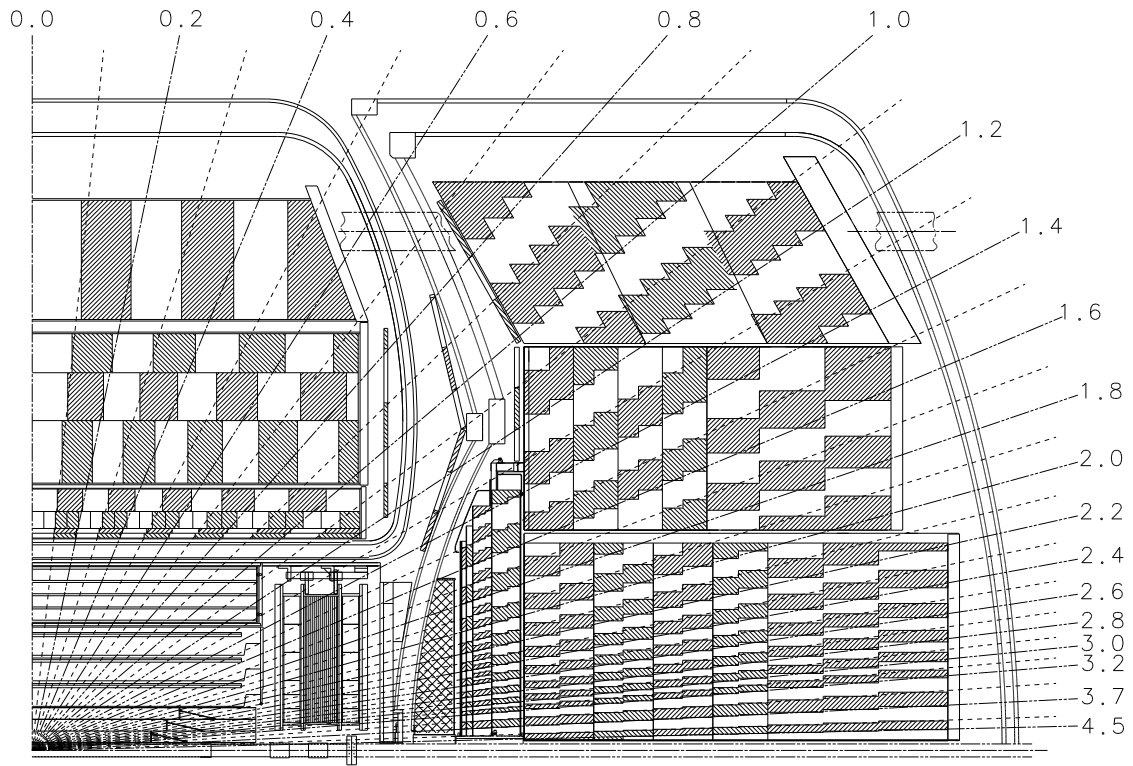


Figure 3.10: Cross Section of a Quarter of the Calorimeter

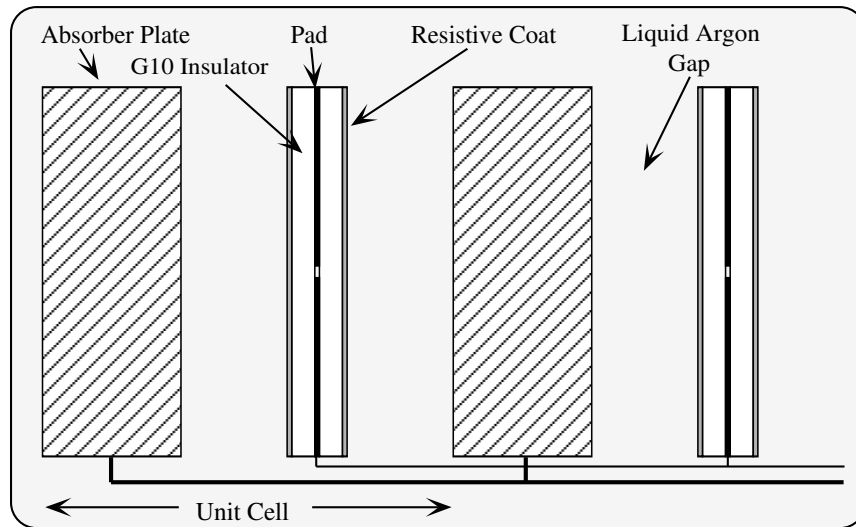


Figure 3.11: Schematic view of a Calorimeter Cell.

The function of the calorimeter is to measure the energy of the particles by inducing electromagnetic and hadronic showers. When traversing material high energy electrons and photons lose their energy through ionization and *bremsstrahlung* (breaking radiation). Above a critical energy [6] *bremsstrahlung* is the dominant process.

$$E_c = \frac{(800 \text{ MeV})}{Z + 1.2} \quad (3.6)$$

Where  $Z$  is the atomic number of the material. An electromagnetic shower begins when, in the presence of material, an electron radiates a photon. The photon pair produces an electron-positron pair, both of which can radiate photons again in turn. As this process repeats itself a single high energy electron ‘converts’ into a shower of many lower energy particles traveling in the direction of the initial incident electron. Clearly this cycle can also begin if the initial particle is a photon as well.

Hadronic particles which enter the calorimeter interact inelastically with the nuclei of the absorbing layers. These interactions produce mostly pions and nucleons which can collide inelastically with other nuclei. In a similar manner, a hadronic shower is initiated when a high energy hadron enters the calorimeter. The characteristic length scale,  $\lambda_I$ , is roughly independent of energy and depends on the density and the weight of the material as given by [6]:

$$\lambda_I = 35 \text{ g cm}^2 A^{1/3} \quad (3.7)$$

where  $A$  is the atomic weight of the material.

The heavy absorber layers present a thick layer of material for the energetic particles to interact with. The liquid argon layers serve as the active medium for ionization from the showering particles. The energy is sampled by measuring the amount of ion-

Term	C.C. electron	C.C. $\pi^\pm$	E.C. electron	E.C. $\pi^\pm$
Noise (N)				
Sampling (S)	14.8%	47.0%	15.7%	44.6%
Constant (C)	0.3%	4.5%	4.5%	3.9%

Table 3.5: Resolution Terms for the Calorimeter.

ization in the liquid argon. The electromagnetic section of the calorimeter contains 65.6 *mm* of uranium which represents  $\approx 20$  radiation lengths. Hence, the majority of the energy from the electromagnetic showers is contained within the electromagnetic section of the calorimeter. Since the characteristic length scale of hadronic showers is much longer than that of an electromagnetic shower hadrons deposit most of their energy in the hadronic calorimeter.

The resolution of a sampling calorimeter,  $\sigma_E$ , can be written as [6] :

$$\left(\frac{\sigma_E}{E}\right)^2 = C^2 + \frac{S^2}{E} + \frac{N^2}{E^2} \quad (3.8)$$

where C is a constant term, S is a sampling term, and N is a noise term. The constant term arises from the calibration of the detector. The sampling term reflects the fact that only a certain fraction of the energy is deposited in the active medium of the detector. Hence, there are statistical fluctuations which degrade the resolution. Finally, the noise terms come from noise in the electronic readout and Uranium decays. The current value of these parameters is indicated in Table 3.5.

## 3.6 Muon Detectors

Muons with energies that are typical of processes at the Tevatron interact with detectors predominantly through ionization. Because of the muon's larger mass, *bremstrahlung* does not play an important role in energy loss until the muons have



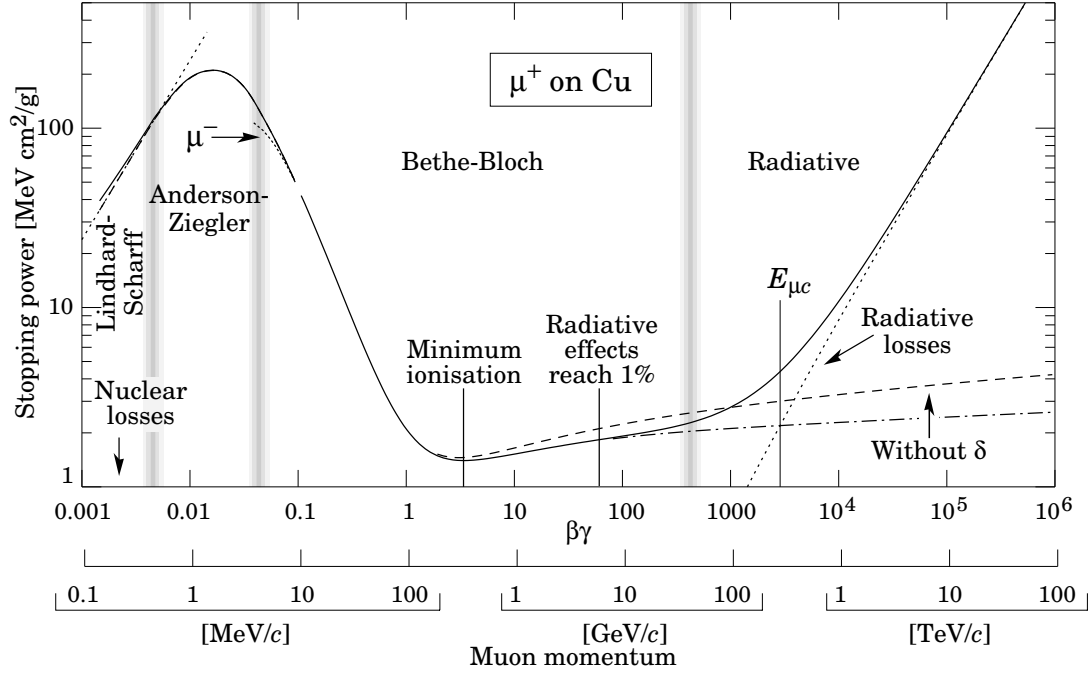


Figure 3.12:  $-\langle \frac{dE}{dX} \rangle$  as a function of muon momentum on Copper.

energies with several hundred GeV [6]. The energy loss by a heavy particle is given by the Bethe-Bloch equation [6]:

$$-\frac{dE}{dx} = K z^2 \frac{Z}{A} \frac{1}{\beta^2} \frac{1}{2} \left[ \ln \frac{2m_e c^2 \beta^2 \gamma^2 T_{max}}{I^2} - \beta^2 - \frac{\delta}{2} \right] \quad (3.9)$$

where  $K = 4\pi N_A r_e^2 m_e c^2$ ,  $A$  is the atomic mass of the absorber,  $\beta = \frac{v}{c}$ ,  $Z$  is the atomic number of the absorber,  $T_{max}$  is the maximum kinetic energy that can be imparted to an electron during a collision,  $I$  is the mean excitation energy of the atoms in the absorber,  $\delta$  is a density effect correction to the ionization loss,  $r_e$  is the classical radius of an electron,  $N_A$  is Avogadro's number,  $c$  is the speed of light, and  $\gamma = \frac{1}{\sqrt{1-\beta^2}}$ . The contributions to the energy loss per unit length by a muon deposited in Copper over a large momentum range are shown in Fig. 3.12.

The energy range of muons produced for typical interactions at DØ lies in the

region of a minimum ionizing particle (MIP) in Fig. 3.12. Since muons interact as MIPs throughout the detector, they pass through the tracking detector elements and calorimeter depositing a small amount of energy in each and rarely shower. Because of the importance charged leptons play at a hadron collider and the fact that muons penetrate the calorimeter, DØ has an entire detector system dedicated to identifying muons.

The muon system is a spectrometer consisting of drift tubes and scintillators arranged around a 1.9 T toroid, see Fig. 3.13. The system is divided into central,  $|\eta| < 1$ , and forward,  $1 < |\eta| < 2$  detector regions. The central region is referred to as the WAMUS (wide angle muon system) while the forward region is referred to the FAMUS (forward angle muon system). In both regions, the system is organized in three layers of drift tubes and scintillators: A, B, and C (the central region B layer is composed of only drift tubes). The A layer is situated outside of the calorimeter and enclosed by the toroid magnet. The B and C layers are mounted outside of the toroid. This combination allows for a calculation of the muon momentum via a measurement of the curvature of the muon trajectory through the magnet.

### 3.6.1 Drift Tubes

The drift tubes are rectangular gas filled volumes with a sense wire strung taut through the center of the volume. Charged particles which pass through the volume ionize the gas and produce electrons and ions. The wire in the center of the chamber is held at a voltage with respect to the walls of the tube. This causes the electrons to move towards the sense wire. As the electrons are accelerated towards the wire, they gain energy and cause further ionization and produce an 'avalanche' of electrons which amplifies the signal. Figure 3.14 shows the geometry of the central drift tubes. The central drift tubes are constructed with extruded aluminum with a steel foil

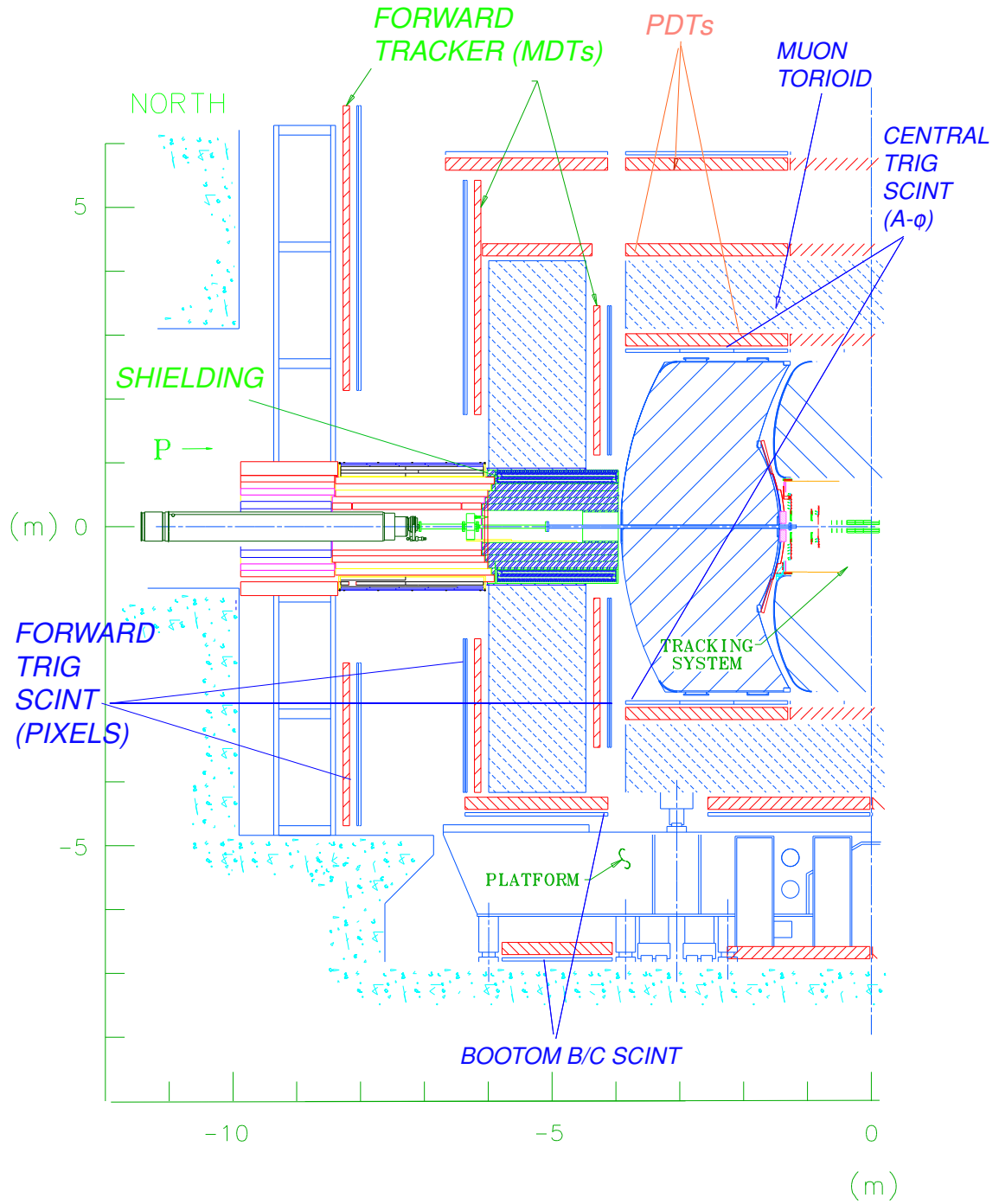


Figure 3.13: Overview of the muon system at DØ.

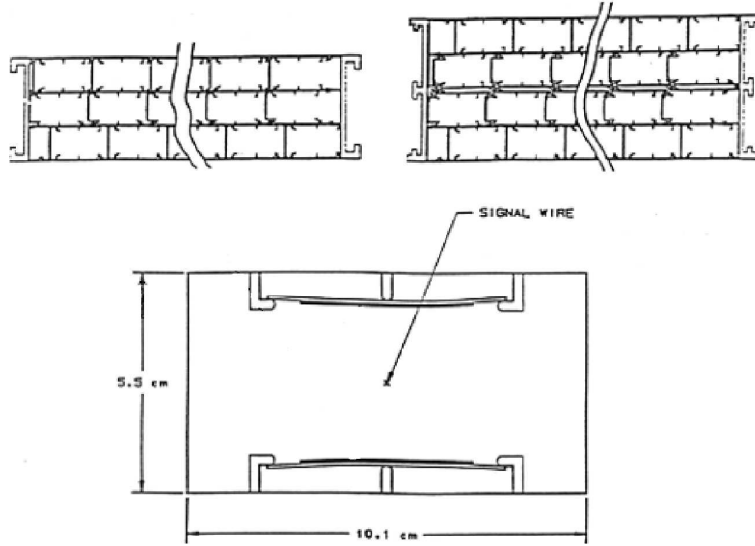


Figure 3.14: Muon Drift Tube Cross-Section.

coating while the central sense wire is a gold plated tungsten wire [46] . The gas is a composition of 80% argon, 10%  $CH_4$ , and 10%  $CF_4$ . The central drift tubes are  $5.5cm \times 10.0cm$  in cross-section and  $240cm$  in length. The forward drift tubes are much smaller having a cross section of  $1.0\text{ cm} \times 1.0$  with varying lengths. The gas mixture is also different in the forward region composed of 90%  $CH_4$ , and 10%  $CF_4$ . Table 3.6 shows an overview of some of the most important drift tube parameters.

The drift tubes are arranged such that the sense wire is parallel to the magnetic field and perpendicular to the particle's trajectory. By calibrating the drift time of the signal to the sense wire, a measurement of the arrival time of the pulse allows for a measurement of the radial distance of the particle to the wire. In the central region, the sense wires from two tubes have been joined so that a comparison of the arrival time of the pulse allows for a measurement of the particles trajectory along the direction of the wire.

### 3.6.2 Scintillators

Layers of scintillation counters aid in muon identification and are used for triggering events that contain muons. The detectors in the forward region are trapezoidal sheets of scintillator with a  $\phi$  segmentation of  $\approx 4.5^\circ$ . Rectangular counters with similar phi segmentation comprise the two scintillating layers in the central region [47]. Photo-multipliers are mounted on the detector which collect the light and convert the signal to an electrical pulse for further readout.

## 3.7 Triggering

The Tevatron provides  $p\bar{p}$  collisions at a rate of 2.5 MHz and the most prominent process is inelastic  $p\bar{p}$  scattering. However, the processes which are of greatest interest occur at much smaller rates. Since it is not technically feasible to record and process events at this rate, a procedure must be developed to decide which events to record. This process is called triggering.

### 3.7.1 Trigger Architecture

The trigger is a three staged pipelined system with each tier reducing the rate into the following tier. Progressively, each tier has more time to examine the events and therefore can make triggering decisions with increasing levels of sophistication [48]. The different triggering tiers are referred to as Level 1, 2, and 3 (L1, L2, L3). With the exception of the muon trigger (which also has inputs from the L1 track trigger), the L1 triggers are based upon isolated detector elements: tracking, calorimeter, and muon. Figure 3.15 shows an overview of the first two trigger levels with the specified design rates of each level. Each of the L1 trigger elements report their findings to

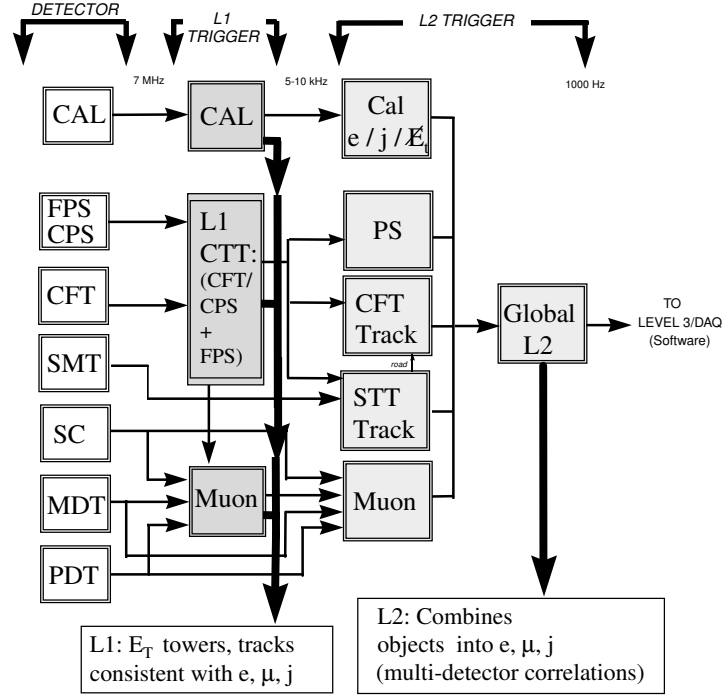


Figure 3.15: Level 1 and L2 Trigger Architecture: The horizontal arrows denote information flow.

the L1 Framework (L1FW) upon each beam crossing. The L1FW is responsible for collecting the information from each of the L1 trigger elements and making the global decision to accept or reject the event. In order to insure that the L1 trigger is dead-timeless, each front-end digitizing crate has sufficient memory to buffer 32 events. The L1 system can support 128 separate L1 triggers or trigger bits. Each bit is pre-programmed to require a specific combination of trigger terms. These trigger bits are determined by custom hardware and firmware built out of a series of field programmable gate arrays (FPGAs).

If the L1TW issues an accept, the event data is digitized and moved into a series of 16 event buffers to be analyzed by L2. The L1 trigger system is designed to be able to handle an accept rate of 7.5 MHz and the L2 input rate is designed for rates up to 10 KHz. The L1 input rate is dictated by the crossing frequency of the particle

bunches in the Tevatron. As of the writing of this thesis, the Tevatron bunch crossing rate is 2.5 MHz. As well, a more typical maximum L2 input rate is around 1.5 KHz.

### 3.7.2 L1 Trigger Elements

#### Track Triggers

The central tracking trigger (CTT) in the central fiber tracker (CFT) is based upon recognition of hit patterns in the axial fibers. As discussed in section 3.4.2 the  $\phi$  segmentation of the CFT is  $4.5^\circ$ . There are eighty of these segments which form trigger sectors for the CFT. The digitized signal from the light collection from particles which transverse these sections are fed into VME cards which have FPGA's which search for tracks via pre-programmed look up tables (LUTs). Each track candidate is identified by its trigger sector, relative  $\phi$  within a trigger sector, momentum, and direction of curvature. Although currently unused, the system also can hold information from corresponding hits in the pre-shower detectors. These L1 track candidates are organized by further hardware to take part in the global L1 trigger decision, along with being passed to the muon trigger and silicon track trigger (STT).

#### Muon Triggers

The muon L1 trigger is based upon the scintillation counter (SC) information, proportional drift tube (PDT) hits, and input from the L1 track trigger. The segmentation of the muon scintillators was chosen to match that of the trigger sectors of the CFT. From the hit information in the muon system and seeded by the tracks from the L1 track trigger, the muon trigger finds muon candidates via combinatorial logic performed in FPGAs. High  $p_T$  tracks are also required to pass cosmic ray veto scintillation counters (cosmic rays originating in the high atmosphere produce muons

which penetrate the DØ detector). Cosmic rays are rejected based on their timing information relative to the beam crossing. As well, the majority of cosmic rays pass through the detector at oblique angles which are inconsistent with originating from the center of the interaction region.

### Calorimeter Triggers

As discussed in section 3.5 the calorimeter is constructed by cells which form projective towers. Trigger towers are formed using  $\Delta\phi \times \Delta\eta$  of  $0.2 \times 0.2$ . Triggers are formed by requiring that the energy deposited in trigger towers are above pre-set levels in one or more trigger towers. A total of sixteen threshold sets are available. As well, additional trigger terms can be constructed from global quantities in the calorimeter from these trigger towers such as: total energy, total energy projected in the transverse plane, and ‘missing energy’ or energy imbalance in the transverse plane.<sup>b</sup>

### 3.7.3 L2 Trigger Overview

The L2 trigger is designed to reduce the event rate by up to a factor of 10. In order to accomplish this, the task is split into two stages: subsystem preprocessing and a final L2 global processor. At the first stage, the data from each of the sub-detectors is examined in greater detail and more precise information about the event is ascertained. In the second stage it is the first opportunity to combined information

---

<sup>b</sup>Objects with high transverse momentum are of great interest at collider physics since they can indicate the decay of heavy objects produced in the collision. Energy is of course a scalar and hence does not have direction. However, the calorimeter samples the energy deposited from the interactions of high energy particles. Further, since high energy particles typically have almost all of this energy from their motion or momentum and not for their mass, the energy is often a very good approximation to the momentum of the high energy particle. Hence, it is common to refer to the quantity ‘transverse energy’, or  $E_T$ . It is typically taken for granted that it is understood that one is referring to the approximate transverse momentum or  $p_T$  of the object.



from the entire detector. This allows the development of triggers that use multiple detector elements to obtain more precise information about objects in the event. With one notable exception (the STT), the processing is done almost entirely in software in processor boards which collect information from the L1 triggers. For example, L2CAL, or the calorimeter preprocessor collects information from all the L1 trigger towers which then are used to build simple jet and electron candidates from clustering algorithms. For these objects the preprocessors calculate the position, energy, and test them for shape and transverse energy requirements. The L2 CTT uses the larger time budget allotted to make a more detailed and precise calculation of the track parameters from the L1 CTT tracks. Similarly, the muon preprocessor improves muon identification by calculating the transverse momentum, rapidity, azimuthal angle, and 'quality' of the muon candidate.

### 3.7.4 The Silicon Track Trigger

The silicon track trigger (STT) performs online track reconstruction using data from the silicon micro-strip detector (SMT) and is seeded by tracks from the L1CTT [49], see Fig. 3.16. L1CTT track candidates are used to define projective 'roads' inside the silicon. Only the axial cluster of strips which are inside  $\pm 2$  mm roads are associated with the CTT track candidates. The SMT detectors are arranged into 12 sectors which  $30^\circ$  in azimuth, although they slightly overlap. However, since 98% of the tracks are contained within one  $30^\circ$  sector, the STT treats the tracks in the twelve sectors independently.

The STT design is significantly different from the rest of the L2 trigger system. This is dictated by the fact that there is no L1 trigger component which utilizes the silicon detector. Hence, the STT must receive and process the digitized data from all the silicon detectors which are used in the trigger. Finally, and most importantly,

Parameter	Central Drift Tubes	Forward Drift Tubes
Wire Step	130 <i>mm</i>	10 <i>mm</i>
Wire Thickness	0.6 <i>mm</i>	0.6 <i>mm</i>
Cathode Material	Extruded Al	Al, Stainless Steel
Wire Material	W-Au ( 96% : 4%)	W-Au ( 96% : 4%)
Wire Diameter	50 $\mu m$	50 $\mu m$
Gas Material	90% $CH_4$ , 10% $CF_4$	80% Ar, 10% $CH_4$ , 10% $CF_4$
Gas Gain	$1.1 \times 10^5$	$2 \times 10^5$
Cathode Potential	2500 V	3100 V
Maximum Drift Time	500 <i>ns</i>	60 <i>ns</i>

Table 3.6: Parameters of the Muon Drift Tubes.

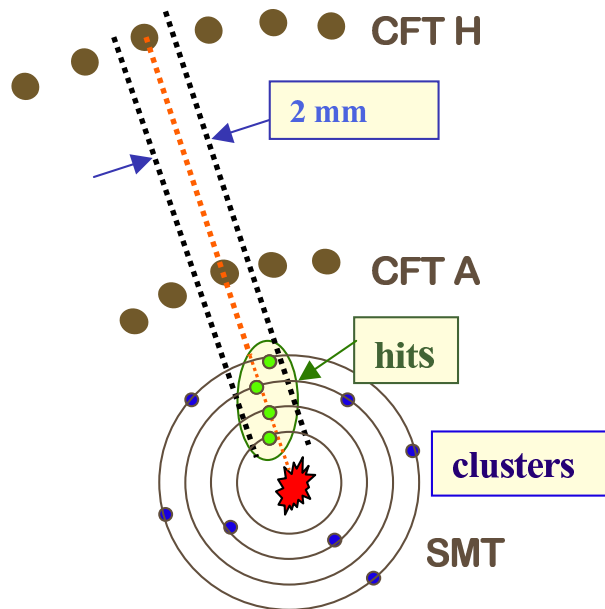


Figure 3.16: Conceptual Design of the Silicon Track Trigger.

the STT fits the tracks from the CTT with the information from the silicon tracker to obtain more detailed information of the tracks at the trigger level.

Data input from the Level 1 CTT and SMT detectors is via optical fibers which plug into custom receiver cards located in the rear card cage of the crate which houses the trigger electronics. The data is processed via FPGA's and DSP's on the logic daughter boards. These three design goals highly influence the system architecture whose backbone is comprised of three custom digital boards which perform these functions. The three components of the silicon track trigger are: the Fiber Road Card (FRC), Silicon Trigger Card (STC), and Track Fit Card (TFC). Each of these modules is designed to plug into a common motherboard for use in a standard VME crate. Data communication between the three modules is achieved via custom mezzanine cards which use Low Voltage Differential Signal (LVDS) cables to transfer data between the cards. As well, each board communicates with a common daughter board that buffers and manages the readout of the data to the data acquisition system. The daughter boards communicate with the buffer readout, the link boards, and the VME backplane via three PCI buses. One STT crate processes data for two  $30^\circ$  sectors (there are six STT crates). The layout of the STT crate is shown in Fig. 3.17.

### **Fiber Road Card**

The Fiber Road Card (FRC) consists of four main elements: the road receiver, the trigger receiver, the road data formatter, and the buffer manager. The road receiver accepts data via optical cables from the L1CTT. It receives trigger information from the framework via a mezzanine card. The road data formatter reformats the CTT data and then broadcasts roads and trigger signals via the LVDS link cards to the other daughter boards. The buffer manager handles the readout to the data acquisition system by controlling the buffer cards. Upon every L1 accept data is received

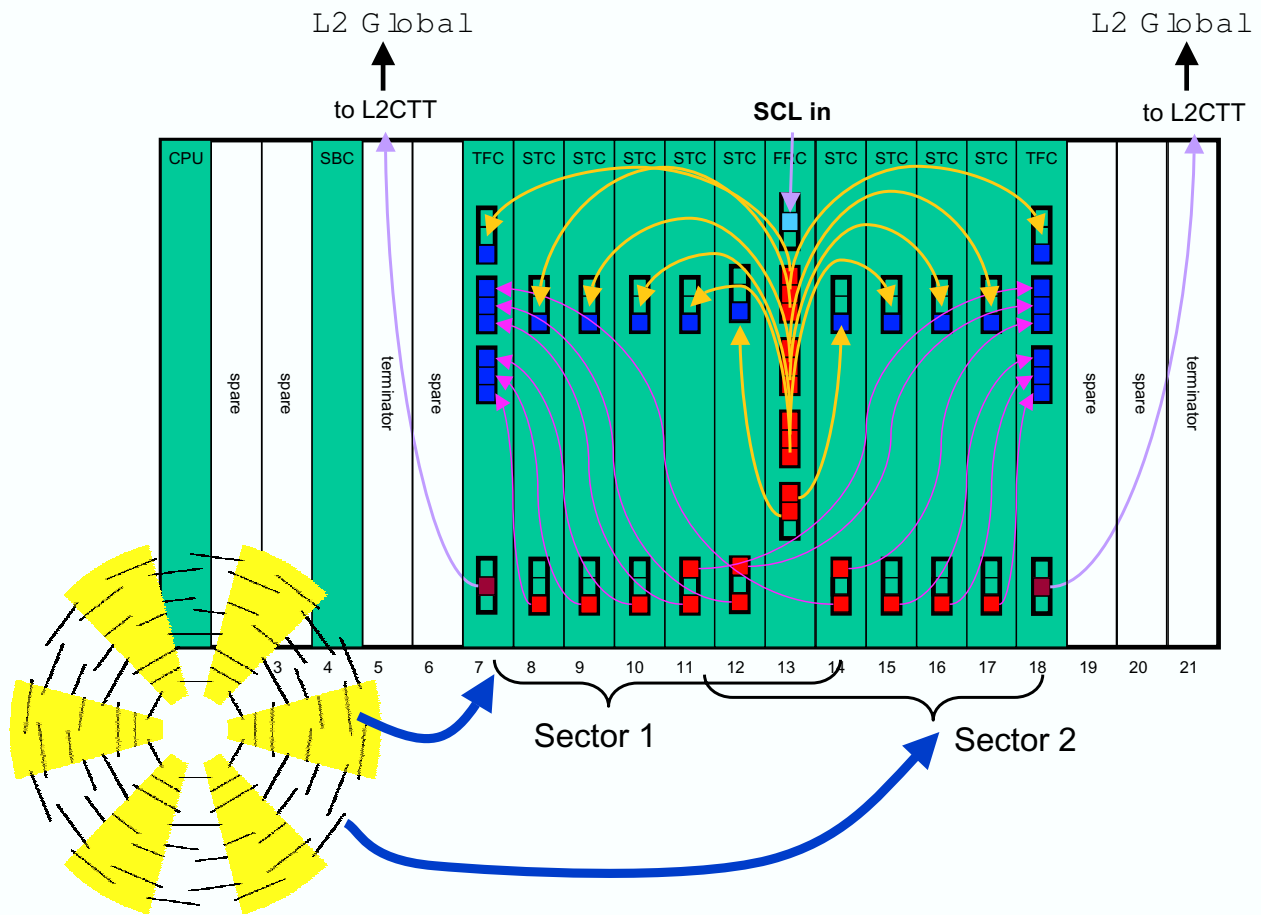


Figure 3.17: Schematic view of a STT Crate. The overlaid cross-section of the silicon micro-strip detector shows the sectors which are processed by the crate.

and processed by all the daughter cards. Data for readout is transferred to the buffer card for each event the system receives. Based on the L2 trigger information, the buffer manager sends control signals to the buffer cards either for readout or for the event to be rejected and overwritten.

### **Silicon Trigger Card**

As mentioned above, because the STT receives the digitized output of the silicon detector directly, the Silicon Trigger Card (STC) must process all the data axial strip silicon data. For this reason, there are nine STCs per crate each of which processes the data from eight detectors. Using downloaded LUTs the STCs mask out noisy and dead silicon strips and perform a strip by strip gain and offset correction.

Next the STCs execute a fast clustering algorithm on the data. The clustering algorithm contains two thresholds a strip and cluster threshold. After gain and offset correction, each strip Analog to Digital Count (ADC) is compared to the strip threshold. If it is above the threshold it is allowed to start a cluster. Once a cluster is started, it ends when a contiguous strip is below the strip threshold. During the clustering, the maximum value of the cluster strip's ADC count is stored. If this maximum value is above the cluster threshold the cluster is retained otherwise it is discarded. The next step involves calculating a cluster centroid. Since this is done on-line, another simple and fast algorithm has been implemented. The centroid is seeded with the cluster maximum. Then the two strips on either side of the cluster maximum along with the strip that contains the cluster maximum are used to calculate an offset. This offset is then added (or subtracted) from the cluster maximum to form the cluster centroid. The final step of the processing is to associate the cluster centroids with the L1CTT tracks. This is done by pre-computed LUTs. If the cluster centroid is within  $\pm 2mm$  of a CTT track it is kept, otherwise it is discarded. Note

that the same cluster centroid can be associated with multiple CTT tracks. The list of centroids associated with CTT tracks is transferred to the Track Fit Card via an LVDS link. The STC also prepares data for readout for the data acquisition system and is used to monitor the STC algorithm performance.

### Track Fit Card

The Track Fit Card (TFC) receives L1CTT tracks over an LVDS link from the FRC and the centroids of silicon clusters associated with those tracks from the STCs. There are two TFCs per crate, which fit tracks in different  $30^\circ$  sectors. The data received is then processed and attempts to fit the CTT tracks using silicon data are made. The results are transferred to a preprocessor to be combined with the tracks from the other crates and sorted before being transferred to L2 global. As well, information is prepared for readout to the data acquisition system for monitoring the track fitting performance.

The data received from the STCs is in silicon hardware coordinates (detector and strip number). The first step is to convert these into  $r - \phi$  coordinates more suitable for track fitting (done by pre-computed look-up tables). The hits in the inner and outer layer of the central fiber tracker are used in the fit. Then the algorithm looks at the silicon hits associated with that CTT track and in each layer selects the hit which is closest in  $r - \phi$  to the track, assuming the track came from the interaction point. If there are silicon hits in all four layers and the  $\chi^2$  is larger than a predetermined number then the silicon hit which contributes most to the  $\chi^2$  is removed and the track is refit. The track is fit to the form:

$$\phi(r) = \frac{b}{r} + \kappa r + \phi_0 \quad (3.10)$$

where  $b$  is the impact parameter with respect to the center of the detector,  $\kappa$  is the track curvature, and  $\phi_0$  is the azimuthal angle of the tangent to the track at the point of closest approach. The  $\chi^2$  of the fit is defined as:

$$\chi^2 = \sum_{i=\text{hits}} \left| \frac{\phi_i - \phi(r)}{\sigma_i} \right| \quad (3.11)$$

where  $\phi_i$  is the azimuthal position of a hit,  $\phi(r)$  is the azimuthal position of a hit predicted by the fit in equation 3.10, and  $\sigma_i$  is the resolution on the azimuthal position of the hit.

Nominally, the beams are made to collide at the center of the detector. However, it is common for the beam spot to be slightly off-centered. Ignoring this information in the hit selection and track fitting was seen to significantly degrade the performance of the STT. Therefore, with the beam spot (which is measured by on-line tracking) is downloaded to the TFC. A correction for the beam position offset is used in both the final hit selection in the TFC and also when fitting for the parameters in equation 3.10.

### 3.7.5 Level 3 Trigger and Data Acquisition System

The third level of triggering is executed completely on a dedicated computer farm which performs a fast reconstruction of the event [50]. This allows the highest level of triggering to be done on high level 'physics' objects such as electrons, muons, and jets. The L3 farm computers run a modified version of the full event reconstruction. The trigger decision must be made within 100ms and has an output bandwidth limitation of approximately 50 Hz. Upon a L2 accept, the data for that event from each of the readout crates is transferred via a large Ethernet switch. A program (the L3 supervisor) monitors the performance and event buffers of the individual Level 3

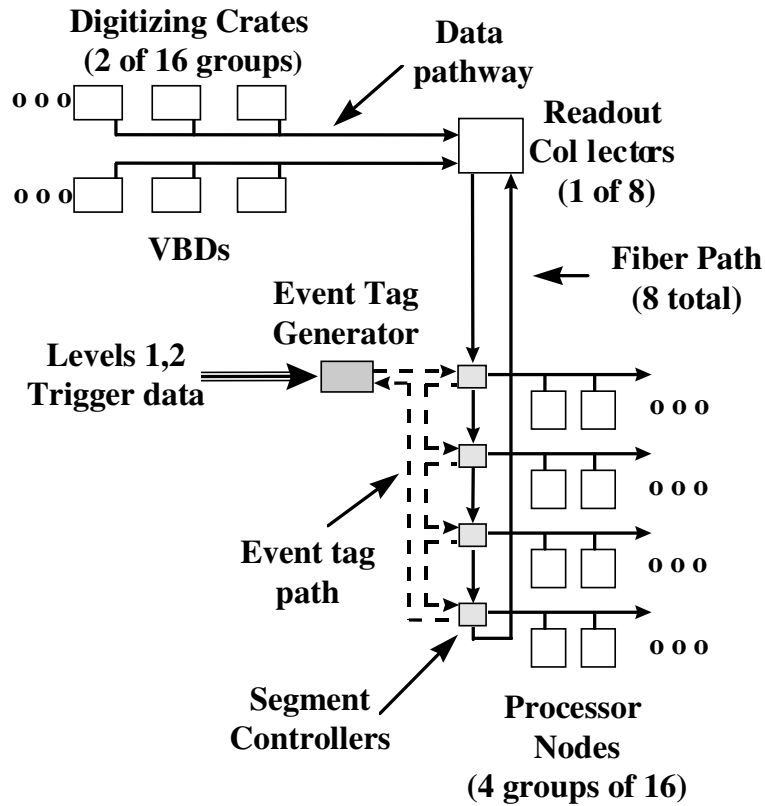


Figure 3.18: Overview of the Level 3 Trigger and Data Acquisition System.

computer nodes and decides which node each event will be sent to. An overview of how data is transferred from readout crates to the Level 3 nodes is shown in Fig. 3.18.

The level three nodes run essentially two programs: an event builder and an event filter. The event builder is told by the level three supervisor which readout crates to expect data from. If the event builder does not get a full event from each crate the event is discarded. The second program runs the event reconstruction and an event filter. The event filter is a list of filters each of which place different requirements on the event. If the event passes any of the event filters, the event is accepted and written to tape for offline analysis.



## Chapter 4

# EVENT RECONSTRUCTION

*'Science is facts; just as houses are made of stones, so is science made of facts; but a pile of stones is not a house and a collection of facts is not necessarily science.'*

Henri Poincare

When an event is recorded by the DØ detector it consists of a large collection of analogue to digital counts (ADC) from all of the detector systems. In order to perform an analysis of the underlying physics this raw information must be processed to reconstruct the properties the physics objects in the event. This chapter discusses the process of reconstructing these objects from the raw data.

### 4.1 Central Tracking Reconstruction

As discussed in chapter 3, there are two major subsystems for detecting charged particle tracks: the silicon micro-strip tracker (SMT) and the central fiber tracker (CFT). When a charged particle passes through a particular layer of the SMT or CFT, several detector elements can register the presence of the particle. Before track fitting, the data is first compressed by forming clusters of hits in the tracking detectors.

### 4.1.1 Clustering

Since the silicon strips are capacitively coupled, when a charged particle passes near one of the strips it often happens that charge accumulates on several contiguous strips. After reading out the detector, a gain and offset correction is applied to each strip to correct for strip to strip variation in detector performance and electronic readout. The clustering algorithm proceeds as follows: as each new strip which has an ADC count above a threshold (8 ADCs) is added the position of the strip is checked to ensure that geometrically the strip is next to the previous one. If it is the neighboring strip and it is above the threshold, then the strip is added to the original cluster. If the ADC count is below the threshold it is ignored, and if the strip is not a neighbor a previously started cluster a new cluster is started. The position of the cluster is pulse height weighted by the formula [51]:

$$\bar{n} = \frac{\sum n_i w_i}{\sum w_i} \quad (4.1)$$

where  $n_i$  and  $w_i$  are the strip numbers and ADC counts for the  $i$ th strip, respectively.

The centroid of the cluster is then given by:

$$u = u_1 + (\bar{n} - 1)p \quad (4.2)$$

where  $u_1$  is the first strip of the cluster,  $p$  is the pitch of the strips, and the -1 is needed because the strip numbering starts with 0.

Clustering in the CFT is similar. In this case, the light yield in each fiber is converted to an ADC count. The light yield first is calibrated for gain and pedestal information on a fiber by fiber basis obtained by using light emitting diodes with the same light output. The light yield is calibrated by the formula:

$$light\ yield\ (photoelectrons) = \frac{ADC - pedestal}{gain} \quad (4.3)$$

The fiber's ADC count is then compared with a threshold which determines if the fiber has a hit or not. The threshold varies from sector to sector, primarily because the wave guides that read out the light vary in length (longer fibers lose more light). The threshold varies from sector to sector and layer to layer (between 1.4-1.5 photoelectrons) [52]. In the axial layers 1 photo-electron corresponds to 15 ADC counts while in the stereo layers it is 7 ADC counts.

Consecutive fibers that registered hits are considered in the same cluster. If there is a fiber or more separation then the previous cluster is ended and a new cluster is started. The position of the centroid is simply taken as the half way point between the two fibers which define the starting and ending point of the cluster.

### 4.1.2 Tracking

After cluster identification, the next step is to combine the cluster information from different layers into track candidates. The most difficult step is identifying which clusters should belong to which tracks. Tracking proceeds along two steps [53] [54]:

- Construct track candidates.
- Filter out the tracks that are most likely noise or 'ghost' tracks (false tracks reconstructed from hit patterns of real charged particles due to combinatoric ambiguities).

The initial track hypothesis is constructed from three clusters in the SMT barrels or disks. Selection of the hits starts with the inner most layer. This is motivated by the fact that the particles can interact or scatter in the detector material and it

is important to know the track parameters at the distance of closest approach. As well there are significantly less combinatoric possibilities working from the interaction point outward. The first measurement can be a cluster in any of the SMT layers. The second measurement is then selected in any following layer provided that the axial angle between the two clusters is less than  $0.08^\circ$ . For selection of the third layer, a circle of 30 *cm* of the constructed track candidate is drawn (which corresponds to a transverse momentum of 180 MeV in the 2 Tesla magnetic field) and clusters within this circle are considered as possible track points.

As well two additional requirements are made: the impact parameter with respect to the beam spot must be less than 2.5 *cm* and the  $\chi^2$  of the resulting track hypothesis must be less than 16. The track building process is continued into the next layer and the expected crossing region is computed. Any hit within this expectation window is tried as a potential point on the track. Note that if in any layer there is more than one cluster that passes the requirements described above a new track candidate is formed. If no cluster is found within the expectation region, this is considered a missed layer for that track. Further there are three categories of missed layers: inside misses (where the layer with the missing cluster is between the two layers where a cluster was found), forward misses and backward misses (where the layer with the missing cluster is forward or behind the track hypothesis).

Track candidates are then required to satisfy the following conditions:

- Clusters on at least four detector layers (SMT or CFT) with both axial and stereo clusters.
- No more than three inside misses.
- No more than six forward or background misses.
- No more than two misses inside the SMT.

- $\frac{N_{clusters}}{5} \geq N_{misses}$ .
- For hypothesis with at least one inside miss there are no more than four inside and forward misses or three inside and backward misses.

The next step is to decide which of the track candidates should be kept as final tracks. This proceeds by the following algorithm. First an ordered list of track candidates is constructed. The tracks with the largest number of clusters are placed first. If two tracks have the same number of clusters, the track candidate with the smallest number of total layer misses is placed first. If the two tracks candidates also have the same number of misses, the track with the lower  $\chi^2$  is placed first. Then the ‘shared hit’ criterion is used to decide which of the track candidates are retained. In the shared hit criterion two or more track candidates can share the same clusters. If the cluster is part of an already accepted track it is considered shared if another track candidate also uses the same cluster. If the number of total clusters in a track candidate is denoted  $N_{total}$  and the number of shared clusters is denoted  $N_{shared}$  then the track candidate is kept if either of the following two criterion are satisfied:

- $N_{shared} \leq \frac{2}{3}N_{total}$
- $N_{shared} \leq \frac{1}{5}N_{total}$  and  $N_{total} - N_{shared} > 3$

In order to further reduce false tracks another step is taken. From the tracks kept from the procedure above, the primary vertex (where the hard scattering event occurred) is reconstructed using the above final track list. Each track that has a small impact parameter with respect to any primary vertex is augmented with two additional ‘clusters’ and the tracks are reordered and selected by the track selection procedure again. This helps to insure that tracks candidates that are most likely from the primary vertex are kept.

In the description above, SMT clusters are needed to start track candidates. Because of non-functioning detectors, and inefficiency, the tracking algorithm also considers tracks with only CFT clusters. In order to reduce the number of false tracks, the procedure for finding tracks starting with the SMT is first used to find the primary vertices of the event. Then a second round of track finding begins, this time searching for tracks starting with the inner most layer of the CFT. The process to define the track candidate is the same as the first steps in tracking algorithm beginning with the innermost layer of the SMT. The construction continues to the outermost layer of the CFT with the additional requirement that the impact parameter of the CFT track is within 1.5 *cm* of some primary vertex. Then the CFT track is extrapolated into the SMT and any SMT clusters that can be associated with the track are kept with the track. This procedure uses the same projection method described above.

## 4.2 Calorimeter Reconstruction

As discussed in chapter three, the calorimeter signal consists of a collection of electrons from the ionization of liquid argon. The signal is then digitized and sent through a series of readout electronics. As in the case of the central tracker, the first step is to correct (on a cell by cell basis) the number of ADCs due to intrinsic differences in cell to cell response variation and electronic readout. The next step is to convert the ADC into an energy deposition in GeV. The calibration comes from both test beam results (where particles of known energy were targeted on portions of the calorimeter [55]) and *in-situ* calibration (reconstructing the invariant mass of particles whose mass is known to much higher precision than the resolution of the calorimeter [56]). After finding the deposition in each cell, the cell energies are summed in towers of equal  $\eta$  and  $\phi$ . While taking this sum, the high energy approximation is made such

that the particles are assumed to be massless. In this approximation, the energy and momentum are equivalent such that an 'energy four-vector' may be constructed [56] given by:

$$(E, E \sin \theta \sin \phi, E \sin \theta \cos \phi, E \cos \theta) \quad (4.4)$$

The towers are then assigned direction variables given by:

$$\phi = \frac{E_x}{E_y} \quad (4.5)$$

$$\theta = \tan^{-1} \left( \frac{\sqrt{E_x^2 + E_y^2}}{E_z} \right) \quad (4.6)$$

The tower energies and direction are then used in reconstructing the energies and directions of electrons, photons, and jets.

### 4.3 Muon Reconstruction

The process of muon reconstruction is similar to that of track finding, though somewhat simpler. Muon reconstruction proceeds through three steps [57] [58]:

- Hit Finding
- Segment Finding
- Track Fitting

### 4.3.1 Hit Finding

There are three different types of detectors in the muon system as discussed in chapter 3: proportional drift tubes (PDTs), mini drift tubes (MDTs), and scintillators. Since most of the PDT wires are paired, this allows a measurement of the drift time (the time it takes the signal to reach the sense wire) and the axial time (the time it takes the signal to move from the wire to be collected). In the MDTs the wires are not paired so the stored time is the sum of the drift and axial time: it is assumed that the ionizing particle went through the center of the MDT. The scintillators provide further timing information and are used to improve the position resolution of the hits. Again the ionizing particle is assumed to have hit the center of the scintillator.

### 4.3.2 Segment Finding

Segment Finding proceeds through several steps [59]:

- Creation of links between hits: links are formed between hits that are within 20 *cm* of each other, are not in the same plane, and are not from the same underlying wire hit. The location and direction of the resulting segment are calculated. In the central region, because of the large size of the drift tubes, the position of the hits on the segment depends on the angle of the segment. Therefore, after the segment direction is calculated the hit positions are then recalculated relative to the segment position. Finally, the segment direction is recalculated according to the new hit positions.
- Linking of segments: The next step is to try to link the local segments to form larger segments. The position and the direction of the segments are examined and if the pair are consistent with a straight line, the two are merged into a larger segment.



- Lining up with the Vertex: Next the primary vertex location is used and the the segment position is recalculated using the primary vertex as one point in the segment. Note that because of the toroid field, which bends the direction of the charged particle this is only applicable to the layer which is before the toroid, layer A.
- Matching B and C segments: Since there is no magnetic field between the B and C layers the particle should travel in a straight line. Segment matching between the B and C layer is then attempted to make larger segments with more precise information.
- Segment Filtering: A  $\chi^2$ , assuming a straight line path, is calculated for each possible segment. The segment with the lowest  $\chi^2$  in each octant is kept.

### 4.3.3 Track Fitting

The track fitting occurs in two steps: local track fitting and matching with tracks from the central tracker. Segments from the A layer and segments from the BC layer are fit to find a local muon track. The procedure takes into account the bending of the trajectory by the toroid field and the energy loss as the muon passes through the iron of the toroid [58]. The track is propagated step by step from the center of gravity of the BC layer to that of the A layer using circular helices. The result is a local muon track parameterized by the position and momentum at the A layer. The next step is to match the track with a track from the central tracker. The matching procedure takes into account the magnetic fields (solenoid and toroid) and multiple Coulomb scattering and energy loss in the toroid and the calorimeter by using the error matrix propagation [60]. The matching is performed and the distance of closest approach to the beam is computed.

## 4.4 Primary Vertex Reconstruction

The primary vertex is the location of the hard scattering event. Reconstructing the location of the primary vertex is done by examining the tracks found in the event. The reconstruction is done in three steps [61] [62]:

- track selection
- vertex finding
- vertex selection

The track selection is designed to find the tracks that most likely come from the primary vertex. Tracks with large impact parameter are typically produced by secondary particles which decay after being produced in the hard scattering event and travel a small distance. Therefore, the tracks from which the primary vertices are reconstructed are required to have small transverse impact parameter. Tracks are required to have clusters in two or more of the silicon layers,  $p_T > 0.5$  GeV , and a transverse impact parameter significance  $\frac{dca}{\sigma_{dca}}$  less than 3.0. In order to separate tracks that come from different interactions, the tracks are then clustered together in the z direction. Tracks that are within 2.0 cm of each other are clustered together. The tracks in each of the z clusters are then fit to vertices using a Kalman filter technique.

Once the clusters are fit to vertices, there is a list of vertices all of which could be the hard scattering interaction point. The vertex selection process is based on an algorithm to select the vertex which has the smallest probability to be from a 'minimum bias' interaction [63]. A minimum bias interaction is due to a soft interaction between the collision of a proton and anti-proton that results in a low transverse momentum transfer. These interactions are essentially due to non-diffractive inelastic

scattering. The essential idea is to select the vertex which most likely contained the hard scattering event.

For each track, the probability of the track coming from a minimum bias interaction is evaluated using the track  $p_T$ . Since higher  $p_T$  tracks are more likely to come from the hard scattering event, this probability is evaluated by studying the  $p_T$  spectrum from minimum bias interactions. As a measure of the probability for the vertex to be from a minimum bias event, one could simply take the product of the individual track probabilities. However, in this case the probability would depend on the number of tracks used in the calculation. In general, the larger the number of tracks used in the vertex, the smaller the probability. A definition of the probability for the vertex to be from a minimum bias interaction which is independent of the number of tracks is:

$$P_{min-bias} = \prod \sum_{k=0}^{N=k-1} \frac{-\ln P}{k!} \quad (4.7)$$

where  $P$  is the probability of an individual track to come from a minimum bias interaction and the index  $k$  labels the tracks. The vertex with the smallest probability of originating from a minimum bias interaction is taken to be the location of the hard scattering event.

## 4.5 Particle Identification

### 4.5.1 Electrons

Electrons, being charged particles, will interact with the SMT and CFT elements producing hits in both tracking detectors. Further, since the central region is immersed in a 2 Tesla magnetic field the trajectory of the particle will bend. As discussed

in chapter three, the primary loss of energy for electrons is through *bremsstrahlung* in the inner most part of the calorimeter.

The expected sources of background for electrons are:

- $\pi^0$  showers which overlap with a track from a charged particle.
- Photons which convert to  $e^+e^-$  pairs.
- $\pi^\pm$  which undergo charge exchange in the detector material.
- Fluctuations of hadronic shower shapes.

Electron identification begins by looking in the calorimeter. An electromagnetic cluster is defined to be a group of towers in the calorimeter with a cone of radius,  $R = \sqrt{\Delta\eta^2 + \Delta\phi^2} < 0.2$  around the highest energy tower. There are several parameters that can be used to characterize a shower in the calorimeter [64]:

- Electromagnetic Fraction (EMF): An electromagnetic shower is expected to deposit most of its energy in first few layers of the calorimeter. The EMF of a shower is defined by:  $f_{EM} = \frac{E_{EM}}{E_{tot}}$  where  $E_{EM}$  is the energy deposited in the electromagnetic calorimeter (as defined in chapter three) and  $E_{tot}$  is the total energy deposited in all layers.
- Isolation fraction: As opposed to hadrons which are typically found in jets of many particles, electromagnetic showers from electrons and photons are typically isolated from other particles in the calorimeter (except for accidental overlap with other particles). The isolation fraction is defined as:

$$f_{iso} = \frac{E_{tot}(R < 0.4) - E_{EM}(R < 0.2)}{E_{tot}(R < 0.2)} \quad (4.8)$$

- Central track match: Since electrons are expected to interact with the central detector, one expects a track from the electron which matches well with the information in the calorimeter. The track should point towards the direction of the electromagnetic shower and have a momentum which is consistent with the energy deposition in the calorimeter. A matching  $\chi^2$  is formed which is defined as:

$$\chi_{EM-track}^2 = \left(\frac{\delta\phi}{\sigma\phi}\right)^2 + \left(\frac{\delta z}{\sigma z}\right)^2 + \left(\frac{\frac{E_T}{p_T} - 1}{\sigma \frac{E_T}{p_T}}\right)^2 \quad (4.9)$$

- H-matrix: The development of an electromagnetic shower has several characteristics that are different from hadronic showers [6]. For example, the energy deposition is expected to maximize after about six radiation lengths. In order to characterize the shape of the electromagnetic shower, DØ uses seven variables: the fractional energy deposition in the four EM layers of the calorimeter, the total energy deposition in the EM calorimeter, the shower width in  $\phi$ , and how consistent the shower is with the z vertex position. In order to incorporate the shower information which indicates how consistent a given shower is with a true electromagnetic shower and which takes into account the correlations between the variables, the H-matrix is defined as [66]:

$$\chi_{hm}^2 = \sum_{i,j=1}^7 (x'_i - \bar{x}_i) H_{ij} (x'_j - \bar{x}_j) \quad (4.10)$$

where the  $x$ 's run over the seven input variables, the  $\bar{x}$  are the averages for Monte Carlo showers, and  $H_{ij}$  are the elements of the covariance matrix of the variables. True electromagnetic clusters will tend to have values of the shower shape variables which are close to the electron averages and hence have lower  $\chi^2$  than non-electromagnetic showers.

- **Electron Likelihood:** In order to maximize the efficiency and minimize the misidentification rate of electrons, a likelihood which combines several variables is used [64]. If the probability that a given shower is from a true electromagnetic shower is  $P_{sig}(x)$  and the probability that it is from background is  $P_{back}(x)$ , the likelihood ratio is defined as:

$$L(x) = \frac{P_{sig}(x)}{P_{sig}(x) + P_{back}(x)} \quad (4.11)$$

By construction when the shower is very signal like the likelihood approaches 1 and when the shower is very background like it approaches 0.

There are input variables are:

- $f_{EM}$
- $\chi_{hm}$
- $\frac{E_T}{p_T}$
- Distance of closest approach (DCA) with respect to the primary vertex
- Probability  $\chi_{spatial}^2$  of a spatial match between the track and the EM shower
- The number of tracks in a cone of  $\Delta R = 0.5$  around the candidate track.

Distributions for the likelihood variables are shown in Fig. 4.1. For the analysis that is presented here the identification of electrons follows from the initial EM cluster reconstruction and also requires that:

- The electron has  $p_T > 15$  GeV.
- The electron is inside the central calorimeter  $|\eta| < 1.1$
- $f_{EM} > 0.9$

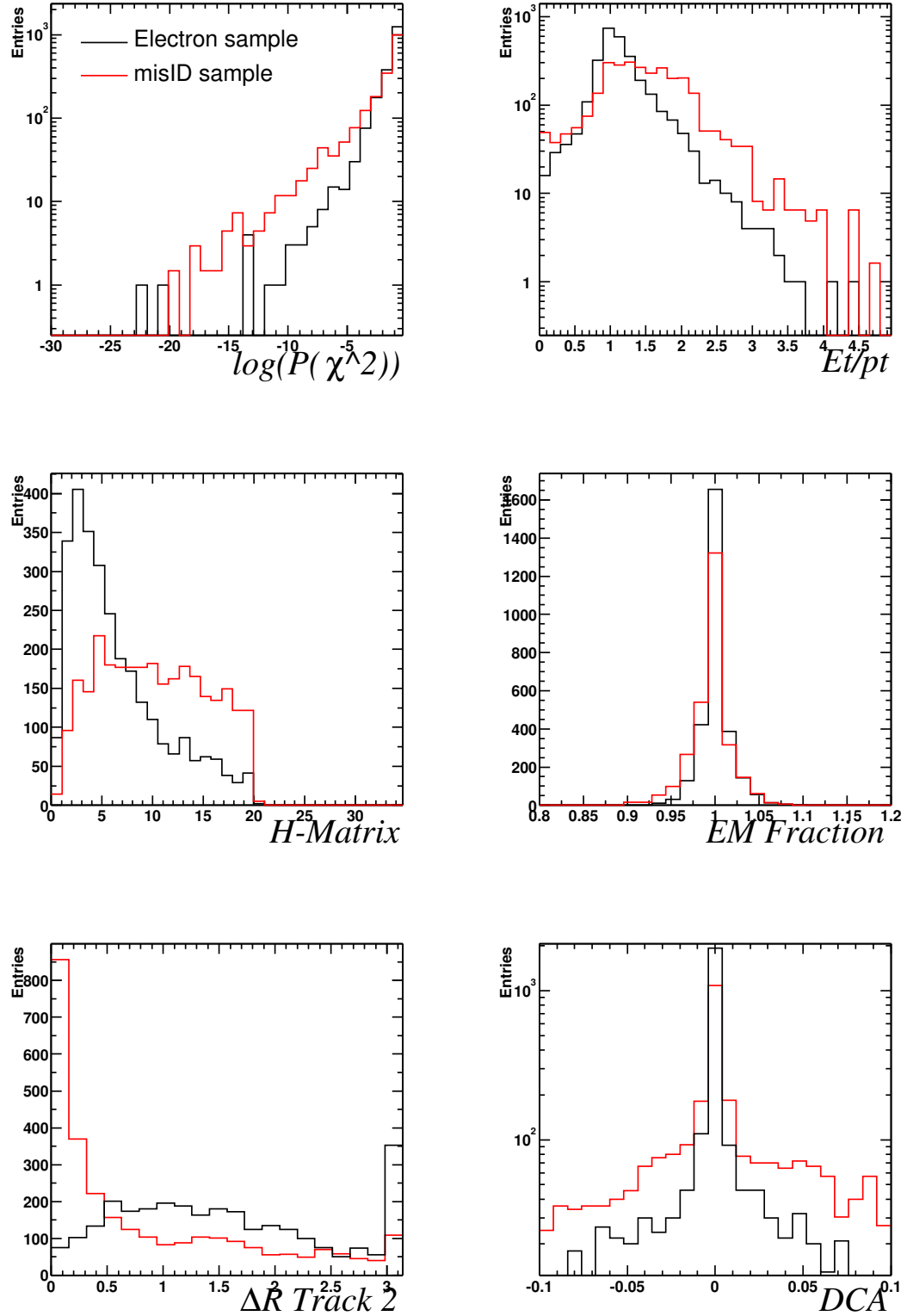


Figure 4.1: Inputs to the electron likelihood [65].

- $f_{iso} < 0.15$
- $\chi_{hm}^2 < 50$
- The electron has a track match from the central tracker with a  $\chi^2$  probability greater than 1%.
- The electron has a large likelihood value:  $L > 0.75$ .

The efficiencies for these selections are summarized in Table 4.1 [67]. Note that the efficiencies listed are evaluated after the previous entry in the table has been required. The efficiencies are evaluated using  $Z \rightarrow e^+e^-$  events in data and Monte Carlo. These events are identified by requiring one well identified electron (the tag electron) which fulfills all the above requirements along with a track pointing to an electron candidate on the other side (the probe electron). The tag electron is required to have  $p_T > 20$  GeV. The probe track is extrapolated to the front of the calorimeter and matched with an electromagnetic cluster requiring that the cluster have  $p_T > 25$  GeV and be matched in  $\phi$  with  $\Delta\phi < 0.15$ . In order to further ensure that the two candidates are indeed an electron-positron pair from a Z boson, the invariant mass of the pair is required to be within the window of 80-100 GeV. The efficiencies are then calculated with respect to the probe electron. The efficiency of the electron likelihood as a function of the mis-identification rate is shown in Fig. 4.2.

Requirement	Efficiency
Electromagnetic cluster reconstruction	$(96.0 \pm 0.4)\%$
$f_{iso} < 0.15$ and $f_{EM} > 0.9$	$(99.7 \pm 0.1)\%$
$\chi_{hm}^2 < 35$	100.0%
Track Match	$(91.3 \pm 0.5)\%$
Electron Likelihood	$(89.1 \pm 0.7)\%$

Table 4.1: Electron Requirement Efficiencies



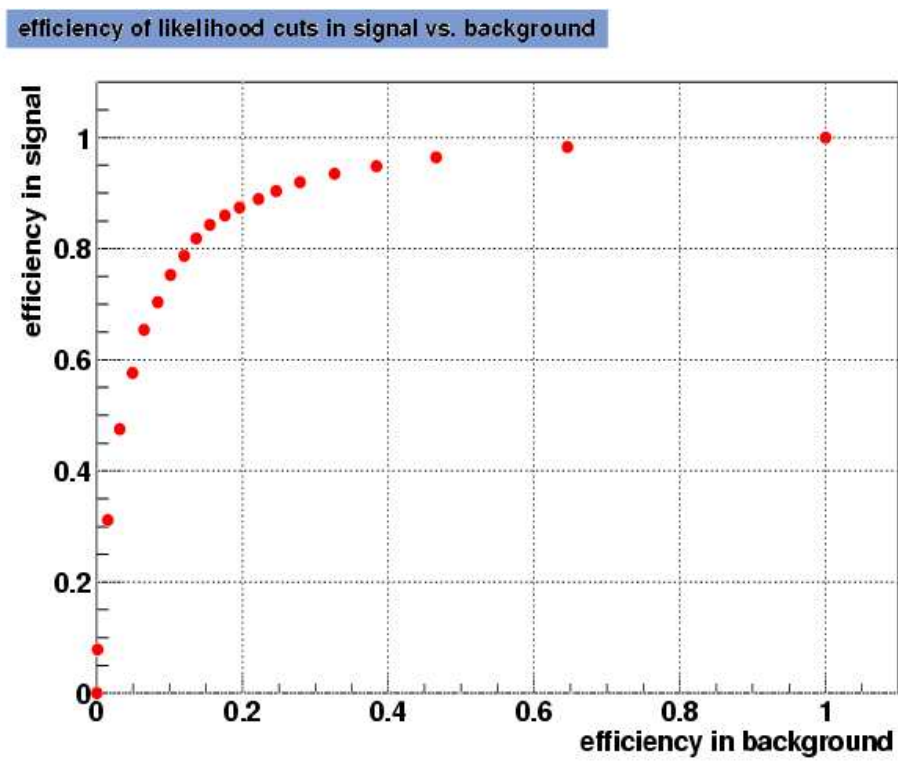


Figure 4.2: Electron Likelihood efficiency as a function of mis-identification rate [65].

### 4.5.2 Muon Identification

Muons can be identified in the DØ detector using three independent sub-detectors: the muon detector system, the central tracking system, and the calorimeter [68]. The muon detector system provides the most unambiguous way of identifying muons covering about 90% of the angular acceptance up to psuedo-rapidity  $|\eta| < 2$ . The loss in acceptance is mostly due to the presence of an electronics platform which sits under the DØ detector (see chapter 3). The central tracking system is highly efficient in finding tracks from charged particles in the entire region of the muon detector and because there are more layers the central tracker provides a more accurate measurement of the momentum of the track. Finally, since muons are minimum ionizing particles in the calorimeter they also deposit a small amount of energy in the calorimeter (though the typical efficiency of  $\approx 50\%$  is far less efficient than other muon signatures).

Muons are required to have:

- at least two A layer wire hits.
- at least one A layer scintillator hit.
- at least two BC layer wire hits.
- at least one BC scintillator hit.
- the time from the beam crossing to the scintillator hit is within 10 ns for the A layer and 15 ns for the BC layers.
- $\frac{\chi^2_{track}}{D.O.F.} < 4$  for the central track fit.
- $\Delta z(\mu, PV) < 1cm$  between the muon track and the primary vertex.
- the distance of closest approach of the track is less then 3 standard deviations from zero.

- the muon is isolated geometrically from any jet:  $\Delta R(\mu, jet) > 0.5$ .

The requirement on the scintillator hit timing is to further ensure that the muon is consistent with originating from the hard scattering event <sup>a</sup>. The requirement on the distance to the primary vertex serves two purposes. First it reduces the number of cosmic ray muons which coincidentally pass through the detector. Secondly, it removes background from poorly reconstructed tracks. The requirements on the distance of closest approach and separation from jets rejects muons that could be produced from the semi-leptonic decay of a B hadron.

## 4.6 Jet Identification

### 4.6.1 Jet Reconstruction

Before jets are constructed, the T42 algorithm [69] is run to reduce the noise in the calorimeter. The idea behind the T42 algorithm is to remove isolated energy cells from the reconstruction. Each cell in the calorimeter is examined, if the energy in the cell is below  $2.5 \sigma$  (the RMS of the energy of the pedestal) the cell is considered for removal. The algorithm then looks at all the nearest neighboring cells. If any of the neighboring cells has an energy deposition that is greater than  $4.0 \sigma$  then the cell is kept, otherwise it is rejected. This leads to removal of cells that have isolated deposition of energy which are most likely due to noise rather than the presence of a physics object.

Jets are reconstructed at DØ using the *improved legacy cone algorithm* [70] [71]. As described in section 4.2 the energy of cells in a projective tower in  $\eta$  and  $\phi$  are

---

<sup>a</sup>Muons created in the upper atmosphere (cosmic ray muons) penetrate the DØ detector and are reconstructed by the muon system. They can be removed by requiring that the muon is consistent with coming from the primary vertex both spatially and temporally.

summed. There are three steps in reconstructing jets: pre-clustering, clustering, and merging and splitting.

The pre-clustering begins by making a  $p_T$  ordered list of all the towers with  $p_T > 500 \text{ MeV}$ . This list is the starting point for the initial jet cones. Next the energy of the towers within a cone of  $\Delta R = 0.3$  is added to the four-vector of the seed tower. If the  $p_T$  of this pre-cluster is larger than 1 GeV, the pre-cluster is promoted to a cluster. If the distance in  $\eta, \phi$  space between the initial seed and the pre-cluster is small enough it is considered a 'stable protojet'. If not, the pre-cluster is used as a seed and the energy of the towers within  $\Delta R = 0.3$  are added to the four-vector to form a new pre-cluster. This process continues until the direction of the pre-cluster and the seed align. The pre-clusters are then compared for uniqueness. If two pre-clusters are within  $10^{-6}$  of each other in  $\eta, \phi$  space then they are considered the same protojet.

Once there is a list of protojets, the algorithm then looks at all the pairs of protojets that are within  $\Delta R$  of 1.0 of each other. An attempt at combining the protojets is made, by adding the two four-vectors and taking that as a seed. The clustering described in the paragraph above is repeated with these new seeds and if a new stable protojet can be made the two are merged. If not, they remain separate. The term protojet rather than jet is used, because two or more protojets can overlap. In order to form unique non-overlapping jets, further merging and splitting occurs.

The merging and splitting of the protojets proceeds very simply and considers only one parameter: the fraction of energy shared between two protojets. The list of protojets is examined starting with the one with the highest  $p_T$ . If the protojet does not share any towers with any other protojet, then it gets promoted to a jet. If it does share a tower and the fraction of shared energy constitutes less than 50% of the smaller  $p_T$  protojet then the energy in the tower is split between the two protojets

and the two return to the list of protojets. If it is larger than 50% then the jets are merged into one protojet. In either case, because of the split or merge, the two protojets no longer represent stable cones and the clustering is redone with the new objects. This process continues until there is a unique list of stable jets which do not overlap.

### 4.6.2 Jet Selection

After reconstruction the following requirements are placed on jets:

- Since jets are expected to deposit some energy in the electromagnetic calorimeter and some in the hadronic calorimeter the jets are required to have an electromagnetic fraction (EMF) of  $0.05 < EMF < 0.95$ .
- To remove jets which are reconstructed due to the noisier coarse hadronic calorimeter (CHC) jets are required to have less than 40% of their energy deposited in the (CHC).
- To remove jets which arise from one isolated cell (most likely due to electronic noise) the ratio of the  $E_T$  in the most energetic cell to the next most energetic cell is required to be less than 10.
- Because of the structure of the readout electronics, an entire calorimeter tower can have coherent noise. In order to remove jets that are reconstructed due to this effect, jets that have 90% of their energy in one calorimeter tower are removed.
- The minimum jet  $P_T$  is 15 GeV. Jets with less transverse momentum are disregarded.

- L1 confirmation of all jets.

The last item requires a bit of explanation. After the previous requirements and the use of T42 to reduce noise in the calorimeter, it was still found that an unacceptable number of jets were being formed by clustering noise in the calorimeter. If the scalar sum of the transverse momentum inside a jet in the L1 trigger towers is L1SET, the following quantity was considered:

$$\frac{L1SET}{Jet\ p_T \times (1 - CHF)} \quad (4.12)$$

In the central and end cap requirements this quantity is required to be  $> 0.4$  and in the ICR region  $> 0.2$ .

### 4.6.3 Jet Energy Scale

As mentioned previously, quarks from the hard scattering event hadronize and form hadronic jets of particles. The reconstruction of jets was discussed in the previous section. Because of the use of a sampling calorimeter, non-linearities, dead-material, showering out of the jet cone, and noise, the energy reconstructed in the calorimeter jet cones is almost always less than the energy of the particles which interacted with the calorimeter. In order to compensate for these effects the energy of the jets needs to be corrected. The corrected energy of a jet can be written [72]:

$$E_{corrected} = \frac{E_{measured} - O}{R \times S} \quad (4.13)$$

where the offset (O) is present because of energy from the underlying event, multiple interactions, electronic noise, and uranium noise from the uranium absorber. R is the calorimeter response to a jet and S is the energy fraction of a jet which lies

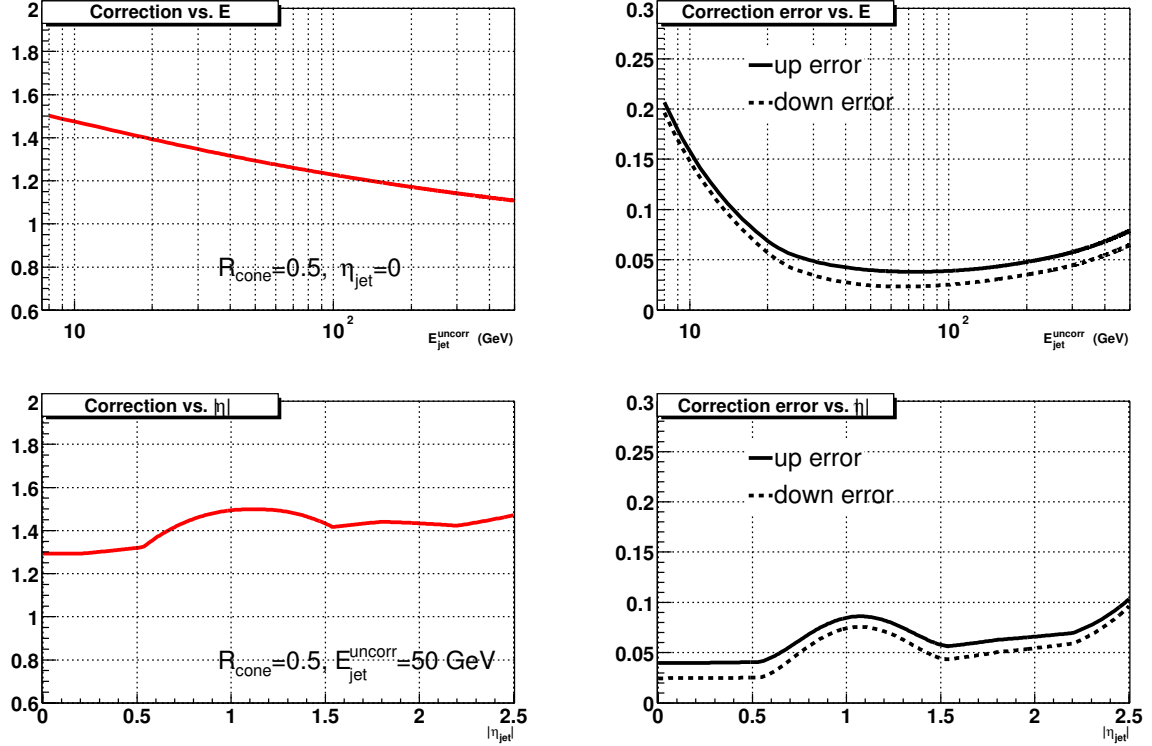


Figure 4.3: Jet energy Corrections.

inside the cone of  $R = 0.5$ . The offset is determined for events which triggered only the 'minimum-bias' event trigger (events which pass no other trigger except to have a hard event). The response term is determined by examining photon + jet events where the photon and jet are 'back-to-back' in  $\phi$ . Since the energy scale for electromagnetic objects is known with much higher precision photon + jet events are very useful. The  $p_T$  imbalance from the electron and the jet is used to derive the response term by discovering the correction which balances the transverse momentum. The showering term is determined by examining the profile of the energy deposition by jets. Figure 4.3 shows the jet energy scale correction as a function of jet energy and jet  $\eta_{\text{detector}}$ .

#### 4.6.4 Jet Energy Resolution

For jets with large transverse momentum,  $p_T > 50$  GeV, the jet energy resolution is measured using dijet events [72]. The average jet  $p_T$  is calculated:

$$\langle p_T \rangle = \frac{p_{T1} + p_{T2}}{2} \quad (4.14)$$

where  $p_{T1}$  and  $p_{T2}$  are the transverse momenta of the two jets. The events are then binned in  $\langle p_T \rangle$  and the distribution of the transverse momentum asymmetry is constructed:

$$A = \frac{|p_{T1} - p_{T2}|}{p_{T1} + p_{T2}} \quad (4.15)$$

If the jet energy measurement were perfect, there would be no asymmetry. The resolution of the jet  $p_T$  can be related to the width of the distribution of the asymmetry  $\sigma_A$  by:

$$\frac{\sigma p_T}{p_T} = \sqrt{2} \sigma_A \quad (4.16)$$

Because the trigger threshold for dijet events is placed quite high, at 25 GeV for each jet, the trigger does not become fully efficient until 50 GeV. In order to derive the resolution for jets lower than this, photon + jet events are utilized. Here an asymmetry variable can be written as:

$$A_{pj} = \frac{p_T^{jet} - p_T^\gamma}{p_T^\gamma} \quad (4.17)$$

Because the resolution on the measurement of the transverse momentum of the photon is much greater than that of the jet, it can safely be ignored and the jet energy resolution can be written as:



$$\frac{\sigma_{p_T^{jet}}}{p_T^{jet}} = \sigma_{A_{pj}} \times R_{pj} \quad (4.18)$$

where  $R_{pj} = \frac{p_T^\gamma}{p_T^{jet}}$  is the factor needed to correct the imbalance between the transverse momentum of the photon and the jet.

The jet energy resolution can be written as:

$$\frac{\sigma_{p_T}}{p_T} = \sqrt{\frac{N^2}{p_T^2} + \frac{S^2}{p_T} + C^2} \quad (4.19)$$

The jet energy resolution as a function of calorimeter region and jet  $p_T$  is summarized in Table 4.2

$\eta_{det}$ range	N	S	C
$0.0 <  \eta_{det}  < 0.5$	5.05	0.753	0.0893
$0.5 <  \eta_{det}  < 1.0$	0.0	1.20	0.0870
$1.0 <  \eta_{det}  < 1.5$	2.24	0.924	0.135
$1.0 <  \eta_{det}  < 2.0$	6.42	0.0	0.0974

Table 4.2: Jet Energy Resolution.

## 4.7 Missing Transverse Momentum

The presence of a neutrino in the final state can only be detected via the imbalance of momentum in the plane transverse to the beam. It is reconstructed from the vectorial sum of all the calorimeter cells which survive the T42 filtering. Since the coarse hadronic calorimeter has significantly more noise, it is found that only using the cells in the coarse hadronic calorimeter which are part of a jet improves the missing transverse momentum resolution. After the energy scale for the jets has been applied, the missing transverse momentum is recomputed by doing a vectorial subtraction of the jets before the jet energy scale and adding the jets after the jet

energy scale. Finally, as muons leave a small amount of energy in the calorimeter, the energy that is expected to be left in the calorimeter as a function of muon momentum,  $\eta$ , and  $\phi$  is determined from Monte Carlo and subtracted from the missing transverse momentum.

## 4.8 Secondary Vertices

Events with top quark production have two b-quarks in the final state. Identification of events with b-quarks in the final state can lead to a reduction in the background due to the absence of these particles in the largest backgrounds to this final state. Due to the relatively long lifetime of the b-quark, approximately  $1.6 \text{ ps}$ , b-quarks with a  $p_T$  in the range of 40 GeV (typical from top decays) have an average decay length of about  $3 \text{ mm}$ . Hence, b-quarks that are produced during the hard scattering process will hadronize and form b-hadrons which travel a short distance from the primary interaction point and decay. One method of identifying the presence of b-quarks in an event is to explicitly reconstruct the 'secondary' vertex using the charged particle tracks from the decay product of the b-quark. This vertex will be separated in space from the primary interaction point. If this secondary vertex can be associated with the presence of a jet in the calorimeter, one can identify the presence of jets coming from the hadronization of b-quarks. Such jets are referred to as b-jets.

The secondary vertex algorithm used here [73] [74], consists of three main steps:

- Identification and reconstruction of the primary vertex.
- Reconstruction of track-based jets.
- Secondary vertex reconstruction.

After the identification of the primary vertex, discussed in section 4.4, track-jets are reconstructed using the following procedure. First, tracks are clustered according to their distance of closest approach in  $z$ . Starting with the highest  $p_T$  track and iterating, the tracks are added to a pre-cluster if the distance in  $z$  is less than  $2\text{ cm}$  from the pre-cluster. If the track is added, the  $z$  position of the cluster is updated with the new track included. For each pre-cluster, the tracks which satisfy the requirements of having  $p_T > 1.0\text{ GeV}$ ,  $\geq 2$  SMT clusters,  $|dca| < 0.20\text{ cm}$  (in the transverse plane) and  $|dca| < 0.40\text{ cm}$  (in  $z$ ) with respect to the primary vertex are included. The selected tracks are then used to form track based jets using the algorithm described in section 4.6.1 using tracks rather than calorimeter towers.

Secondary vertices are then constructed from the track-jets. Again this proceeds through several steps:

- Track Selection: only the tracks that already part of track jets and hence pass the requirements in the above paragraph are used in addition to the requirement that  $\frac{|dca|}{\sigma_{dca}} > 3.0$ .
- Find all the two track vertices from the selected tracks.
- Attach additional tracks to the vertex according to the resulting  $\chi^2$ .
- Select the secondary vertices by selection of the parameters of the resulting vertex.

Table 4.3 indicates the requirements of the tracks and the resulting secondary vertex. Then the secondary vertices are matched in  $\eta, \phi$  space with calorimeter jets with a  $\Delta R < 0.5$  requirement. A jet is identified as a b-jet if the decay length significance is greater than 7.0.

Variable	Requirement
impact parameter significance	$\geq 3.5$
track $\chi^2$	$< 3$
$p_T$ of track	1.0 GeV
Number of SMT clusters	$\geq 2$
$r - \phi$ dca of tracks	$\geq 0.15$
z dca of tracks	$\geq 0.4$
$\chi^2$ cut for attaching tracks to vertex	15
vertex $\chi^2$	$< 100$
vertex collinearity	$\geq 0.9$
vertex decay length	$\leq 2.6cm$
minimum track multiplicity	$\geq 2$
decay length significance	$\geq 7.0$

Table 4.3: Requirements on the Construction and Selection of Secondary Vertices.

# Chapter 5

## EVENT SIMULATION

*'Everything should be made as simple as possible, but not simpler.'* Albert Einstein

### 5.1 Introduction

Because the event sample only consists of a handful of events, it is necessary to rely on computer simulations of both signal and background events to model the response of the detector. These simulations proceed through a number of steps each using Monte Carlo techniques. First, an 'event generator' is used to generate simulated events which describes the production mechanism at the hard scattering level. These programs numerically calculate the matrix elements for the production mechanism to some order in perturbation theory. Since the hadronization process cannot be described properly by perturbation theory, another program is used which relies on phenomenological models of the hadronization. This describes the process by which a quark or gluon from the hard scattering event develops into a shower of hadronic particles forming a jet. The next steps involve modeling the response of the detector to the particles in the final state of the event and describing the digitization of the

detector signals. Finally, the same event reconstruction described in the previous chapter is run on the simulated detector signals.

The **ALPGEN** program [22] is used to describe the hard scattering process for both signal and background. The **PYTHIA** program [75] was interfaced with **ALPGEN** in order to perform the hadronization process. The output is then processed through the **DØGEANT** simulation [79] [80] [81] which performs the detector simulation. With collider data the data gets digitized and read out onto digital computers. It is essential to also simulate the process by which the raw detector output gets converted to ADC values. This is done by a program called **D0SIM**.

## 5.2 Simulated Signal

The  $t\bar{t}$  simulation was performed by **ALPGEN** for  $t\bar{t}$  production and decay, while **PYTHIA** was used to generate the remaining event. The version of **ALPGEN** used, 1.2, implements the full spin correlation information. The energy scale for the calculation must be specified. Typically, this is measured by the momentum transfer of the hard scattering of the two primary partons and the momentum transfer squared is signified by  $Q^2$ . The scale for the calculation was taken to be  $Q = m_t$ .

All the leptonically decaying W boson was allowed to decay into all three leptons: electron, muon, and tau. The tau was decayed inclusively by the **TAUOLA** [76] program while **EVTGEN** [77] was used to provide the branching ratios and lifetimes of the following b quark states:  $B^0$ ,  $B^+$ ,  $B_s^0$ ,  $B_c^+$ , and  $\Lambda_b$ . The parton distribution function (PDF), which describes the probability of finding a parton  $i$  with momentum  $p_i$  inside the proton was taken to be the CTEQ6.1M [78] distribution function.

The simulation allows specification of the top quark mass. Samples were generated setting the top quark mass to 150, 160, 165, 170, 175, 180, 185, 190, and 200 GeV.

Table 5.1 shows an overview of the signal samples generated.

Top Quark Mass (GeV)	Number Generated
150	47750
160	45500
165	25750
170	48250
175	191300
180	48000
185	46500
190	48500
200	49000

Table 5.1: Overview of the  $t\bar{t}$  lepton + jets samples used in the analysis.

### 5.3 Simulated Background

The main background process is  $W + \text{jet}$  events which were again generated using ALPGEN for the matrix element and PYTHIA for the generation of the rest of the event. The following  $W + 4 \text{ jet}$  samples were generated and used in this analysis:  $Wjjjj$ ,  $Wccjj$ , and  $Wbbjj$ . The default generation parameters for the background simulation is compared to that of the  $t\bar{t}$  samples in Table 5.2. For the systematic uncertainty of the scale of the interaction a  $W + \text{jet}$  sample with  $Q^2 = \langle p_{T_j}^2 \rangle$  (the average transverse momentum of the jets in the event) was also generated. In the case of the  $W + \text{jet}$  simulation, the jets in the event come from gluon radiation. These can be quite soft, collinear, and far forward (in the direction of the initial parton). In order to have a reasonable efficiency of the generation compared to final event selection the following was required for all partons at the generation level: a minimum transverse momentum of 8 GeV,  $|\eta| < 3.0$ , and separated from all other partons in  $\eta - \phi$  space by at least 0.4. An overview of the background samples that

were used in this analysis is specified in Table 5.3.

Generation Parameters	$t\bar{t}$	W+jets
PDF	CTEQ6.1M	CTEQ5L
$Q^2$ (dynamical scale)	$m_t^2$	$M_W^2 + \sum p_{T_j}^2$
$p_t(parton)$	none	$> 8 \text{ GeV}$
$ \eta(parton) $	none	$< 3.0$
$\Delta R(parton, parton)$	none	$> 0.4$
$ \eta(l) $	none	none
$p_T(\nu)$	none	none

Table 5.2: Main Generation Parameters for  $t\bar{t}$  and W+jets simulation.

Process	Number Generated
Wjjjj	229,884
Wbbjj	417,222
Wccjj	394,500
Wjjjj ( $\sum p_{T_j}^2$ )	200,000

Table 5.3: Overview of the  $t\bar{t}$  samples used in the analysis.



# Chapter 6

## EVENT SELECTION

*'I often say that when you can measure what you are speaking about, and express it in numbers, you know something about it; but when you cannot measure it, when you cannot express it in numbers, your knowledge is of a meager and unsatisfactory kind.'*

Lord Kelvin

This chapter summarizes the selection criteria that were designed to preferentially select  $t\bar{t}$  events over background processes. Here two slightly different criterion are described. As mentioned previously, events with jets originating from a bottom quark (b-jet) are present in all top quark events while they are absent from the largest background sources. Hence, requiring evidence for one or more b-jets in an event increases the probability of selecting a top quark event. On the other hand, it is expected that the efficiency for identifying at least one b-jet in a  $t\bar{t}$  event is  $\approx 60\%$ , after all other event requirements in the selection. Because of the large mass of the top quark, events containing a top and an anti-top quark have a unique final state topology. Another strategy is to exploit this unique topology by using topological variables to select events. In this thesis, we present a measurement utilizing both

methods to select a sample highly enriched in  $t\bar{t}$  events out of the one billion events recorded.

## 6.1 Topological Analysis

The lepton + jets channel event signature (as described in section 2.6) consists of four high  $p_T$  jets, a high  $p_T$  charged lepton, and significant missing transverse energy. The two largest backgrounds are W+jet events and multijet events where a jet is misidentified as an isolated charged lepton and the transverse energy is significantly mis-measured. There are two stages of event selection: the event 'pre-selection' and the topological selection. The pre-selection is used to obtain a sample of  $t\bar{t}$  and W + multijet events and the topological selection is used to isolate the top quark events from that sample.

### 6.1.1 Muon + Jet Pre-selection

The event is required to satisfy the following requirements [82]:

- Have at least four jets with  $p_T > 20$  GeV and  $|\eta| < 2.5$ .
- The presence of a muon with  $p_T > 20$  GeV. Besides the criterion for muon identification (discussed in section 4.5.2), the muon is also required to:  $|\Delta z(\mu, PV)| < 1.0$  cm.
  - Be well separated from any jet:  $\Delta R(\mu, jet) > 0.5$  and to be isolated from energy deposition in the calorimeter [67]. This minimizes the chance that the muon originated from the decay of a hadron in a jet.
  - The central track associated with the muon must have a distance of closest

approach (dca) which is consistent with the muon coming from the primary vertex with  $\frac{dca}{\sigma_{dca}} < 3$  and  $|\Delta z(\mu, PV)| < 1.0 \text{ cm}$ .

- Have a well measured central track with a  $\chi^2 < 4$ .
- To have a large imbalance of transverse energy,  $\cancel{E}_T > 20 \text{ GeV}$ , indicating the presence of a neutrino.
- Have the missing transverse energy separated from the direction of the muon:
$$\Delta\phi(\mu, \cancel{E}_T) > 0.1 \cdot \pi - 0.1 \cdot \pi \cdot \cancel{E}_T/50(\text{GeV})$$

$$\Delta\phi(\mu, \cancel{E}_T) < 0.8 \cdot \pi + 0.2 \cdot \pi \cdot \cancel{E}_T/30(\text{GeV})$$

This is required because if the track parameters of the muon are measured poorly, the momentum can be significantly miscalculated. If this occurs, the imbalance of the transverse energy is caused by the mis-measurement and should point in the direction of the muon. The cuts were optimized by studying both data and Monte Carlo [67].

- Not have a second high  $p_T$  lepton (electron or muon).
- Have a primary vertex with at least three tracks in the fiducial region of the silicon micro-strip detector and  $|z_{PV}| < 60 \text{ cm}$ .

The efficiencies for the various event requirements are summarized in Table 6.1.

It is also required that the kinematic fit for the top quark mass converged with a  $\chi^2 < 10$  (discussed in section 6.1). There are certain aspects of the simulation which are known to slightly over-estimate the efficiencies of the various selection criteria. Essentially, these are correction factors which arise because there are effects in the data (noise, electronics readout failure, etc.) which are not completely modeled in the simulation. Correction factors for these effects have been derived [82] and the total efficiency to select a top quark event in the muon + jets channel is estimated to

Requirement	Exclusive Efficiency %	Cumulative Efficiency %
4 jets $p_T > 20$ GeV, $ \eta  < 2.5$	$46.45 \pm 0.36$	$46.45 \pm 0.36$
Muon Identification	$76.01 \pm 0.45$	$35.31 \pm 0.35$
Muon Track Match	$97.21 \pm 0.20$	$34.33 \pm 0.38$
Muon $ \eta  < 2.0$	$99.85 \pm 0.05$	$34.28 \pm 0.34$
Muon $p_{T>20}$ GeV	$71.97 \pm 0.56$	$24.67 \pm 0.31$
$\Delta R(\mu, jet) > 0.5$	$78.42 \pm 0.60$	$19.34 \pm 0.29$
Muon track $\chi^2 < 4.0$	$99.84 \pm 0.07$	$19.31 \pm 0.29$
Muon DCA significance $< 3.0$	$94.69 \pm 0.37$	$18.29 \pm 0.28$
Muon Isolation	$85.41 \pm 0.60$	$15.62 \pm 0.26$
$\cancel{E}_T \Delta\phi$	$89.19 \pm 0.54$	$13.93 \pm 0.25$
Second Muon Veto	$99.92 \pm 0.05$	$13.92 \pm 0.25$
Electron Veto	$99.89 \pm 0.06$	$13.87 \pm 0.25$
Primary Vertex Found	$99.89 \pm 0.06$	$13.87 \pm 0.25$
$ Z_{primary\ vertex}  < 60$ cm	$98.71 \pm 0.23$	$13.71 \pm 0.25$
PV with 2 tracks	$99.85 \pm 0.08$	$13.61 \pm 0.25$
$\Delta z(\mu, primary\ vertex)$	$99.92 \pm 0.05$	$13.60 \pm 0.25$
Trigger Efficiency	$95.43 \pm 0.41$	$12.97 \pm 0.24$

Table 6.1: Muon Event Selection Efficiency per Requirement [82].

be  $12.33 \pm 0.23$  %. A more comprehensive discussion on the event selection and how the efficiencies and scale factors were estimated can be found in Ref. [82].

### 6.1.2 Electron + Jet Pre-selection

The event is required to satisfy the following conditions [82]:

- Have at least four jets with  $p_T > 20$  GeV and  $|\eta| < 2.5$ .
- The presence of an electron with  $p_T > 20$  GeV. Besides the criteria for electron identification (discussed in section 4.5.1), the electron is also required to:
  - Have a match with a track with  $p_T > 10$  GeV.
  - Have an electron likelihood (section 4.5.1) value greater then 0.85.
  - Be consistent with coming from the primary vertex:  $|\Delta z(e, PV)| < 1.0$  cm.
- To have a large imbalance of transverse energy ( $\cancel{E}_T > 20$  GeV), indicating the presence of a neutrino.
- Have the  $\cancel{E}_T$  separated from the direction of the electron:
 
$$\Delta\phi(e, \cancel{E}_T) < 0.7 \cdot \pi - (0.7 \cdot \cancel{E}_T / 48.86(\text{GeV}))$$

This is required because in the case of a misidentified electron, a jet with a leading  $\pi^0$  with an accidental track match from another particle or a charged pion which charge exchanges to a neutral pion can be misidentified as an electron. In this case, the electromagnetic scale is used to correct the energy of the object. Therefore, if a jet is misidentified as an electron one expects that the momentum imbalance will point in the direction of the misidentified electron. Requiring that the  $\cancel{E}_T$  point away from the the electron in the event reduces the probability to select events with misidentified electrons.

- Not have a second high  $p_T$  lepton (electron or muon).
- Have a primary vertex with at least three tracks in the fiducial region of the silicon micro-strip detector and  $|z_{PV}| < 60 \text{ cm}$ .

Table 6.2 [82] shows the efficiency of  $t\bar{t}$  event selection for the various event requirements. After correction factors are applied to account for the data to Monte Carlo differences the efficiency of the event selection in data is estimated to be  $11.62 \pm 0.20$  % [82]. For a more detailed discussion on each of the event selection and how the efficiencies and scale factors were estimated see Ref. [82]. As in the muon + jet channel it is also required that the kinematic fit converged with a  $\chi^2 < 10$ .

Requirement	Exclusive Efficiency %	Cumulative Efficiency %
4 jets $p_T > 20 \text{ GeV}$ , $ \eta  < 2.5$	$44.43 \pm 0.29$	$44.43 \pm 0.29$
Electron Identification	$44.42 \pm 0.36$	$26.31 \pm 0.26$
Electron $ \eta_{detector}  < 1.1$	$83.31 \pm 0.43$	$21.92 \pm 0.25$
Electron Track Match	$92.94 \pm 0.32$	$20.37 \pm 0.24$
Electron $p_T > 20 \text{ GeV}$ ,	$93.2 \pm 0.4$	$19.13 \pm 0.28$
Matched Track $p_T > 10$	$99.93 \pm 0.04$	$19.11 \pm 0.23$
Electron Likelihood	$89.28 \pm 0.42$	$17.06 \pm 0.22$
$\cancel{E}_T > 20$	$89.53 \pm 0.44$	$15.28 \pm 0.21$
Second Electron Veto	$99.98 \pm 0.02$	$14.36 \pm 0.21$
Muon Veto	$99.95 \pm 0.03$	$14.35 \pm 0.21$
$ Z_{pv}  < 60 \text{ cm}$	$99.61 \pm 0.10$	$14.30 \pm 0.21$
PV with 2 tracks	$99.63 \pm 0.10$	$14.25 \pm 0.21$
$ \Delta z(e, PV)  < 1.0 \text{ cm}$	$92.63 \pm 0.74$	$14.21 \pm 0.21$
Trigger Efficiency	$92.69 \pm 0.74$	$13.17 \pm 0.22$

Table 6.2: Electron Event Selection Efficiency per requirement [82].

## 6.2 Topological Likelihood

Since the top is such a heavy object, variables such as the scalar sum of the jet  $p_T$  can give quite good discrimination between  $t\bar{t}$  and background. By making a

selection on that aspect of the event topology, it was seen that the resulting events had reconstructed top masses that were highly biased. As well the shape of the irreducible background was indistinguishable from the signal making it difficult to separate the two and remove the bias. The approach that was then taken makes use of topological variables describing the shape of the event to form a discriminant between signal and background [25] [83] with a judicious choice of variables to avoid the introduction of a bias in the top quark mass measurement.

### 6.2.1 Variables

The four topological variables considered here are:

1.  $\cancel{E}_T$ .
2.  $\mathcal{A} \equiv \frac{3}{2} \times \text{smallest eigenvalue of } \mathcal{P}$
3.  $H'_{T2} \equiv \frac{H_{T2}}{H_{\parallel}}$
4.  $K'_{Tmin} \equiv \frac{(\min \text{ of } 6 \Delta R_{ij}) \cdot E_T^{\text{lesser } j}}{E_W^T}$

$\mathcal{A}$  is the aplanarity of the event.  $\mathcal{P}$  is the normalized momentum tensor of the event derived from the momenta of the jets and the reconstructed W. It is defined as:

$$\mathcal{P}_{ij} \equiv \frac{\sum_a p_{a,i} p_{a,j}}{\sum_a |\vec{p}_a|^2} \quad (6.1)$$

where  $i$  and  $j$  label the spatial components of the momentum vector, and  $a$  runs over all jets and the reconstructed W.  $\mathcal{A}$  is defined as three-halves the smallest eigenvalue of  $\mathcal{P}$  and has a range of 0 - 0.5. It can be shown [84] that events with highly aplanar momentum vectors have large values of aplanarity.

$H_{\parallel}$  is the scalar sum of  $|p_z|$  of the jets, isolated lepton, and the neutrino.  $H_{T2}$  is the sum of the  $|p_T|$  of the jets excluding the leading jet.  $H'_{T2}$  gives rather good discrimination while having only a small correlation with the fit mass. Although variables such as  $H_T$  have notably better discrimination power, the correlation with the top quark mass and jet energy scale is unacceptably large [83].

$K'_{Tmin}$  is a measure of the jet separation folded together with “transverse energy” of the reconstructed W.  $\Delta R_{ij}$  is the distance between jet  $i$  and jet  $j$  in  $\eta - \phi$  space. Of the six possible  $\Delta R_{ij}$  between the four leading jets, the smallest is chosen.  $E_T^{lesserj}$  is the smaller of the two jets  $E_T$ ’s. Note that the transverse energy of the W is defined as the sum of  $|p_T^l|$  and  $|p_T^\nu|$ .

Two other variables were seriously considered:  $\eta_{rms} = \sqrt{\langle p_T \text{ weighted } \eta^2 \rangle}$  and sphericity. Both variables were seen to give good discrimination, however both had a high correlation with the other variables used (most notably  $H'_{T2}$  and  $\mathcal{A}$ ) and hence did not contribute very much to the overall discrimination power.

### 6.2.2 Distributions

Figure 6.1 shows the distributions of the four topological variables obtained for a background sample of W+jets and  $t\bar{t}$  Monte Carlo. Since W+jet events are expected to be the largest background, the discriminant was built to provide as much discrimination between  $t\bar{t}$  events and W+jet events as possible (see section 6.5).

### 6.2.3 Correlations

There are two types of correlations which are important in constructing a low bias likelihood. A kinematic fit is applied to each of the candidate events (described in chapter 7) which returns a fit mass for each event. The distribution of the fit masses



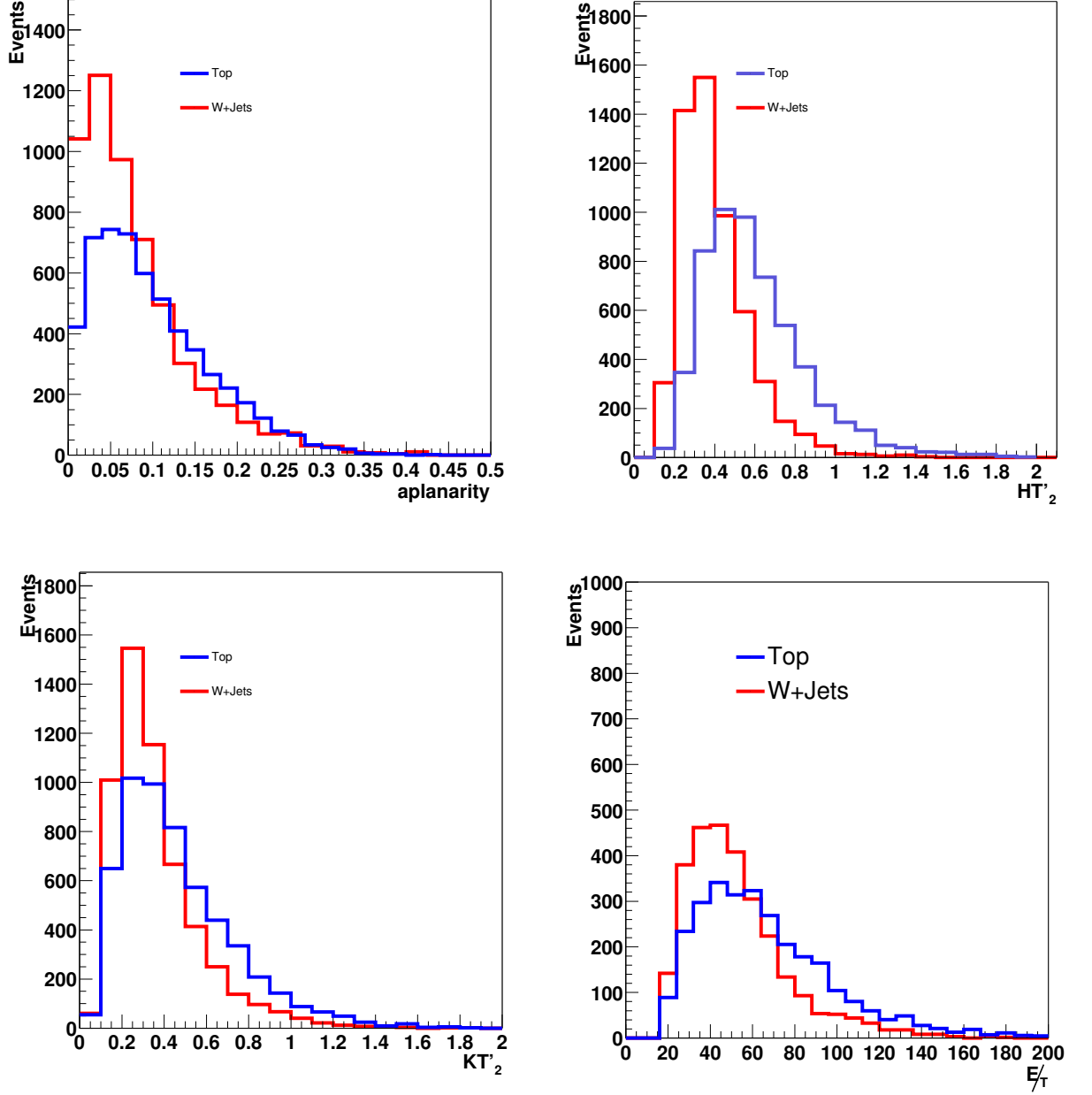


Figure 6.1:  $\mathcal{A}$  distributions (top left),  $H'_{T2}$  distributions (top right),  $K'_{Tmin}$  distributions (bottom left) and  $E_T$  distributions (bottom right) for  $t\bar{t}$  and background.

is used to extract the top mass. The first, and most important is the correlation of the variables that form the likelihood and the fit mass for the events. The purpose of constructing the low bias likelihood is to determine a way of separating the signal from background without either loosing sensitivity or biasing the measurement in an unknown way. Figure 6.2 shows the correlation of the four topological variables with the fit mass.

The correlation coefficients between the topological variables and the fit mass are summarized here (for the  $t\bar{t}$ ):

1.  $\cancel{E}_T$ : 0.06
2.  $\mathcal{A}$ : -0.09
3.  $H'_{T2}$ : 0.02
4.  $K'_{Tmin}$ : 0.03

It is important to check that the variables are not significantly correlated with each other or with the fit mass. In order to do so we compute the standard Pearson product linear moments. For the correlations amongst themselves, this is best represented by a symmetric matrix. The elements are calculated according to:

$$C_{ij} = \frac{\langle (L_i - \bar{L}_i)(L_j - \bar{L}_j) \rangle}{\sigma_i \sigma_j} \quad (6.2)$$

if  $i = (1, 2, 3, 4) = (\cancel{E}_T, \mathcal{A}, H'_{T2}, K'_{Tmin})$ ; we obtain:

$$\mathcal{C} = \begin{pmatrix} 1 & -0.05 & 0.03 & -0.04 \\ -0.05 & 1 & 0.37 & 0.12 \\ 0.03 & 0.37 & 1 & 0.17 \\ -0.04 & 0.12 & 0.17 & 1 \end{pmatrix} \quad (6.3)$$

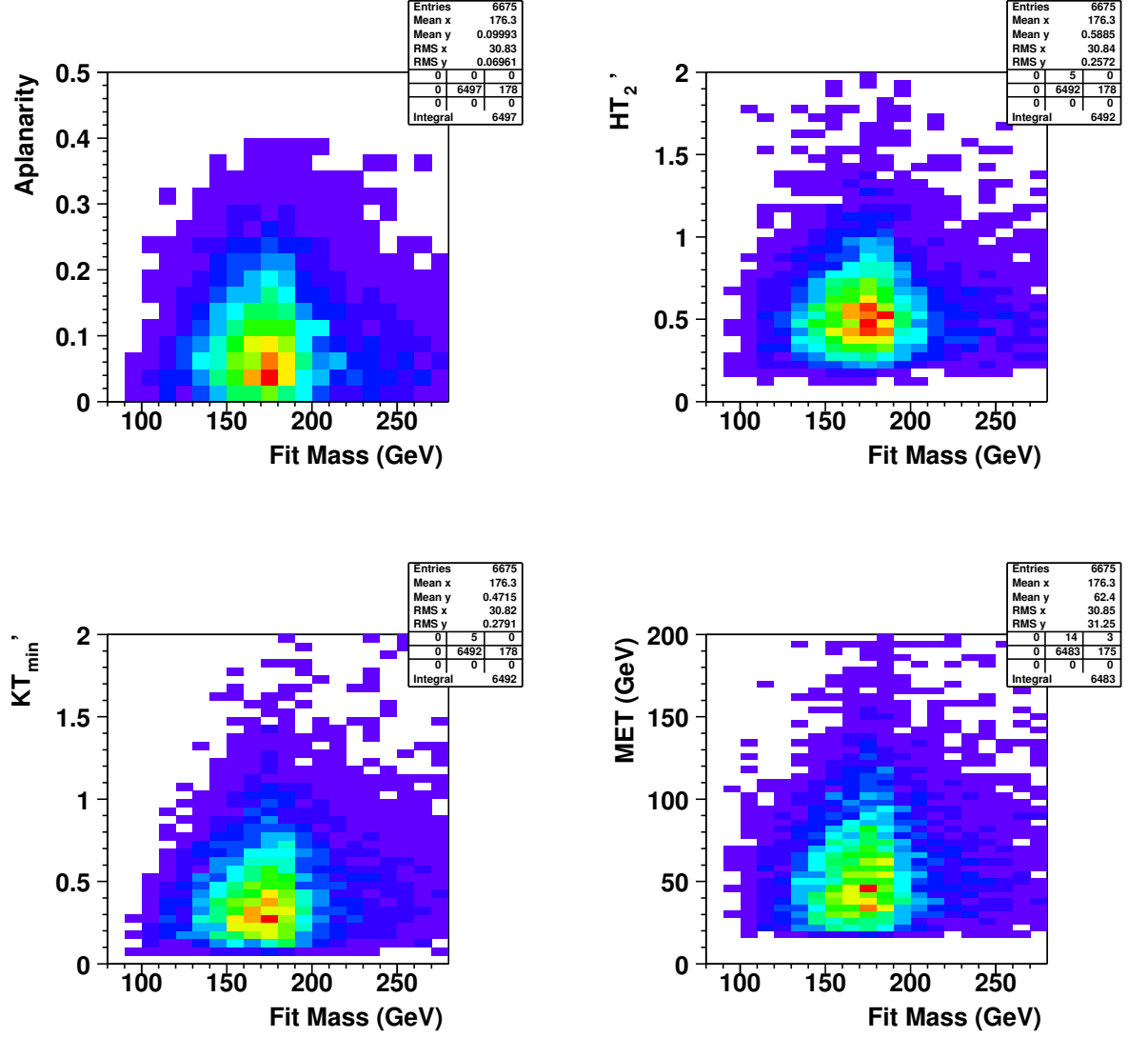


Figure 6.2:  $\mathcal{A}$  versus  $m_t$  (top left),  $H'_{T2}$  versus  $m_t$  (top right),  $K'_{Tmin}$  versus  $m_t$  (bottom left) and  $\cancel{E}_T$  versus  $m_t$  (bottom right) for  $t\bar{t}$

The variables with the most significant correlation are  $\mathcal{A}$  and  $H'_{T2}$ . The correlations between the various variables are displayed in Fig. 6.3.

#### 6.2.4 Forming the Discriminant

Now we must develop a procedure to obtain maximal discrimination between signal and background by combining these variables into a likelihood. We follow the work described in Ref. [83]. For each event we compute a discriminant which is mapped between 0 and 1 from the topological variables. The closer the value is to one, the more likely it is that the event is a  $t\bar{t}$  event. This procedure is described below.

First, the topological variables are not used directly. A set of functions is used to map the variables such that the distributions are more smoothly varying. The motivation for this step is that when performing fits to the topological variables the fits are highly effected by the large variations. In particular, statistical fluctuations in rapidly varying regions can cause bad fits and poor understanding of the data. The functions that are used ( again following Ref. [83] ):

1.  $\mathcal{A}$ :  $e^{-11\mathcal{A}}$
2.  $H'_{T2}$ :  $\ln H'_{T2}$
3.  $K'_{Tmin}$ :  $\sqrt{K'_{Tmin}}$
4.  $\cancel{E}_T$ :  $e^{-\max\left(0, \sqrt{\frac{3(\cancel{E}_T-5)}{2}}\right)}$

From this set of functions, we form the bin by bin ratio for variable  $i$  :

$$L_i^{tb} = \ln\left(\frac{top}{background}\right) \quad (6.4)$$

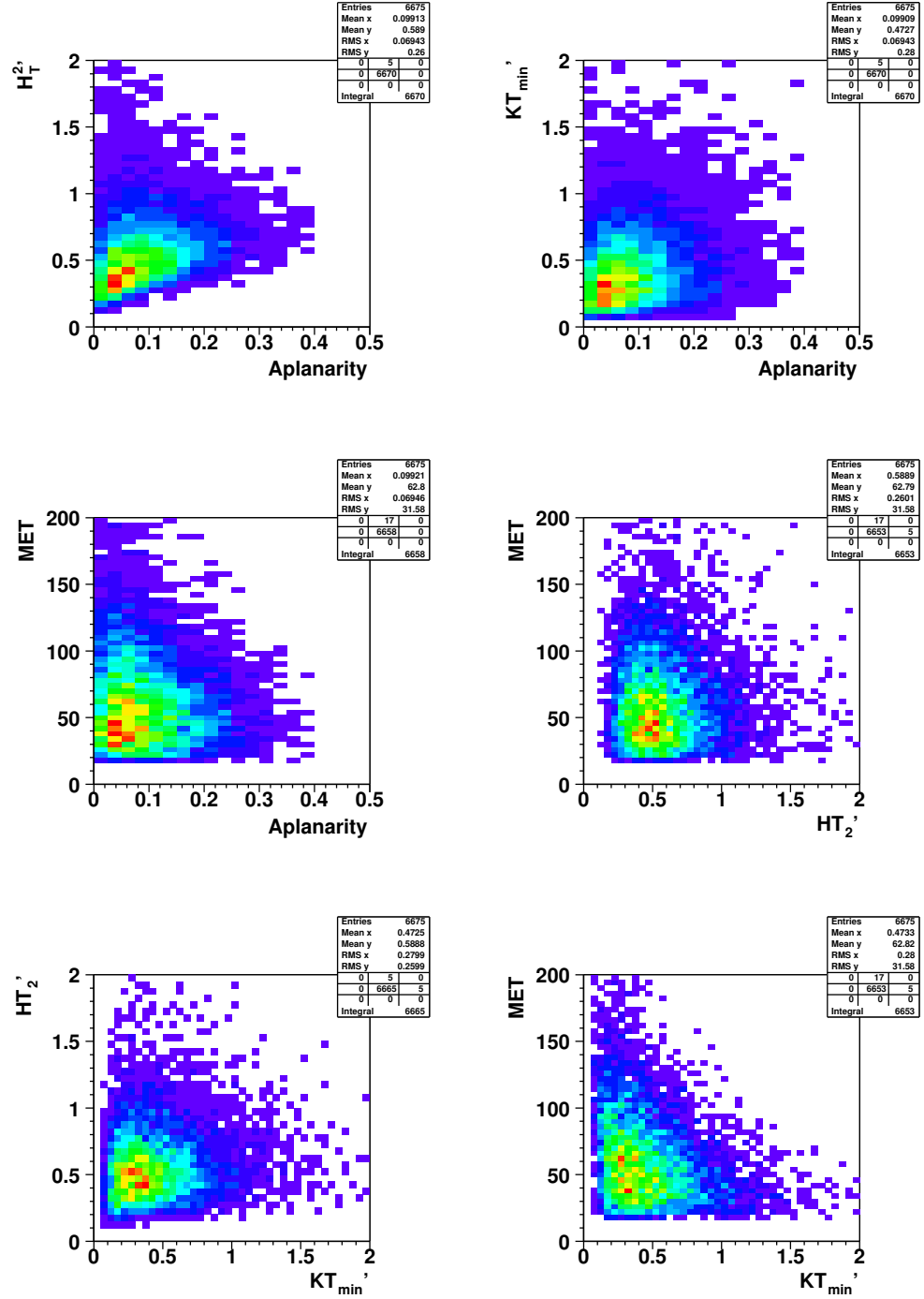


Figure 6.3:  $\mathcal{A}$  versus  $H_{T2}'$  (top left),  $\mathcal{A}$  versus  $K_{Tmin}'$  (top right),  $\mathcal{A}$  versus  $\cancel{E}_T$  (middle left),  $H_{T2}'$  versus  $\cancel{E}_T$  (middle right),  $K_{Tmin}'$  versus  $H_{T2}'$  (lower left), and  $K_{Tmin}'$  versus  $\cancel{E}_T$  (lower right) for  $t\bar{t}$ .

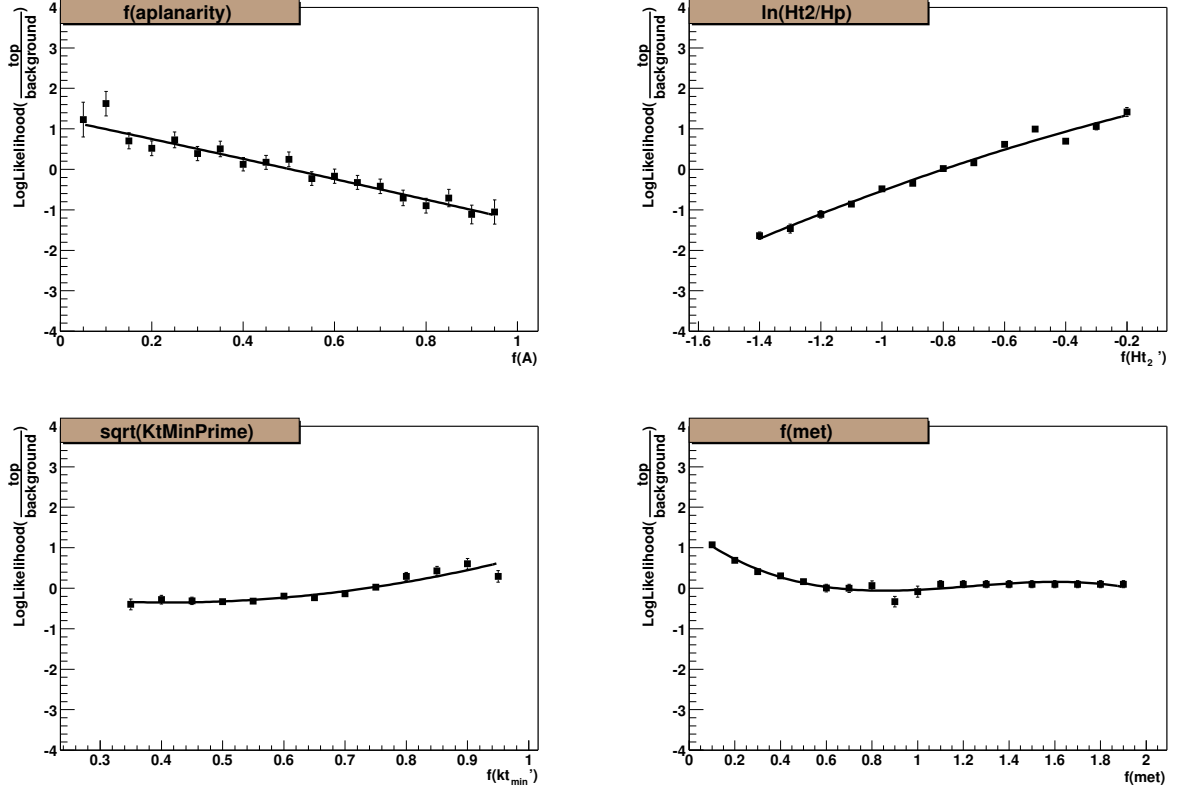


Figure 6.4:  $\mathcal{A}$  fit (top left),  $H'_{T2}$  fit (top right),  $K'_{Tmin}$  fit (bottom left) and  $\cancel{E}_T$  fit (bottom right)

The next step is to fit polynomial functions to each of the points generated above. One should also note that underflows and overflows are placed in the edge bins of the histogram. This is to ensure that there is minimal loss of information in this procedure. The fits are shown in Fig. 6.4

From these functions a combined log likelihood is found by summing the individual log likelihoods:

$$L^{tb} = \sum_{i=1}^4 L_i^{tb}(f_i) \quad (6.5)$$

Finally, the likelihood discriminant is formed as:

$$\mathcal{D}_{LB} = \frac{1}{1 + \mathcal{P}e^{-L^{tb}}} \quad (6.6)$$

We choose  $\mathcal{P}$  to be 1.25. Clearly the choice of this variable is independent of the discrimination achieved. We choose this value to be consistent with Ref. [83].

To evaluate the discriminant, we compute the individual likelihoods for each variable by using the fit function on an event by event basis. For each event we then use Eq. 5.6 to form the final discriminant. The distribution from the topological likelihood for signal and background are shown in Fig. 6.2.4. The improvement that is achieved in separating the signal and background with the combination of the four variables is quite dramatic. To see this, consider a comparison with making individual requirements of the variables. The following requirements on each of the topological values (individually) retain 95 % of the  $t\bar{t}$  events (after the event preselection which requires the  $\cancel{E}_T > 20$  GeV):

1.  $\mathcal{A} > 0.015$
2.  $H'_{T2} > 0.28$
3.  $K'_{Tmin} > 0.145$
4.  $\cancel{E}_T > 0.25$

With these requirements the following efficiencies are observed in the W+jet sample:

1.  $\mathcal{A}$ : 88% events retained.
2.  $H'_{T2}$ : 80% events retained.
3.  $K'_{Tmin}$ : 93% events retained.

4.  $\cancel{E}_T$ : 94% events retained.

The total efficiency for these selections for the  $t\bar{t}$  sample is 81 % while retaining 61 %. Requiring the discriminant to be larger the 0.48 retains 81% of the  $t\bar{t}$  events and 46 % of the w+jet events, which is a 16 % improvement in rejection.

Since all these correlations are below 0.1, we find these variables acceptably uncorrelated with the fit mass. In order to obtain a quantitative measure of the separation achieved we compute the signal to noise ratios,  $s_i$ , for each variable i as:

$$s_i \equiv \frac{\frac{1}{2}\langle L_i^{tb} \rangle_{top} - \frac{1}{2}\langle L_i^{tb} \rangle_{bkgnd}}{\sqrt{\frac{1}{2}\sigma^2(L_i^{tb})_{top} + \frac{1}{2}\sigma^2(L_i^{tb})_{bkgnd}}} \quad (6.7)$$

for this we find:

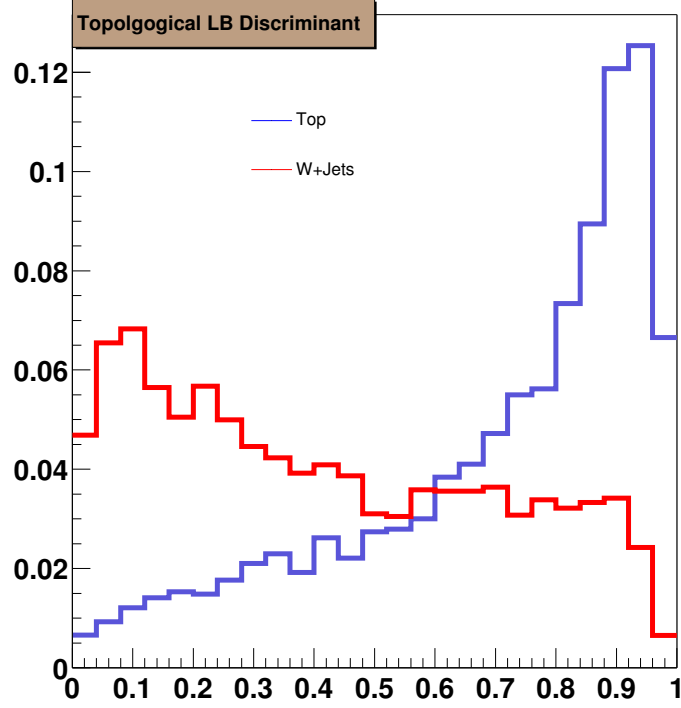
1.  $s(\cancel{E}_T) = 0.05$
2.  $s(\mathcal{A}) = 0.63$
3.  $s(H'_{T2}) = 0.32$
4.  $s(K'_{Tmin}) = 0.28$

A final requirement of a topological discriminant  $\mathcal{D}_{LB} > 0.4$  was chosen to minimize the expected statistical error on the determination of the top quark mass (see chapter 7). It is expected that this requirement retains  $\approx 85\%$  of the top quark events while rejecting  $\approx 50\%$  of the background. Table 6.3 summarizes the efficiencies of the additional requirements after the event preselection.

### 6.3 Analysis with b-jet identification

Since a  $t\bar{t}$  event will have a bottom and anti-bottom quark that will hadronize and form b-jets, while the majority of the background does not, the identification of b-



Figure 6.5: Discriminant for  $t\bar{t}$  and background.

Electron + Jets Event Requirement Efficiencies		
Source	$\chi^2 < 10$	$D_{LB} > 0.4$
$t\bar{t}$	$97.4 \pm 0.3\%$	$87.8 \pm 0.6\%$
W + jets	$87.8 \pm 1.5\%$	$56.2 \pm 2.3\%$
Multijet	$89.6 \pm 3.3\%$	$62.8 \pm 6.1\%$
Muon + Jets Event Requirement Efficiencies		
Source	$\chi^2 < 10$	$D_{LB} > 0.4$
$t\bar{t}$	$92.2 \pm 0.4\%$	$83.9 \pm 0.8\%$
W + jets	$87.5 \pm 1.4\%$	$47.3 \pm 2.5\%$
Multijet	$85.0 \pm 3.3\%$	$66.2 \pm 6.5\%$

Table 6.3: Efficiencies for requirements after event preselection. The efficiencies quoted are relative to all previous requirements.

jets can be used to preferentially select top quark events while removing background events. In this analysis, we use a similar preselection discussed in section 6.2.1 and 6.2.2 but also require the identification of one or more jets that are tagged as b-jets and lower the jet  $p_T$  requirement to 15 GeV. Since requiring one or more b-jets in the event greatly reduces the background (as will be discussed below) lowering the jet  $p_T$  requirement allows more efficient selection of  $t\bar{t}$  events. As well, the  $\chi^2$  is relaxed and all that is required is that the kinematic fit converges in a permutation consistent with the b-jet identification. The procedure for identifying secondary vertexes from the charged particle tracks and identifying them with calorimeter energy deposition was described in section 4.8.

### 6.3.1 Flavor Composition

As mentioned before, the largest backgrounds do not have heavy flavor quarks in the final state and hence requiring the presence of b-jets significantly increases the purity of the sample. Unlike the case of the topological analysis where there are only two relevant backgrounds, several other background sources become important here. While the most important backgrounds are still  $W + \text{jet}$  events and multijet events with lepton misidentification, there are other distinct sources of background become more prominent because of the requirement on the tagged jet.

For the purposes of the lifetime tagging method based on the presence of a secondary vertex, it is convenient to separate the quarks into 'light' and 'heavy flavor' depending on the lifetime of the hadrons they form. For these purposes the up, down, and strange quarks are categorized as light flavor, while the charm and bottom quarks are labeled as heavy quarks. The main purpose of this categorization is not to separate them on the basis of the mass of the quarks but rather using the lifetime of the hadrons they form. The light flavor hadrons or the hadronic jets which they

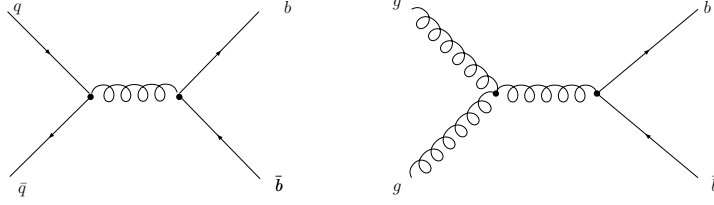


Figure 6.6: Lowest order diagrams for the flavor creation process.

comprise have a very small probability of being identified as heavy flavor. This can occur, with a probability of  $\approx 0.5\%$  (chosen by construction of the secondary vertex selection), because of mis-measured track parameters. To a good approximation the probability to mis-tag a light quark jet is independent of these three flavors [73] [74]. In contrast, the heavier charm and bottom quarks form hadrons that will travel some short distance ( $\approx$  few mm) and then decay. Since the lifetime of the charm hadrons is shorter than the b hadrons (and hence the decay length is shorter) the probability of finding a secondary vertex from the decay of a charm hadron is smaller and found to be  $\approx 15\%$  (averaged over  $p_T$  and  $\eta$ ). Whereas, the probability of finding a b-jet is  $\approx 50\%$  for the  $p_T$  and  $\eta$  range that is of interest for top quark decays.

There are three basic sources of heavy flavor jets: flavor creation, flavor excitation, and parton shower/fragmentation [85]. Flavor creation corresponds to the production of a  $b\bar{b}$  pair by either gluon fusion or the annihilation of light quarks in the process shown in Fig. 6.6.

The flavor excitation process is shown in Fig. 6.7. In this process a b or  $\bar{b}$  is scattered out of the initial state and into the final state by a quark or gluon. Although there are no 'intrinsic' or valence b quarks in the proton, the proton has a 'sea' of virtual quarks [3] [4]. These virtual quarks can be of any flavor and are governed via a structure function of the proton [3]. Finally, the heavy flavor quarks can be produced

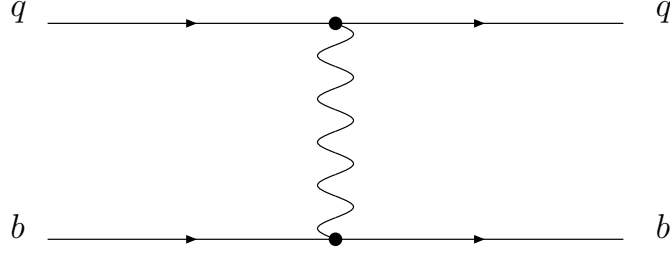


Figure 6.7: One of the lowest order diagrams for b excitation.

by gluon splitting in the parton as shown in Fig. 6.8. Note that the branching ratios have for the heavy flavors have been separated into two classes: one in which the two heavy quarks from hadronize and form separate jets and one in which the heavy quarks are not separated enough in  $\eta - \phi$  space and merge into one jet. When the two heavy quarks are merged into one jet this is denoted by the notation  $(c\bar{c})$  and  $(b\bar{b})$ .

Flavor Composition	Branching Fraction %
W + light jets	$84.1 \pm 2.3$
W( $c\bar{c}$ )	$3.3 \pm 0.43$
W( $b\bar{b}$ )	$1.87 \pm 0.74$
Wc	$5.31 \pm 0.33$
W $c\bar{c}$	$2.8 \pm 1.1$
W $b\bar{b}$	$2.56 \pm 0.17$

Table 6.4: Flavor composition in the W + Jet sample [86], [22].

These processes, in conjunction with multiple jets from initial state radiation, form the heavy flavor multijet background. As in the case of the multijet light flavor background, one jet can be misidentified as an isolated lepton and the transverse energy significantly mis-measured. Because of the relatively small probability for a jet to be misidentified, ( $\approx 10^{-4}$ ), this is again a smaller fraction of the background.

The largest background is W + jet production where one of the jets is produced

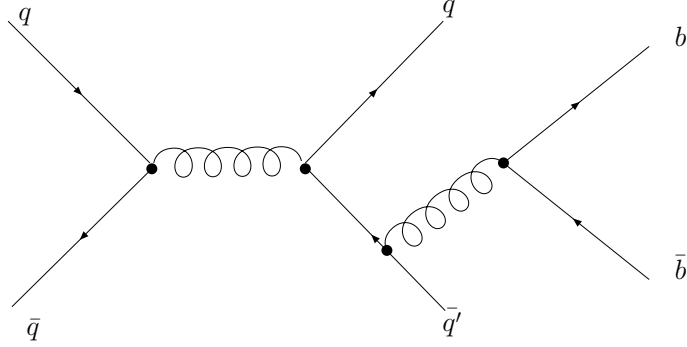


Figure 6.8: An example of gluon splitting in the fragmentation process.

from the hadronization of a heavy quark. The three sources of heavy flavor are identical to the multijet case, however, a W boson is produced in the scattering as well. A representative diagram for each of the three processes is shown in Fig. 6.9. Note that in the diagrams shown in Figs. 6.6 - 6.9 the bottom quark can be replaced with a charm quark. It is important to make a distinction between these two backgrounds in the case that one explicitly reconstructs a secondary vertex, in one of the jets and requires its presence in the event selection because of the different probabilities for the process to occur and to be identified. In the case of gluon splitting into heavy quarks some care has to be taken since the two quarks produced can often merge into one jet. If this occurs, the probability of being identified as a heavy flavor jet is higher since there will be a higher track multiplicity coming from the decay of two separate heavy flavor hadrons.

Other backgrounds have also been considered:  $Z \rightarrow \tau\tau$ , diboson production (WW, WZ, ZZ), and electroweak production of single top events. However, it was found the expected contribution of these processes to the final event selection was negligible [86].

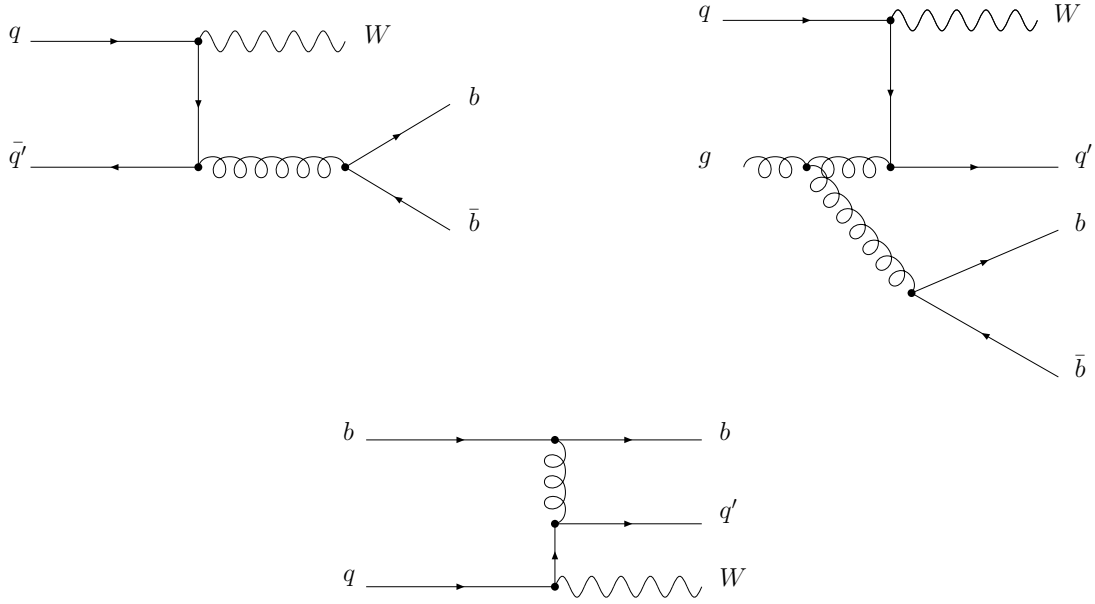


Figure 6.9: Sources of W+heavy flavor jets at the Tevatron.

### 6.3.2 Tagging Probabilities

We find that the efficiency of identifying a b-jet in Monte Carlo events and collider data is not the same. Therefore, a scale factor must be applied to the Monte Carlo in order to accurately represent the data and to give better estimates of the performance of the detector. One can write the probability to identify a b-jet as:

$$P_{jet(\alpha)}(E_T, \eta) = P_{tag(\alpha)}^{data}(E_T, \eta) SF_{tag(\alpha)}(E_T, \eta) \quad (6.8)$$

where  $\alpha$  labels the flavor of the jet and  $SF$  is the scale factor. The probability of identifying or tagging a jet varies with the transverse energy of the jet. The greater the energy of the hadron, the larger the relativistic  $\gamma$  factor and the longer the decay length. From the per jet tagging efficiencies, one can calculate the probability that an event with several jets will have at least one tag.

$$P_{event}^{tag}(n \geq 1) = 1 - \prod_{i=1}^{N_{jets}} (1 - P_{jet(\alpha)}^j(E_T, \eta)) \quad (6.9)$$

Again,  $\alpha$  labels the flavor of each jet. The probability for a single tag in a  $t\bar{t}$  event is estimated at  $45.5 \pm 0.1\%$  while the probability of a double tag is estimated to be  $15.1 \pm 0.1\%$  [86]. The tagging probabilities for the signal and most relevant background sources are shown in Table 6.5.

Process	Single Tag Probability %	Double Tag Probability %
Multijet	$7.2 \pm 2.0$	$0.68 \pm .48$
W + light jets	$1.18 \pm 0.01$	$< 0.01$
W( $c\bar{c}$ )	$6.6 \pm 1.0$	$0.04 \pm 0.01$
W( $b\bar{b}$ )	$30.0 \pm 2.3$	$1.18 \pm 0.78$
Wc	$8.7 \pm 0.1$	$0.062 \pm 0.003$
W $c\bar{c}$	$14.1 \pm 0.6$	$0.67 \pm 0.07$
W $b\bar{b}$	$42.2 \pm 0.3$	$9.8 \pm 0.3$
$t\bar{t}$	$45.5 \pm 0.1$	$15.1 \pm 0.1$

Table 6.5: Probability for signal and background events to be tagged corrected in data [86].

## 6.4 Event Yield and Sample Composition

The data set corresponds to an integrated luminosity of  $226.1 \text{ pb}^{-1}$  in the electron + jets channel and  $229.1 \text{ pb}^{-1}$  in the muon + jets channel. After the event selection (without any requirement on the topological discriminant, identification of b-jets, or  $\chi^2$  requirement), there are 87 events that pass the electron + jets selection and 80 events that pass the muon + jet selection. The cross-section is extracted via a fit to a (similar) topological likelihood. Template fits to the likelihood distribution give the sample composition shown in Table 6.7 [82]. It is convenient to refer to the set of requirements that are used in the cross-section analysis as the preselection.

Electron + Jets	
Requirement	Number of Events
Preselection	87
$\chi^2 < 10$	78
$D_{LB} > 0.4$	49
Muon + Jets	
Requirement	Number of Events
Preselection	80
$\chi^2 < 10$	68
$D_{LB} > 0.4$	45

Table 6.6: Topological Event Yield.

Channel	Predicted Number of Events
Electron + Jets	
$t\bar{t}$	$27.5 \pm 2.2$
W+jets	$9.5 \pm 0.45$
Multijet	$12 \pm 0.55$
Muon + Jets	
$t\bar{t}$	$20.4 \pm 0.9$
W+Jets	$22.0 \pm 2.6$
Multijet	$2.6 \pm 0.5$

Table 6.7: Expected Sample Composition for Topological Analysis.



After the requirement on the discriminant and the convergence of the kinematic fit the total number of events is reduced to 94. Taking into account the efficiencies for these additional selections for signal and background, approximately 51% of these events are expected to be  $t\bar{t}$  events. With the tagged event selection the number of events in data is 69 with approximately 76 % of the events expected to be from  $t\bar{t}$ . Table 6.6 summarizes the event yield in the topological selection while Table 6.8 summarizes the event yield for the tagged selection. Table 6.9 summarizes the predicted sample composition before and after the kinematic fit convergence. Note that for simplicity the heavy flavor contributions that were separated in table 6.5 have been combined depending on the flavor of the heavy quark.

Electron + Jets			
Requirement	Single Tags	Double Tags	Total
Preselection (with Jet $p_T > 15$ GeV )	38	9	47
$\chi^2$ Convergence	36	6	42
Muon + Jets	Single Tags	Double Tags	Total
Requirement			
Preselection (with Jet $p_T > 15$ GeV )	24	5	29
$\chi^2$ Convergence	22	5	27

Table 6.8: Tagged Event Yield.

Channel	Expected Number of Events
Electron + Jets	
$t\bar{t}$	$30.5 \pm 2.4$
W+jets	$7.0 \pm 0.6$
Multijet	$4.5 \pm 0.4$
Muon + Jets	
$t\bar{t}$	$22.0 \pm 1.75$
W+Jets	$4.3 \pm 0.3$
Multijet	$0.7 \pm 0.05$

Table 6.9: Expected Sample Composition for Tagged Analysis.

# Chapter 7

## METHODS FOR THE TOP QUARK MASS MEASUREMENT

*'No problem can stand the assault of sustained thinking.'*

Francis Marie Arouet de Voltaire

### 7.1 Kinematic Fitting

In order to reconstruct the mass of the top quark from its decay products, we need to measure the four-vectors of the final state particles: the jets, charged lepton, and neutrino. While the jets formed after the hadronization of the final state quarks and the charged lepton can be directly observed, and their properties measured by the DØ detector, the neutrino cannot. However, the presence of the neutrino can be inferred from the missing transverse energy in the event:  $\cancel{E}_T$ . This missing energy is taken to be the magnitude of the transverse momentum of the neutrino. However, this procedure cannot be extended to the longitudinal or z component of the neutrino momentum since there are particles with very small transverse momentum that escape

down the beam pipe. The  $p_z$  of the neutrino is the one kinematic unknown in the event.

### 7.1.1 Fit Description

There are three constraints on the four-vectors in the decay. Since the two W's are produced on shell in  $t\bar{t}$  events, two jets should have the invariant mass of the W as should the charged lepton and neutrino. Also CPT conservation demands that the mass of the top and anti-top quark are the same. However, in the actual experiment, the top and anti-top are not produced exactly on-shell in every event and the W has a finite width as well. It has been shown that making the on-shell approximation leads to less than 0.05% variation in the kinematic fit [87] (the leading uncertainties are at least 1-2 orders of magnitude larger making the approximation valid).

We have three constraints but only one unknown, hence the kinematic algebra is twice over-constrained. In order to start the fitting procedure, one must have an initial value for all of the kinematic variables. The  $p_z$  of the neutrino is found by forcing the invariant mass of the charged lepton and the neutrino to be that of the W boson. This leads to a quadratic equation and two possible solutions. This is consistent with the over-constrained nature of the problem. In principle, one could attempt to use the results of the fits from both solutions. In practice it has been found that taking the smallest absolute value of the neutrino solution yields the correct solution in approximately 60% of the cases [88]. In the same work it was also found that either solution ultimately yields the same fit mass in over 90% of the cases.

The fit is based on the SQUAW [89] algorithm and was implemented in the the `hitfit` package [88]. The fit is performed by minimizing a  $\chi^2$  defined as:

$$\chi^2 = (\vec{x} - \vec{x}_M)G(\vec{x} - \vec{x}_M)^T \quad (7.1)$$

where  $\vec{x}_M$  is a vector of measured variables,  $\vec{x}$  is a vector of fitted variables, and  $G$  is the inverse error matrix of the measured quantities.  $G$  is taken to be diagonal. The fit attempts to minimize the  $\chi^2$  subject to the three constraints.

If the fit were linear in its parameters, one could solve the minimization problem by the method of Lagrange Multipliers and standard linear algebra techniques. Since this is not the case an iterative technique is used. The starting point is the vector of measured values of the variables. Then the constraint functions are expanded in a power series and linearized. Using Lagrange Multipliers the  $\chi^2$  is minimized with respect to linearized constraint equations. The fit values for that iteration are taken as the starting point for the next iteration. In the next iteration the constraint equations are re-evaluated. This process continues until the constraint equations are satisfied or the  $\chi^2$  stops changing. If the the fit requires more than 1,000 iterations then the fit is stopped and discarded. This occurs in less than 0.1 % of Monte Carlo  $t\bar{t}$  events. For a more detailed description of the algorithm see Ref. [88].

Another fold in the procedure is jet permutations. To lowest order, there are four jets from the hadronization of the four quarks in the final state. *A priori* it is not known which jet came from which parton. Therefore, one has to attempt to fit all the possible jet assignments. With four jets there are twelve distinct permutations (in principle there are twenty-four permutations for four objects but the invariant mass of the hadronically decaying  $W$  is the same if the two jets assigned to the  $W$  are exchanged). These incorrect permutations are another source of background. Often initial and final state gluon radiation can lead to more than the nominal four jets. Only the four highest  $p_T$  jets are used in the fit. We assume that any other jet is from initial state radiation.

The number of permutations rapidly increases as the number of jets considered in the fit increases, the first few values are:

- $N_{jets} = 4$ ; 12 permutations.
- $N_{jets} = 5$ ; 140 permutations.
- $N_{jets} = 6$ ; 1020 permutations.
- $N_{jets} = 7$ ; 5992 permutations.

This fast increase is one of the motivating factors in only considering the highest four  $p_T$  jets in the fit. In each case, there is only one correct permutation and the others act as a background source which smears the resolution of the fit.

### 7.1.2 Fit Performance

In order to assess the performance of the kinematic fit, we must first examine the resolutions and the energy scale of the input quantities. The objects in the event with the worse resolution are also the most ubiquitous objects in lepton+jet events: the jets. The essential problem is that the experimental signature is the response of the calorimeter to a jet of hadronic particles. On the other hand, in order to reconstruct the mass of the top quark one would like to use conservation of energy and momentum of the primary decay particles. Since this is impossible, one attempts to make a mapping from the measured jet energies to the partonic level energies. Even in principle, an exact mapping cannot be made because while the quarks from the decay of the top quark and hadronically decaying  $W$  are colored objects, the jets are color neutral. As well, experimental constraints complicate this process since the calorimeter response does not measure the energy of the particles in the jet perfectly.

Nonetheless, by examining Monte Carlo events where one can uniquely match parton to jets in  $\Delta R$  space, one can study the mean quark energy for a given jet

energy. This is the final correction factor applied to the jets and occurs within the fitting routine itself.

By studying the average quark energy for a given jet energy, one can apply 'parton-level' corrections to the jet to more accurately estimate the energy of the jet [25]. These corrections are derived from top quark Monte Carlo events by examining the quarks from the hadronically decaying W and the b quarks. Separate corrections are applied depending on the flavor of the quark since the response from light flavor and heavy flavor quarks is seen to be different. Figure 7.1.2 shows the invariant mass of the two jets from the hadronically decaying W and the invariant mass of the two jets from a  $Z \rightarrow b\bar{b}$  Monte Carlo sample before and after parton level corrections.

Since the fit is attempted for every jet permutation, the assignment by the fitter between parton and jet varies. While the fit is being performed the jets receive different parton level corrections depending on whether they are considered a light or heavy quark jet in that particular permutation. Without the presence of a tag, there is no *a priori* reason to prefer a particular jet permutation over another. Hence, all permutations are attempted and the one with the lowest  $\chi^2$  is retained as the 'fit mass' for the event. Figure 7.1.2 plots the correct permutation versus the  $\chi^2$  rank of the fit and the value of the  $\chi^2$  for the correct permutation. Note that in order for there to be a 'correct' permutation one must be able to uniquely match all of the partons from the  $t\bar{t}$  decay to the reconstructed jets. This occurs in approximately only 50% of the top quark events due to initial and final state gluon radiation, reconstruction acceptance, jet overlap, and jet reconstruction inefficiency.

With the tagged events the permutations that are inconsistent with the btag should be disregarded (if the jet is correctly identified as a b-jet then these permutations can not be correct). For a single tag this reduces the number of permutations to 6, while with two tagged jets there are only two permutations (depending on which

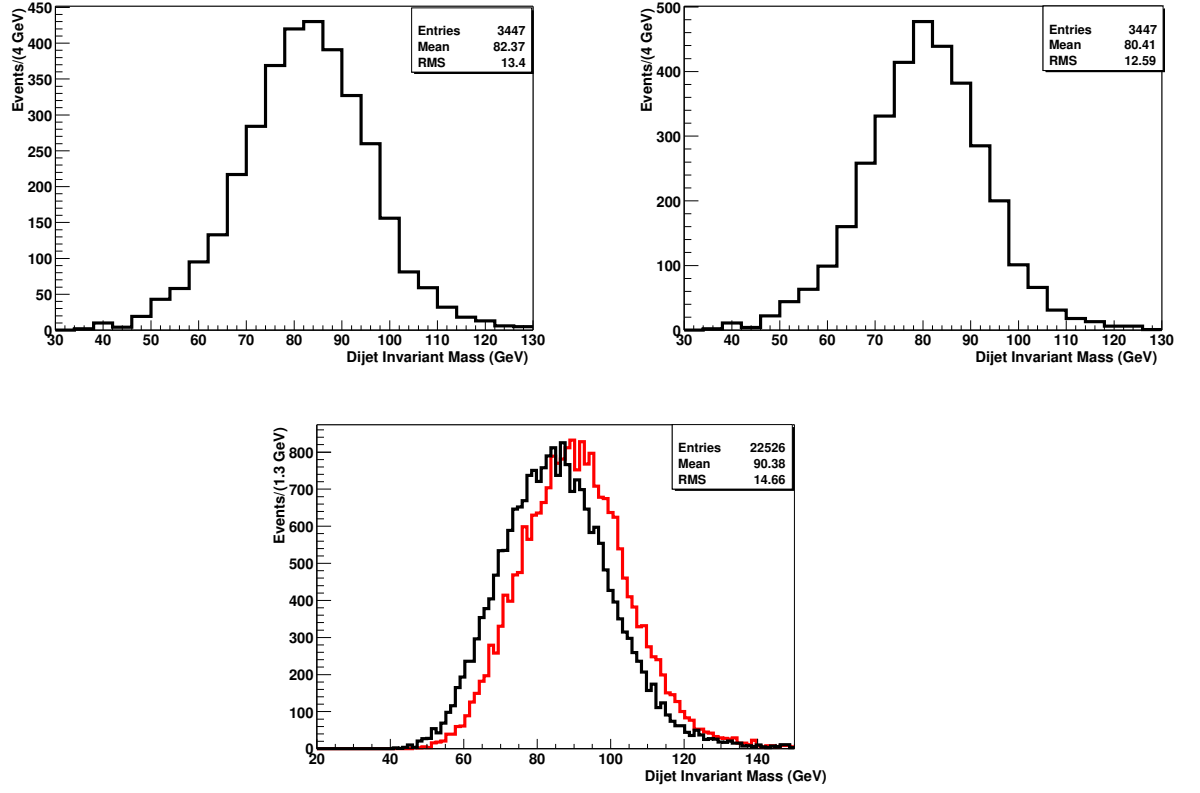


Figure 7.1: W boson invariant mass without parton level corrections (top left), W boson invariant mass with parton level corrections (top right), Z invariant mass with and without parton level corrections (bottom) .

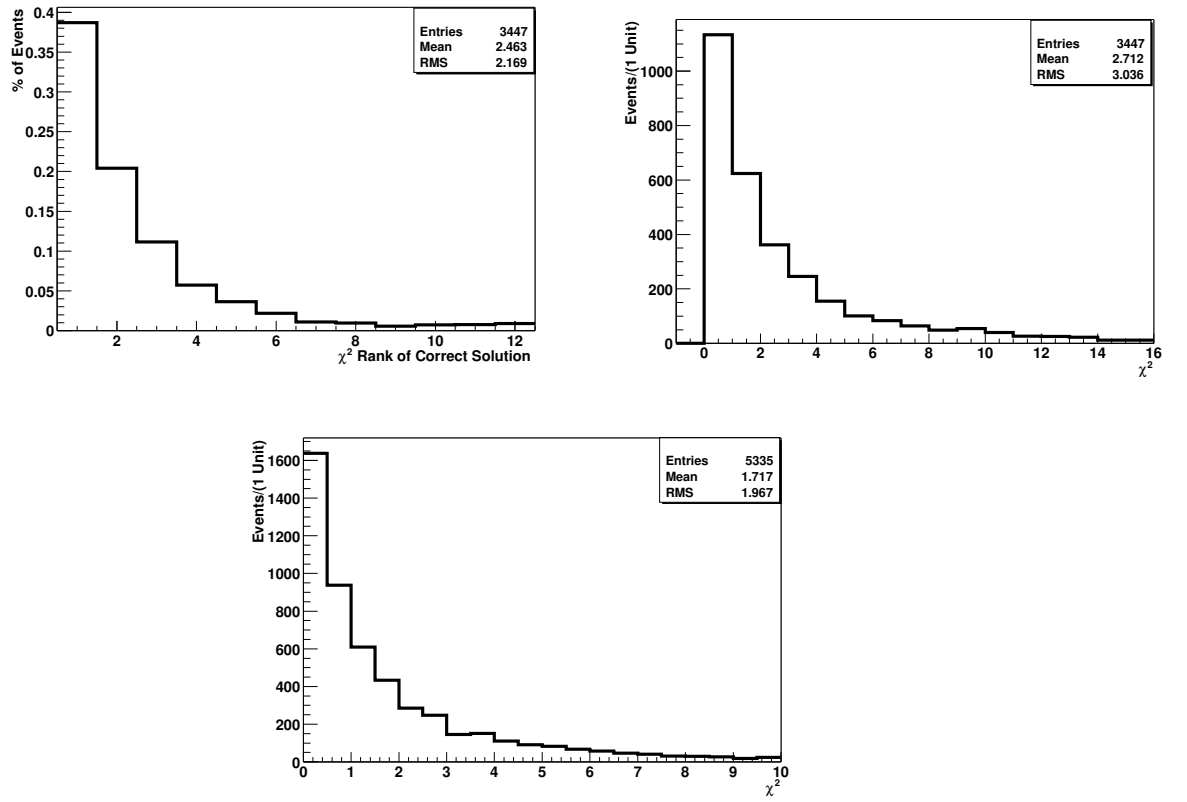


Figure 7.2:  $\chi^2$  rank of the correct permutation (left),  $\chi^2$  for the correct permutation (right), and the distribution for of the lowest  $\chi^2$  solution (bottom).



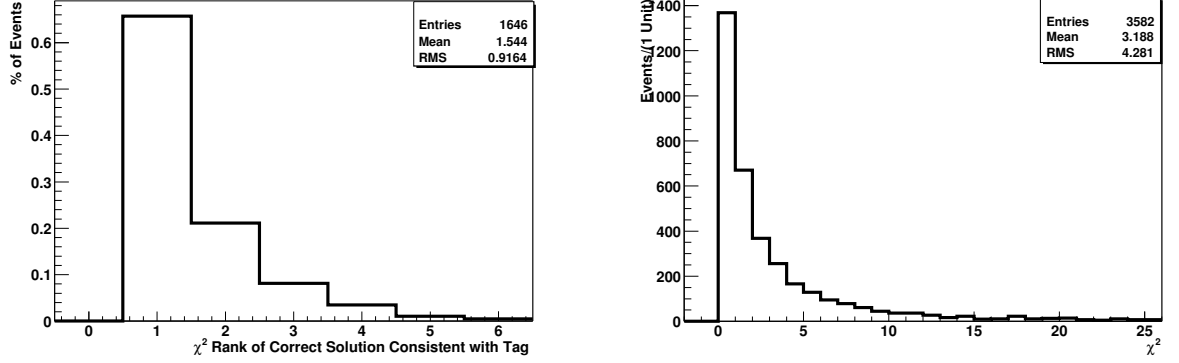


Figure 7.3:  $\chi^2$  rank of the correct permutation consistent with the tag (s) (left) and the distribution for the lowest  $\chi^2$  permutation consistent with the tag (s).

top each b-quark is assigned to). This reduces the number of permutations to consider and hence increases the probability of the lowest  $\chi^2$  permutation being the correct permutation. Figure 7.3 shows the  $\chi^2$  distribution for the tagged events (one or two) in the lowest  $\chi^2$  permutation which is consistent with the fit as well as the  $\chi^2$  rank of the correct solution.

One can evaluate the performance of the kinematic fitting technique by examining the fit mass of the events in the correct permutation. In this case, there is no combinatoric ambiguity or radiative effects that contribute to the width of the distribution. Figure 7.4 shows the fit mass for the correct permutation in events where there is a unique jet to parton match and there are no jets arising from initial or final state gluon radiation for a Monte Carlo sample generated with a top quark mass of 180 GeV as well as the invariant mass of the three jets from the hadronically decaying top. Note that the fit mass has a smaller r.m.s then the hadronic invariant mass. This arises do to the fact that during the fit, a set of kinematic values from the fit is obtained by forcing the measured values to the three constraints described above.

In the actual experiment, we do not have the ability to turn off or ignore jets

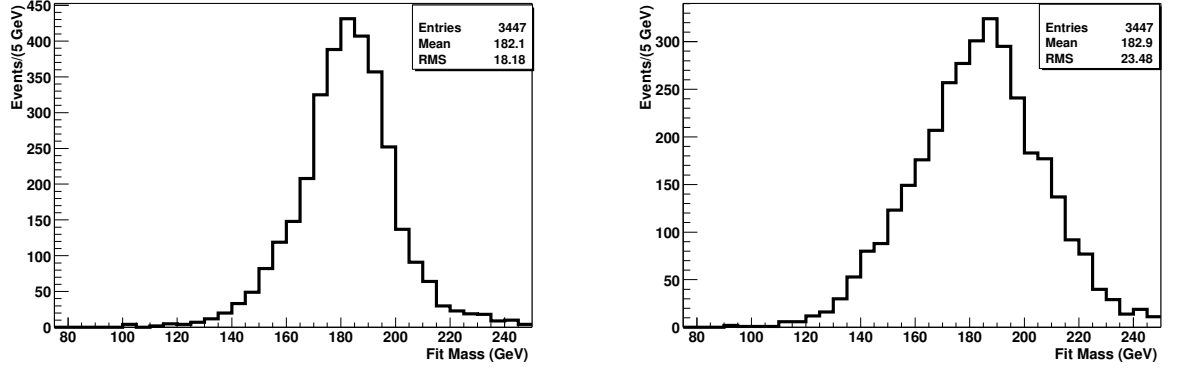


Figure 7.4: Fit mass of parton matched events in the correct permutation (left) and the invariant mass of the three jets from the hadronically decaying top quark (right).

arising from gluon radiation. Nor do we know which jet permutation is the correct one to choose. For this analysis, we simply choose the permutation with the lowest  $\chi^2$  and consider the highest four  $p_T$  jets in the kinematic fit. This leads to a broadening of the fit mass distribution which comes from two sources: choosing jets from gluon radiation and treating them as if they were one of the four jets expected from the top decay, and choosing a permutation which happens to have a slightly better  $\chi^2$  due to detector response and resolution. Figure 7.4 shows the difference in the fit mass resolution resulting from choosing a jet permutation that has a lower  $\chi^2$  from the fit, but is not necessarily matched to correct partons in the event.

Finally, in the case of the actual experiment one of course does not have the privilege of knowing which jet arose from which parton in the top decay. Neither does one know if the jet comes from initial or final state gluon radiation. Some theoretical work on understanding the effects of gluon radiation on the reconstructed top mass [90], [91], [92]. However, experimentally it has been extremely difficult to identify on a jet by jet basis if the jet arose from a quark or a gluon in a hadronic collider [25]. Initial state gluon radiation tends to be emitted in the direction that the initial

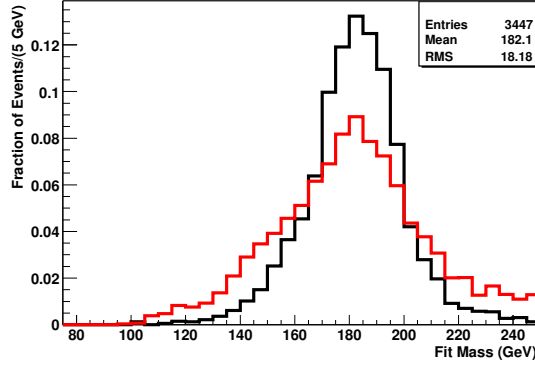


Figure 7.5: Fit mass of all events that pass the event selection in the lowest  $\chi^2$  (red/dashed) compared to the fit mass for parton matched events in the correct permutation.

quarks from the beam were traveling [90] and hence the initial state jet multiplicity peaks in the forward region. Requiring that the jets be in the central region removes the most copious source of jets from initial state gluon radiation. However, final state gluon radiation and gluons radiated at a large angle can still be chosen and treated as one of the four nominal jets in the event. The result of these effects is shown in Fig. 7.5. The distribution is wider as compared to Fig. 7.4. This arises from two effects. First the lower mass tail is primarily caused by final state radiation where not all of the energy in the event is used in the fit. In contrast, the higher mass tail is primarily produced from hard gluon radiation from the initial state where one jet from the initial state is chosen rather than one of the four jets in the fit.

The resolution degradation can be alleviated, to a certain extent by the presence of one or more jets identified as a b-jet. In this case two things occur. First, we can ignore all of the permutations which are inconsistent with the hypothesis of that jet being matched to a b-quark. For events where one jet is identified as a b-jet this decreases the number of permutations to six. In the case of two jets identified as b-jets there are only two permutations (the remaining ambiguity is only which top

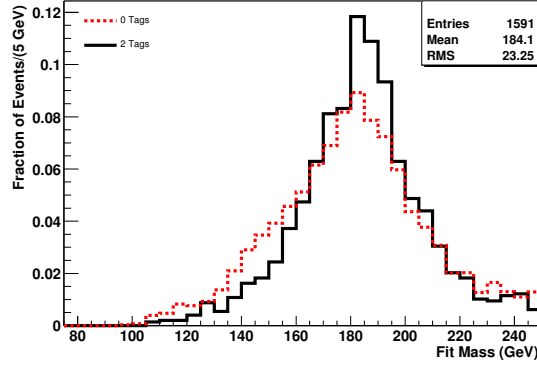


Figure 7.6: Comparison of the fit mass resolution in the lowest  $\chi^2$  permutation consistent with the b-jet identification of two jets to that without any requirement on the b-jet identification.

quark the jet should be assigned to, the one decaying purely hadronically or the one decaying semi-leptonically). Figure 7.6 shows the resolution improvement owing to the reduction of combinatoric background due to the b-jet identification. The r.m.s. of the fit mass distribution is improved by 16 % for the double tagged events.

## 7.2 Likelihood Fitting

### 7.2.1 Fit Description

The template analysis is based on comparing the fitted mass from the kinematic fit on the collider data with the results obtained from fitting simulated Monte Carlo data samples of known top quark masses. In this comparison we use the fitted top quark mass from the permutation with the smallest  $\chi^2$  as the mass estimator. We apply the same event selection on the Monte Carlo events as on the collider data. For each hypothetical top quark mass, we create templates by constructing a histogram of fit masses with 10 GeV wide bins from 80 to 280 GeV. We also construct a background

template from the most prominent background to our decay channel:  $W + 4$  or more jet production.

In order to extract the top quark mass from this comparison, we use a binned likelihood fit. We write the probability distribution function for the mass estimator in terms of the number of signal events,  $n_s$ , and the number of background events,  $n_b$ , in our sample. We constrain the fraction of background events to the expected number using a Poisson probability term.

In each bin, we obtain  $n$  events which have contributions from  $t\bar{t}$  events and background events. For each mass template, the likelihood fit finds the most likely number of signal and background events. We construct our likelihood function to be the product of two Poisson factors. The first factor,  $P_1$  is simply the likelihood of having  $n_s$  signal events and  $n_b$  background events when observing a total of  $n$  events:

$$P_1 = \frac{(n_s + n_b)^n e^{-(n_s + n_b)}}{n!} \quad (7.2)$$

The second factor is a constraint on the number of background events. We can write the expected total number of events as  $\langle n_t \rangle = \langle n_b \rangle (1 + \frac{n_s}{n_b})$  where  $\langle n_b \rangle$  is the expected number of background events. The second factor,  $P_2$ , can be written:

$$P_2 = \frac{\langle n_t \rangle^n e^{-\langle n_t \rangle}}{n!} \quad (7.3)$$

For the fit,  $\langle n_b \rangle$  is obtained from the topological cross-section measurements with the slight differences in event selection taken into account. The likelihood is multiplied together over all mass bins for each template. The likelihood is then minimized as a function of the number of signal and background events. The best fit number of signal and background events is obtained and the likelihood for that sample composition obtained. This procedure is repeated for each template. The

template which has the greatest likelihood, or equivalently the smallest negative log likelihood is identified and a parabola is fit through the templates within  $\pm 15$  GeV (in the topological ensembles)-  $\pm 10$  GeV (in the tagged ensembles) of the template with smallest negative log likelihood. The minimum of the parabola is taken as the most likely top quark mass and the statistical uncertainty is extracted by finding the mass for which the fit to  $-\ln(L)$  rises by  $\frac{1}{2}$ .

To extract the most likely number of signal events, we interpolate between the values of  $n_s$  at the two top quark masses which straddle the minimum of the fit to  $-\ln(L)$ . The actual maximization is performed using the MINUIT package [93]. The templates used for the topological analysis are shown in Fig. 7.7 and those for the tagged analysis in Fig. 7.8.

As discussed in section 6.4 the background is expected to be composed of  $\approx 68\%$  W+jets. The other main source of background is multijet events where one jet is misidentified as an isolated high  $p_T$  lepton. In order to obtain a sample of these and investigate the characteristics of these events the selection for the leptons was changed. In the case of the electron channel, the electron likelihood requirement was reversed and in the muon channel the muon was required not to be isolated. In principle, one could easily obtain larger samples of multijet events by changing some of the kinematic requirements (most notably the requirement on  $\cancel{E}_T$  which is only large for multijet events with significantly mismeasured  $\cancel{E}_T$ ). However, by changing the kinematic selection the characteristics of the events would change and the fit mass distribution would not represent the actual background in the final sample after all event requirements. The fit mass distribution for multijet events is compared to the w+jets fit mass distribution in Fig 7.2.1. The distributions are similar, though not identical, and a Kolmogorov test estimates the probability of the two distributions coming from the same parent distribution at 9.0%. Since most of the background is

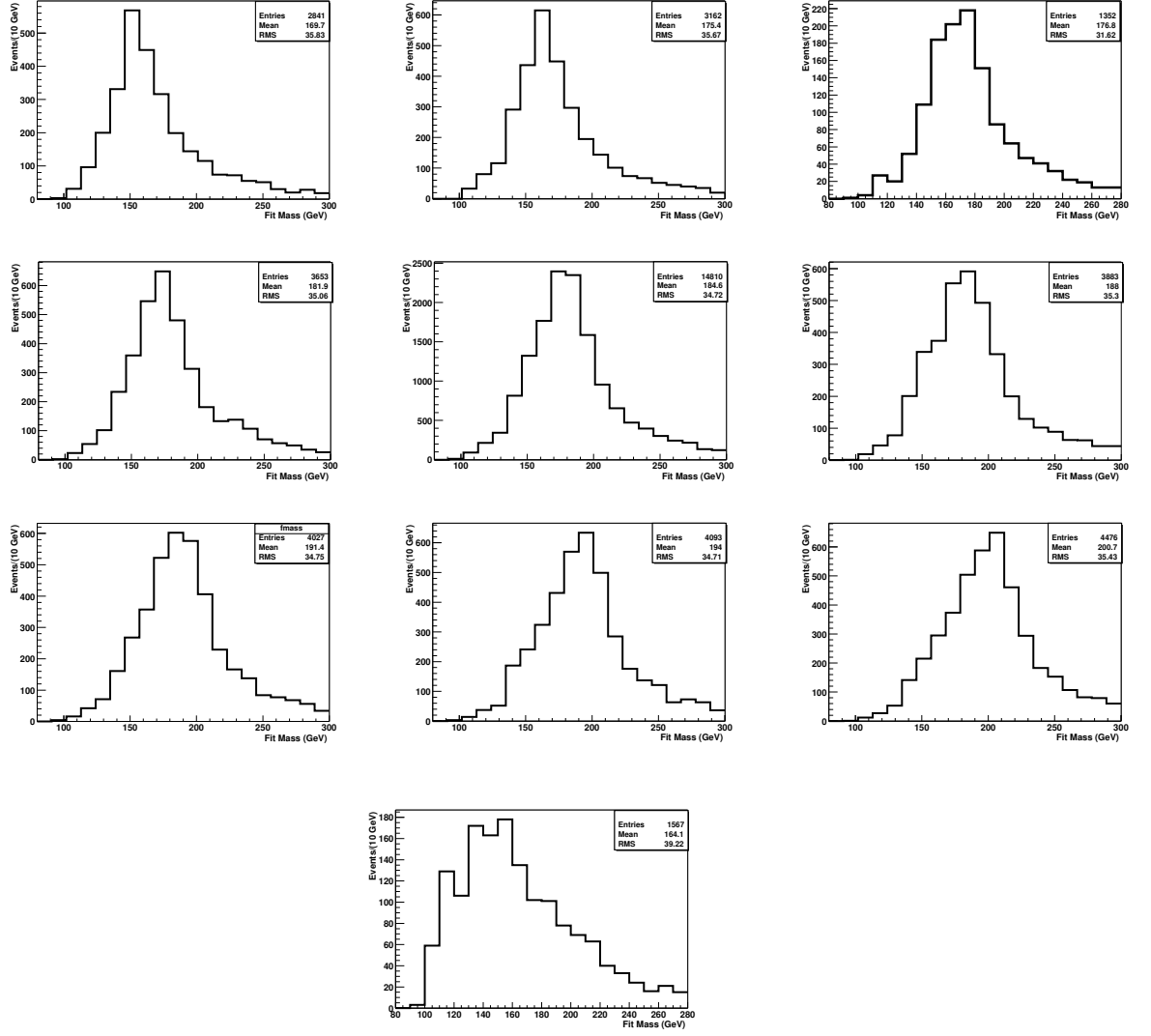


Figure 7.7: Templates for the Topological Analysis (in order from top right to left bottom 150, 160, 165, 170, 175, 180, 185, 190, 200 GeV, the W+jets template is the extreme bottom).

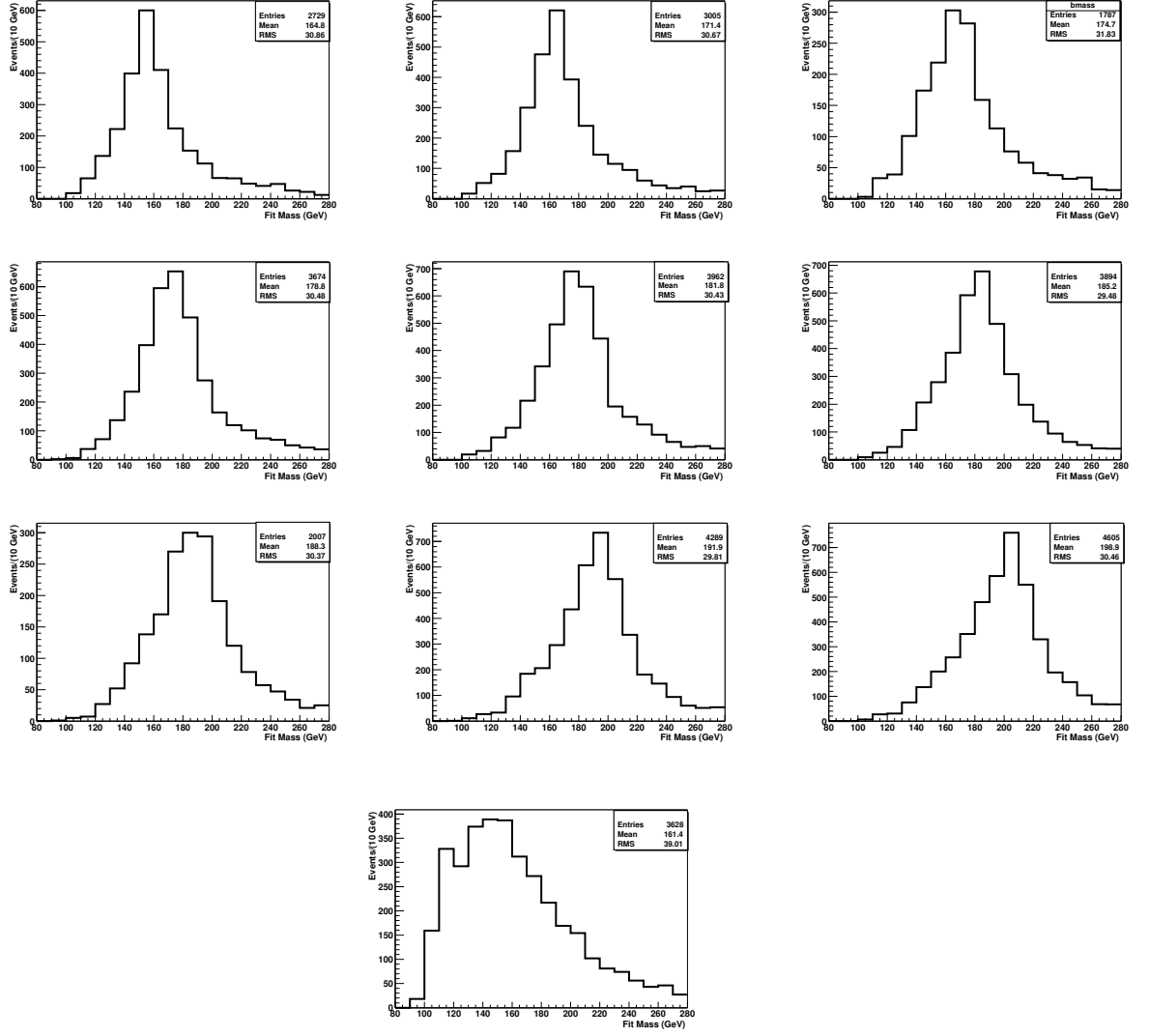


Figure 7.8: Templates for the Tagged Analysis (in order from top right to left bottom 150, 160, 165, 170, 175, 180, 185, 190, 200 GeV, the W+jets template is the extreme bottom).



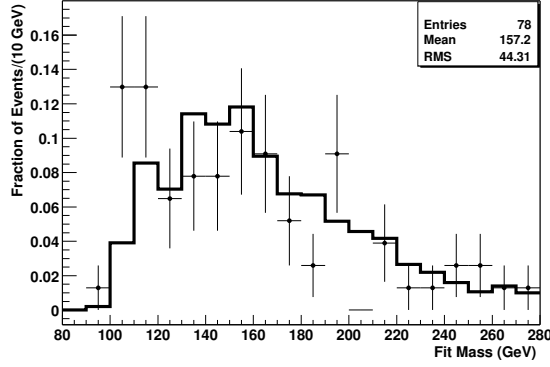


Figure 7.9: Comparison between the W+jets and multijet fit mass distribution.

predicted to W+jets and the fit mass distributions are reasonably similar the W+jets sample was used both for the ensemble testing and in the background template. This is also motivated by the simple fact that the sample size for the multijet background available is quite small.

### 7.2.2 Ensemble Tests

Since the final data sample consists of sample sizes of less than  $\approx 100$  events, it is important to carefully test the statistical properties of the mass extraction procedure. There are several questions one can ask of the mass estimation parameter the most important are that: the procedure is well calibrated, returns errors that are consistent with the statistical spread of the results, and that the procedure is robust. The procedure for testing an estimator's statistical properties is known as ensemble testing. In the actual experiment, there is only one data sample with a true (albeit unknown) signal fraction.

Ensemble testing proceeds as follows. A series of 'mock' experiments is carried out by producing a set of signal and background events from Monte Carlo. The likelihood fit is performed and the most likely top quark mass and its error along

with the estimated number of signal events and its error is retained. In the case of Monte Carlo we know the input top quark mass used for events generation with and the sample composition precisely. This procedure is repeated several times with many different ensembles to judge the performance of the method.

For each ensemble, the fit mass of the events is binned in exactly the same way as in the analysis of data.. Then the likelihood fit is performed on the ensemble and the extracted top quark mass and the error assigned by the likelihood fit is stored. In a likelihood method, one does not have to use the fit mass for the event as the estimator. In principle, any quantity of the event that is correlated with the mass of the top quark could be used to estimate the mass of the top if one can extract the correspondence between the chosen estimator and the top quark mass. In this case, the kinematic fit mass was chosen because of the obvious high degree of correlation between the kinematic fit mass and the 'true' top quark mass. However, in order to understand the performance of the chosen estimator one needs to understand two quantities:

- The bias  $b = \langle \hat{m} \rangle - m_{true}$
- The variance  $V = \sqrt{\langle \hat{m}^2 \rangle - \langle \hat{m} \rangle^2}$

In principle, one would like there to be no bias and to choose an estimator with the best resolution possible. As well, ensemble tests allow for a careful examination of the estimator extraction procedure. There are three important questions that can be answered by ensemble tests. Does the chosen estimator have a bias? What is the expected resolution or error on the measurement? Are the errors that are returned by the likelihood fit consistent with the statistical spread of the ensembles?

The first question can be answered by generating many different Monte Carlo samples with different values of the parameter. This corresponds to generating Monte

Carlo samples with several different hypothetical values for the top quark mass. The fitting procedure is then run over this series of ensembles. If the method is unbiased the average of the ensemble extracted masses will be consistent with the known input value over a range of hypothetical top quark masses.

The second question can be answered by examining the distribution of statistical errors returned by the likelihood fit. The median of the ensemble error distribution is the most likely actual value for the statistical error in data. This allows one to test the statistical power of the method by examining the error distribution. Secondly, when the fit is performed on data, it allows one to make a statement on how likely the statistical error achieved in data is, when compared to the expected statistical error seen in ensemble tests.

The final question can be answered by forming the 'pull' distribution for the ensembles. For each ensemble we can define the quantity:

$$pull = \frac{m_{top} - m_{true}}{\sigma_{m_{top}}} \quad (7.4)$$

One would expect that given a large number of ensembles the errors returned by the fit would be consistent with the observed statistical fluctuations away from  $m_{true}$ . Specifically, one would expect that:

- The pull distribution would have a mean of 0. On average  $m_{top} - m_{true}$  should be zero.
- The pull should be Gaussian distributed with a sigma ( $\sigma$ ) of 1.0. The fluctuation of the extracted top quark mass around the true top quark mass should be equal to the average  $\sigma_{m_{top}}$ .

The results of the ensemble tests performed for the topological and b-tagged anal-

ysis are described below. Monte Carlo samples were generated with the following hypothetical top quark masses (in GeV): 150, 160, 165, 170, 175, 180, 185, 190, and 200.

### Ensemble Tests with Topological Selection

In the case of the topological selection, there were 167 candidate events. After the  $\chi^2$  and discriminant requirement there were 146 and 94 events (respectively). The ensemble tests were performed by composing ensembles with 146 events with the expected background fraction of 60 %. During the formation of the ensembles the likelihood requirement was made such that on average the ensembles had 94 events with the expected sample composition after all event requirements. The total number of events is fixed however the number of signal and background events is allowed to fluctuate within binomial errors. This is done to reflect the fact that the sample composition in data is only estimated and the actual number of  $t\bar{t}$  events may not be the predicted central value.

The first step was decide the optimal requirement on the low bias discriminant. A series of ensemble tests with various requirements on the discriminant. The discriminant was varied from 0.2 to 0.7. As shown in Fig. 7.10 the expected statistical uncertainty is minimized by requiring the discriminant to be larger then 0.4 (although the curve is quite shallow in the area around the minimum).

In order to study any possible bias in the method, for each hypothetical top quark mass, 200 ensembles were formed using the sample composition described above. The likelihood fit was performed on each of the ensembles. Figure 7.11 shows the output of the likelihood fit for the 200 ensembles using the 175 GeV Monte Carlo. Note that a few percent of the ensembles do not converge. This occurs for one of two reasons: either the likelihood curve becomes inverted so that their is no fit minimum or the

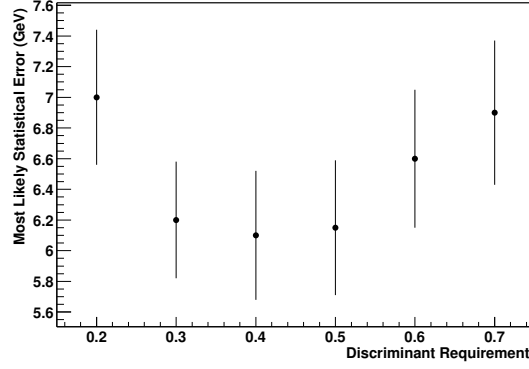


Figure 7.10: The most likely statistical uncertainty as a function of the requirement on the discriminant.

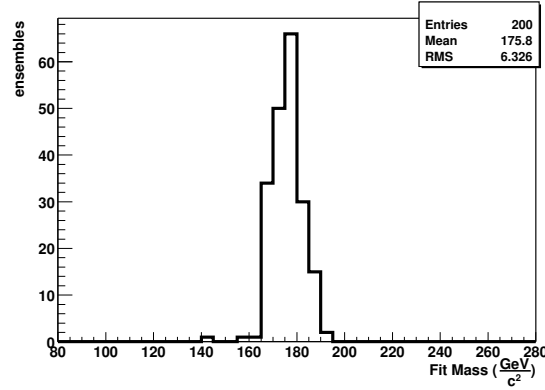


Figure 7.11: The extracted top quark mass for 200 ensemble tests using the topological event selection.

likelihood curve does not minimize in the range between the smallest and largest mass template. In either case, the answer returned by the minimization has no meaning and is removed from the set of ensembles. This occurs between 0-4% of the ensembles.

The same procedure was then performed on the various mass points in order to extract a calibration curve. For each mass point, the ensemble average was taken as the central value and the uncertainty on the extracted mass for that set of ensembles is given by  $\frac{r.m.s}{\sqrt{N_{ensembles}}}$ . A linear fit was then performed on the resulting ensemble

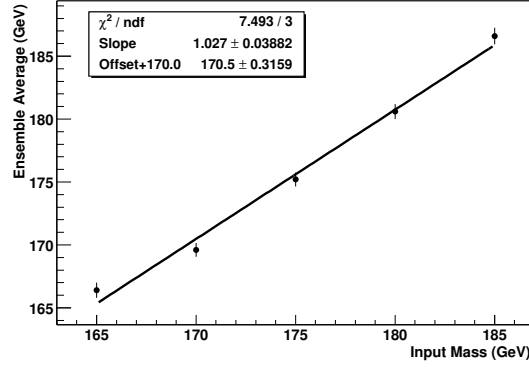


Figure 7.12: Calibration curve obtained from ensemble tests using the topological event selection.

points, and the results are shown in Fig. 7.12. Note that the fit was performed centering the offset at 170 GeV rather than setting the offset to be evaluated at the y-intercept. This is done because this is the closest sample to the fit mass extracted in data. One would like to know if there is any bias around the point actually seen in data. Also, if it were centered around the y-intercept the fit would extrapolate all the way back to the intercept while the points range from 165-185 GeV and hence would have a larger uncertainty associated with the fit. The fitted slope is consistent with unit slope well within  $1\sigma$ , the offset at 170 GeV is measured to be about 0.4 GeV and is consistent with zero within about  $2\sigma$ . Note that if this offset is not simply a statistical fluctuation it is an order of magnitude smaller than the expected statistical uncertainty and therefore does not contribute significantly to the uncertainty of the method.

The pull distribution for the 170 GeV ensembles is shown in Fig. 7.13. It is consistent with a Gaussian centered at zero and with a sigma slightly less than one. This shows that the uncertainties assigned from the fit are consistent with the statistical spread of the ensembles. Hence, when the fit is performed on data one can

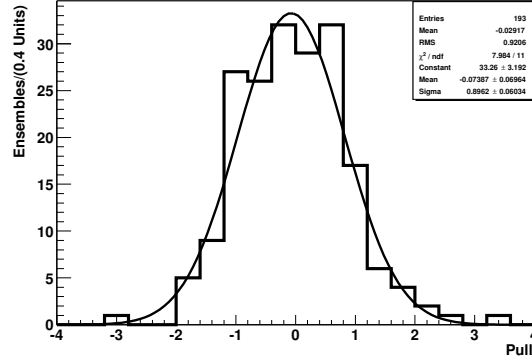


Figure 7.13: Pull distribution of the 170 GeV ensembles fit with a Gaussian.

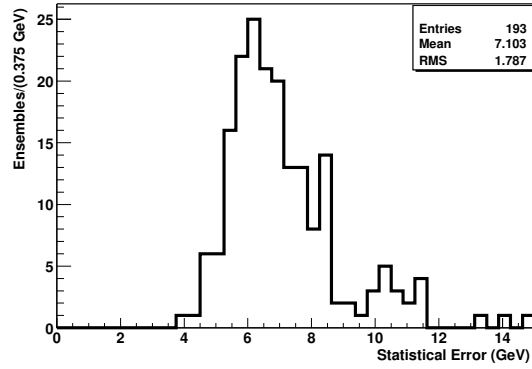


Figure 7.14: Expected statistical uncertainty in the topological analysis from the 170 GeV ensembles.

be assured that the uncertainty assigned from the likelihood fit is the standard  $1\sigma$  confidence level [6]. The ensemble mass average and uncertainty as well as the  $\sigma$  and uncertainty from the pull distributions using the various mass points as inputs to the ensembles is shown in Table 7.1.

Finally, one can evaluate the estimated statistical power by examining the expected statistical uncertainty from the ensemble tests. The results from the 170 GeV ensembles are shown in Fig. 7.14. The mean of the uncertainty is about 7.1 GeV while the most likely value (the mode) is approximately 6.1 GeV.

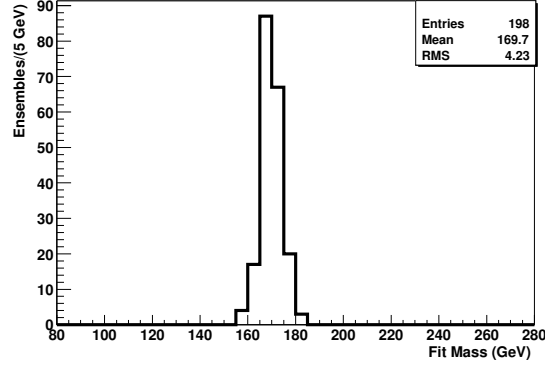


Figure 7.15: The extracted top quark mass for 200 ensemble tests using the tagged event selection

### Ensemble Tests with b Tagged Selection

The same procedure that is described in the previous section was also performed with ensembles using the b tagged event selection. In data there are 69 tagged events with a signal fraction estimated to be  $\approx 76 \pm 10\%$ . Ensembles were formed in the same way as described in the topological case but with the number of events and signal fraction appropriate to the tagged selection. The distribution of extracted masses from the likelihood fit for the ensembles generated with 170 GeV  $m_{true}$  is shown in Fig. 7.15.

Ensembles were formed for the various input top quark masses and the calibration curve was obtained. The procedure is identical to the case described in the section before. Again, the linear function was chosen to put the offset closest to the measured mass in data to evaluate any possible deviation from linearity or bias at the measured point. The results are shown in Fig. 7.16. A very similar performance is seen in the calibration curve with respect to the topological analysis. A summary of the ensemble tests is presented in Table 7.2.

The pull distribution for the 170 GeV ensembles is shown in Fig. 7.17. The



Input Mass (GeV)	Ensembles	Average (GeV)	Error (GeV)	Pull $\sigma$	$\sigma$ Error
165	196	166.4	0.60	0.87	0.05
170	194	169.6	0.55	0.89	0.06
175	198	175.2	0.55	0.93	0.05
180	196	180.6	0.60	0.87	0.05
185	192	186.6	0.65	0.87	0.05

Table 7.1: Summary of the Topological Ensemble Tests

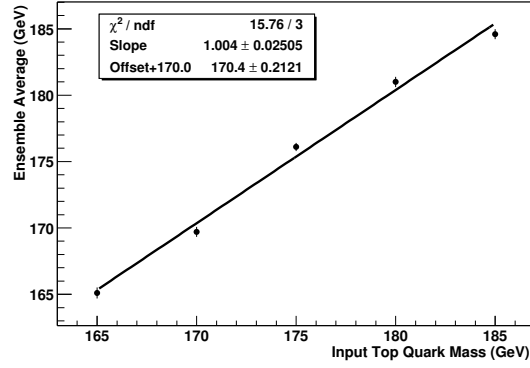


Figure 7.16: Calibration curve obtained from ensemble tests using the tagged event selection.

Input Mass (GeV)	Ensembles	Average (GeV)	Error (GeV)	Pull $\sigma$	$\sigma$ Error
165	195	165.1	0.42	0.96	0.07
170	198	169.7	0.38	0.91	0.07
175	200	176.1	0.48	0.93	0.06
180	197	181.0	0.39	0.92	0.07
185	194	184.6	0.39	0.92	0.08

Table 7.2: Summary of the Tagged Ensemble Tests

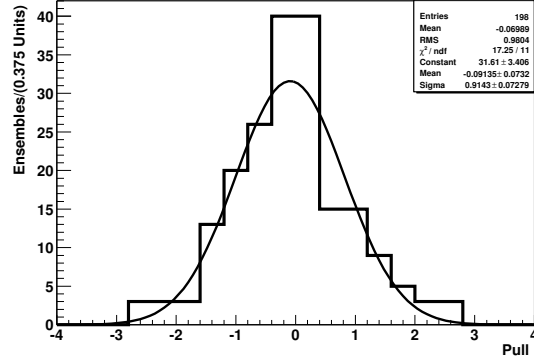


Figure 7.17: Pull distribution of the 170 GeV ensembles fit with a Gaussian with unit width.

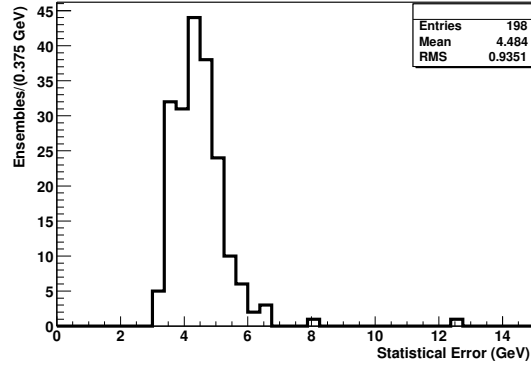


Figure 7.18: Expected statistical uncertainty in the tagged analysis from the 170 GeV ensembles.

distribution has been fit with a Gaussian which has a mean consistent with 0 and a  $\sigma$  consistent with unity. Finally, the expected statistical uncertainty is shown in Fig. 7.18. In the tagged analysis the most likely value (mode) of the statistical uncertainty is about 4.2 GeV while the mean is about 4.5 GeV.

## Chapter 8

# RESULTS WITH COLLIDER DATA

*'In theory, there is no difference between theory and practice. In practice, there is a big difference'*

Yogi Berra

In this chapter, the results obtained from collider data are presented for both the topological selection and the tagged selection. A detailed description of the various sources of systematic uncertainty and how they were estimated is presented along with a list of the various cross-checks that were performed.

### 8.1 Results with the Topological Selection

As discussed previously, there are 94 events that pass the final topological event selection. From the cross-section measurement [86] (taking into account the efficiencies for the extra event requirements of a good  $\chi^2$  fit from the kinematic fit and the topological discriminant requirement) the expected number of background events is

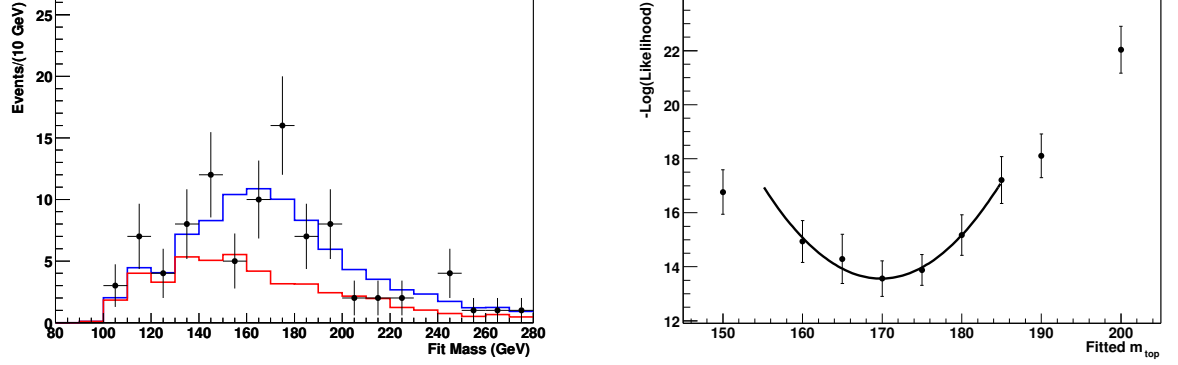


Figure 8.1: The likelihood curve from the fit of the topologically selected events (left). The distribution of fit masses of the topologically selected events (right). The red curve is the expectation from background only events (normalized to the fraction preferred by the fit) while the blue curve is the sum of the expectation from signal and background for the mass point closest to the fit result.

$45.1 \pm 8.2$  events while the expected number of signal events is  $48.9 \pm 8.8$ . The fit mass distribution for the 94 data events are shown in Fig. 8.1 (left plot). A likelihood fit to the fit mass distribution as a function of the assumed top quark mass is shown in Fig. 8.1 (right plot). The result of the likelihood fit leads to a measurement of the top quark mass of  $169.9 \pm 5.8 \frac{\text{GeV}}{c^2}$  (statistical uncertainty only). The number of  $t\bar{t}$  events is determined to be  $44.2 \pm 6.6$ .

Figure 8.2 shows the topological discriminant for the events (relaxing the selection on the discriminant itself). For both the fit mass distribution (Fig. 8.1 left) and the topological likelihood (Fig. 8.2) we overlay the the signal and background distributions. The expectations of the signal and background events are those determined by the likelihood fit. We note that the predicted distributions match the observed distributions in data very well. As shown in Fig. 8.3, the statistical uncertainty on the measurement seen in data is quite close to the expected statistical uncertainty from ensemble tests.

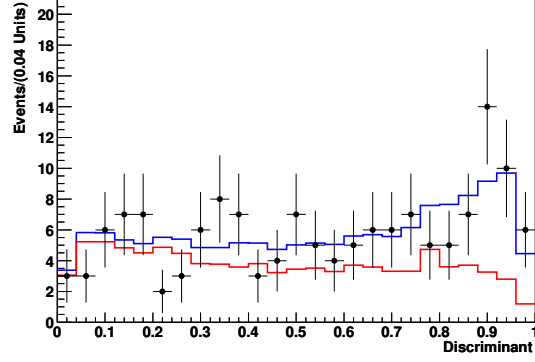


Figure 8.2: The distribution of the topological discriminant of the preselected events (without requirement on the topological discriminant). The red curve shows the expected distribution from background only and the blue curve is the expected distribution from signal and background (normalized to the number of data events with the signal to background returned from the likelihood fit).

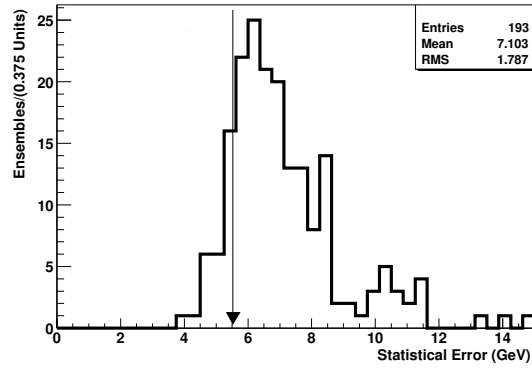


Figure 8.3: The distribution of statistical uncertainties from ensemble tests of the  $t\bar{t}$  sample with input mass of 170 GeV. The result in data is marked by the large arrow.

Table 8.1 shows the negative log likelihood value for each template point in the fit.

Template Mass (GeV)	-Log(Likelihood)	Likelihood Uncertainty
150	16.62	0.79
160	14.73	0.82
165	14.06	0.73
170	13.46	0.68
175	13.74	0.60
180	14.91	0.65
185	16.92	0.68
190	17.71	0.72
200	21.34	0.84

Table 8.1: Fit results for variations of the topological discriminant requirement.

## 8.2 Results with the Tagged Selection

As discussed in section 5.5, 69 events are selected from the tagged event selection. From the cross-section [86] measurement, and after folding in the additional efficiencies of the kinematic fit  $\chi^2$  convergence requirement, the number of signal events is expected to be  $52.4 \pm 4.2$ . A likelihood fit to the fit mass distribution as a function of the assumed top quark mass is shown in Fig. 8.4 (right plot). The result of the likelihood fit leads to a measurement of the top quark mass of  $170.6 \pm 4.2$  GeV (statistical uncertainty only). The number of  $t\bar{t}$  events is determined to be  $49.2 \pm 6.3$ .

Figure 8.5 shows the topological discriminant for the events. As in the case of the topological selection, the signal fit mass distribution and topological discriminant is very well reproduced by Monte Carlo expectations with the signal to background ratio chosen by the fit. Figure 8.6 shows that the statistical uncertainty on the measurement in data is quite close to the expected statistical uncertainty from ensemble tests.

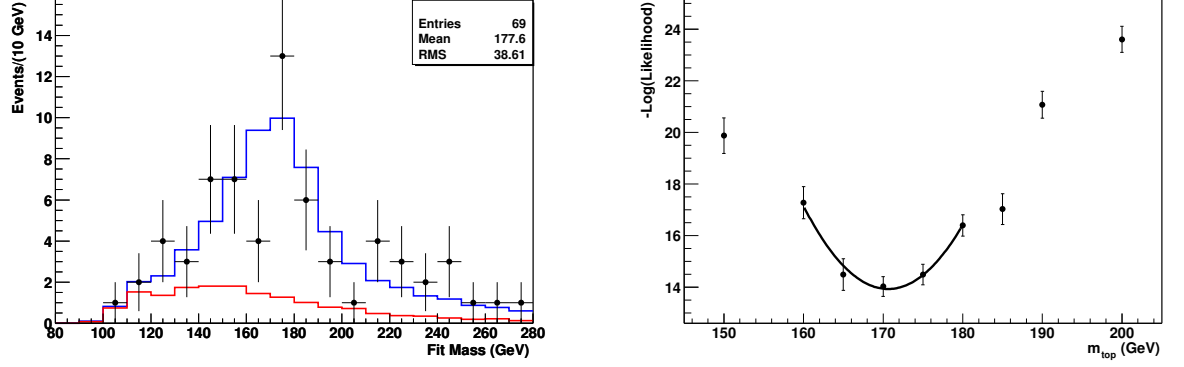


Figure 8.4: The likelihood curve from the fit of the tagged event selection (left). The distribution of fit masses of the events (right). The red curve is the expectation from background only events (normalized to the fraction preferred by the fit) while the blue curve is the sum of the expectation from signal and background for the mass point closest to the fit result.

Table 8.2 shows the negative log likelihood value for each template point in the fit.

Template Mass (GeV)	-Log(Likelihood)	Likelihood Error
150	19.87	0.68
160	17.27	0.62
165	14.49	0.61
170	14.03	0.38
175	14.49	0.39
180	16.39	0.41
185	17.03	0.59
190	21.07	0.52
200	23.60	0.50

Table 8.2: Likelihood Values for the Tagged Analysis.

Figure 8.7 shows the fit mass versus the discriminant value for both the tagged and topological event selection.

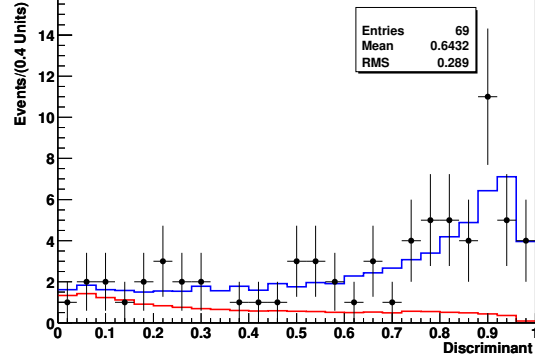


Figure 8.5: The distribution of the topological discriminant of the tagged events. The red curve shows the expected distribution from background only and the blue curve is the expected distribution from signal and background (normalized to the number of data events with the signal to background returned from the likelihood fit).

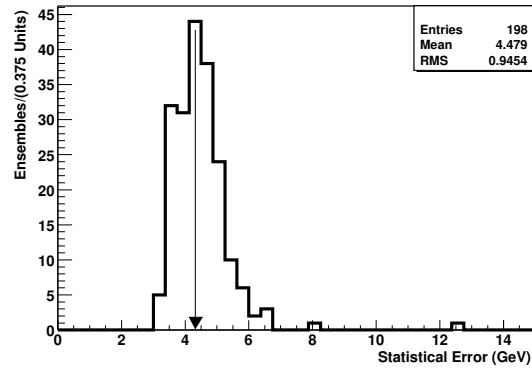


Figure 8.6: The distribution of statistical uncertainties from ensemble tests from a  $t\bar{t}$  sample with input mass of 170 GeV. The result in data on the tagged sample is marked by the large arrow.



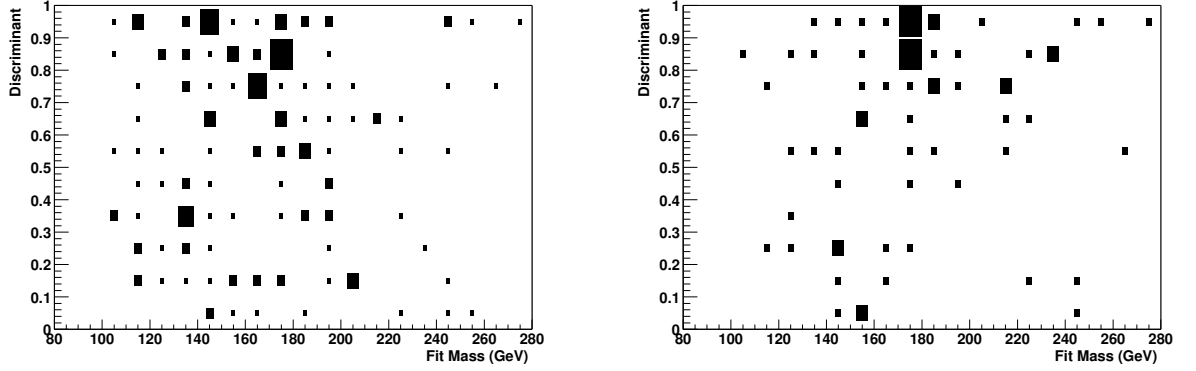


Figure 8.7: Fit mass versus discriminant value for the topological selection (left) and the tagged selection (right).

### 8.3 Systematic Uncertainty

Along with the statistical fluctuations associated with a sample with limited statistics there are a number of sources of error that could systematically lead to uncertainties on the top quark mass measurement. This section discusses the systematic uncertainties on the top mass determination. All systematic uncertainties were evaluated using the 175 GeV  $t\bar{t}$  templates as the nominal value. In the case of the topological analysis the nominal value from ensemble testing was found to be 175.2 GeV while in the tagged analysis the nominal value was 176.1 GeV. All variations are quoted from these central values.

#### 8.3.1 Jet Energy Scale Uncertainty

The dominant source of systematic uncertainty comes from the uncertainty associated with the jet energy scale. As discussed in section 4.6.3 because of the use of a sampling calorimeter, out of cone showering, dead material, non-linearities, and noise, the energy of a jet is almost always less than the energy of the particles that produced the jet. Therefore, the energies of the reconstructed jets must be scaled in order to

reproduce the correct energy of the underlying particles. In the  $t\bar{t}$  lepton + jets decay final state, there are nominally four jets. Since the top quark mass is reconstructed from the charged lepton, missing transverse momentum, and the jets in the event, the scale which is applied to the jet energies is of crucial importance to the measurement. The final state contains at least four jets and only one charged lepton. Since the jet energy scale is applied to all of the jets in the event, it is the most important factor in determining the total reconstructed energy of the event. As well, the jet energy scale is less precisely known than the lepton energy scale which further magnifies its importance to the measurement.

Since the method used to extract the top quark mass relies on templates constructed from Monte Carlo samples, by far the largest effect is the difference between the jet energy scale in data and Monte Carlo. This can be understood from the following simple example. Suppose that the energies of the jets were systematically shifted downward by 10%. In terms of the kinematic fit, this would mean that the invariant mass of dijet pair from the hadronically decaying  $W$  and the invariant mass of the hadronically decaying top quark would also be shifted downward by 10%. However, if this were the case in both collider data and Monte Carlo simulation the templates constructed from Monte Carlo would be systematically shifted down by 10%. Therefore, when using the shifted templates the top quark mass resulting from the fit would have this 10% shift accounted for and the extracted top quark mass would be exactly the same if there was not a shift at all. This serves to illustrate that what is most important is that the jet energy scale in data matches the jet energy scale in Monte Carlo.

In order to evaluate the difference between the jet energy scale in data and Monte Carlo, it is necessary to have a sample in data where one can accurately compute the jet energy scale. A convenient sample is composed of events where there is

one jet balanced by the recoil of a high energy photon. Since the resolution for electromagnetic objects is much more precisely known than hadronic objects, one can make the approximation that the energy of the photon is correctly reconstructed. Hence, the transverse momentum of the photon must be balanced by the transverse momentum of the jet.

In order to parametrize the difference in the jet energy scale seen between data and Monte Carlo it is convenient to define the ratio:

$$\Delta S = \frac{E_T^{Jet} - E_T^\gamma}{E_T^\gamma} \quad (8.1)$$

where  $E_T^{Jet}$  is the 'transverse energy' of the jet, and  $E_T^\gamma$  is the 'transverse energy' of the photon. This simple ratio gives the fractional difference in the reconstructed energy between the jet and the photon.  $\Delta S$  is plotted as a function of the jet detector eta in Fig. 8.8 [72]. The difference between data and Monte Carlo is shown in Fig. 8.9 [72].

In order to estimate how this difference impacts the top quark mass measurement the difference shown in Fig. 8.9 was parameterized in the following way. For jets with transverse energies above 30 GeV the relative data to Monte Carlo uncertainty was taken to be 5%. For jets with transverse energies below 30 GeV, the percent difference was taken to depend on the jet energy and is given by:

$$relative\ uncertainty = 30\% - \frac{20\%}{30\ GeV} \times E_T^{Jet} \quad (8.2)$$

This form was used in order to take into account the slow rise in the difference between data and Monte Carlo in the case of jets with transverse energies between 20 and 30 GeV. This contour then represents a  $\pm 1\sigma$  band for the relative uncertainty on the jet energy scale between data and Monte Carlo. The Monte Carlo samples

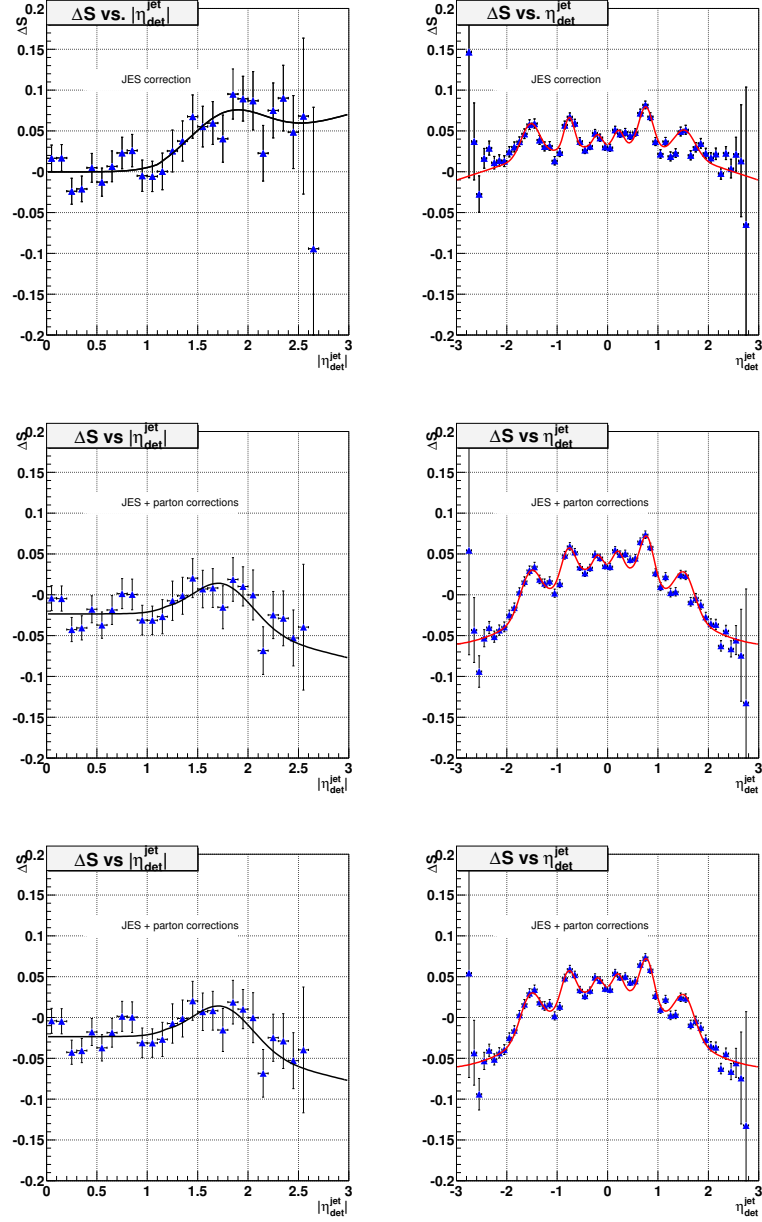


Figure 8.8: The jet energy scale deviation  $\Delta S$  as a function of jet  $\eta$  (det) for Monte Carlo (left) and for data (right) after basic JES correction (top), after JES+parton-level corrections, after eta-dependent adjustments (bottom).

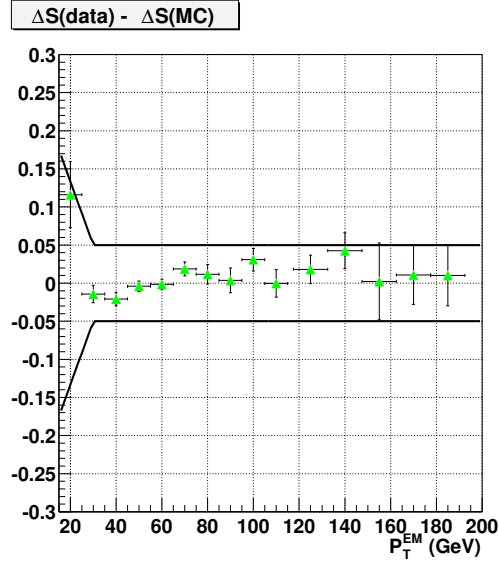


Figure 8.9:  $\Delta S_{data} - \Delta S_{MonteCarlo}$  as a function of  $\gamma p_T$ . Displayed band shows relative JES error used to estimate JES uncertainty.

were then reprocessed twice once with the energy scale increased by the  $1\sigma$  contour and once with the jet energy decreased by the  $1\sigma$  contour. The shift in the fit mass distribution for signal and background is shown in Fig. 8.10.

The systematic uncertainty from the jet energy scale was assigned by taking Monte Carlo samples where the jet energy scale had been shifted up and down according to the above procedure. The templates for the fit remained the same. In this way, one can estimate the effect of the shift on the top quark mass by examining the average ensemble fit mass from the likelihood fits. With the jet energy scale shifted up by  $1\sigma$  in the  $t\bar{t}$  sample the ensemble average was found to be 182.0 and with the jet energy scale shifted down by  $1\sigma$  the ensemble average was 168.7. This leads to a variation of +6.8 GeV and -6.5 GeV. In the case of the tagged analysis one more step was added. Since the probability to identify a jet with a secondary vertex is dependent on the jet  $p_T$ , the jet energies were also varied up and down by the same amount before calculating the probability of a tagging a jet in Monte Carlo. This

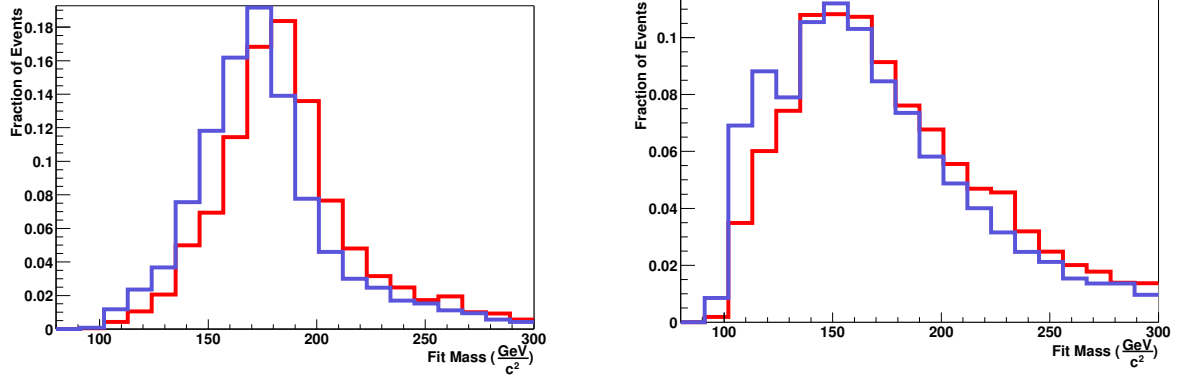


Figure 8.10: Variation of the fit mass distribution with the  $\pm 1\sigma$  contours for signal (left) and background (right).

needs to be taken into account since effects the sample composition and the resolution in the fit mass distribution. Shifting the jet energies up by  $1\sigma$  the ensemble average was found to be 180.8 GeV, while shifting the jet energies down by  $1\sigma$  the ensemble average shifted to 170.8 GeV. Hence there was a variation of +4.7 GeV and -5.3 GeV. As a cross-check the jet energy scale uncertainty was also evaluated without varying the jet energy scale for the tagging probabilities and a variation of +4.1 and -4.2 GeV was found (ensemble averages of 171.9 and 180.2 GeV). This indicates that the size of the effect of the tagging probabilities is about 0.5 - 1.1 GeV. In both the topological selection and the tagged selection there is an effect from the jet energy scale arising from the shift in the signal and background fit mass distributions. For the tagged selection the signal fraction is much higher and the shift seen in the ensemble tests is almost entirely due to the shift in the signal fit mass distribution. This is confirmed by simply performing the topological ensemble tests but using the signal fraction of the tagged selection. In this case the uncertainty in the topological selection from the jet energy scale is reduced to the uncertainty obtained in the tagged selection.

### 8.3.2 Gluon Radiation

As mentioned in previous chapters, although the nominal  $t\bar{t}$  lepton + jets event has a final state of four jets, a charged lepton, and a neutrino,  $\approx 40\%$  of these events are expected to have an extra jet from either initial or final state gluon radiation. There has been some theoretical work dedicated to the study of gluon radiation in top decays [90] [91] [92] but owing to the limited samples of top quark events produced there is little experimental work on the subject.

The effect on the kinematic mass fit depends on the source of the gluon. Recall that in this work the four highest  $p_T$  jets are used in the mass fit. If there are other jets, they are not used in the mass fit (other than their effect on the missing transverse energy). If one of the initial state quarks radiates a hard gluon that hadronizes and becomes one of the four highest  $p_T$  jets in the event it will be used in the mass fit. *A priori*, we know that regardless of what jet permutation is used, the fit mass will not be the correct mass for the event. The energy from the initial state gluon jet is not from the  $t\bar{t}$  system and hence should not be used in the mass reconstruction. This has a tendency to produce higher mass solutions and a broadening of the fit mass distribution. If the gluon radiates from one of the final state quarks at a large enough angle the energy of that quark is split into two jets. Since only the four highest  $p_T$  jets are used the fit mass will again be incorrect and leads to lower mass solutions since not all the energy of the  $t\bar{t}$  system is included in the fit. In this case one could argue that one could extend the number of jets that are used in the fit. However, it has been shown that the combinatoric explosion leads to a much larger background of incorrect permutations. For example, for 6 jets there are already over 1,000 permutations [88].

In order to understand the effects of gluon radiation one can examine the properties of the jets from gluons in Monte Carlo in the  $t\bar{t}$  sample generated with a top

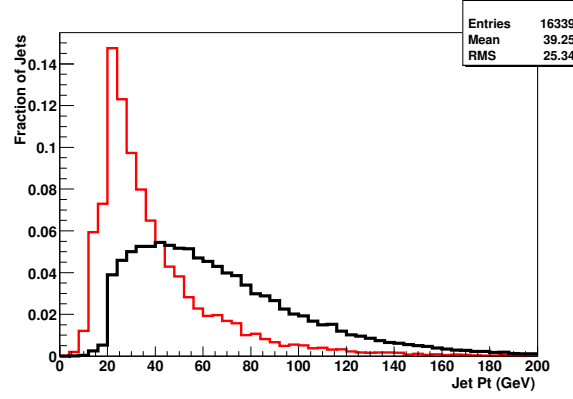


Figure 8.11: Jet  $p_T$  spectrum for jets from the primary partons (blue) and gluons (red).

quark mass of 175 GeV. Figure 8.11 shows the  $p_T$  spectrum of jets from one of the four primary quarks in the lepton + jets decay compared to the  $p_T$  spectrum of jets from gluons.

Since there is essentially no previous experimental guidance on gluon radiation in top quark decays, Monte Carlo must be used and trusted to provide the right number of gluon jets with the correct properties. To understand the effects this has on the top quark mass reconstruction, the events in Monte Carlo with only four partons hadronizing and forming four jets were compared to the events where one gluon jet was used in the kinematic fit. The results are shown in Fig. 8.12. As one expects, the effect of gluon radiation is to widen the fit mass distribution. Taking a conservative stance, the systematic uncertainty from gluon radiation was taken by selecting events with gluon radiation not present and events where one of the jets used in the kinematic fit was from a gluon. The two selections were used to form ensembles and compared to the nominal ensemble results. For the topological analysis with events with no gluon radiation the ensemble average was found to be 174.9 GeV. While the events with gluon radiation had an ensemble average of 177.8 GeV. The variation from



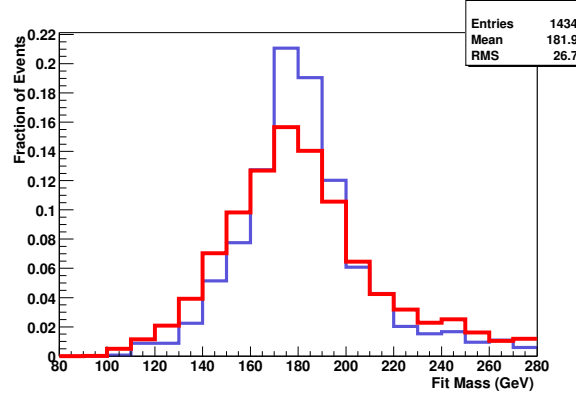


Figure 8.12: Fit mass distribution for events with (red) and without (blue) gluon radiation.

nominal is thus found to be 0.2 GeV for the events without gluon radiation and 2.6 GeV with the events with gluon radiation. Added in quadrature the total uncertainty is found to be 2.6 GeV. For the tagged analysis the same procedure was repeated. In this case the ensembles formed with no gluon radiation had an ensemble average of 176.0 GeV and the ensembles formed with gluon radiation had an ensemble average of 178.5 GeV. The variation from nominal is thus found to be 0.1 GeV for the events without gluon radiation and 2.4 GeV for the events with gluon radiation. Added in quadrature the total uncertainty is found to be 2.4 GeV. The two variations were then added in quadrature to yield a  $\pm 2.6$  GeV uncertainty for the topological selection and a  $\pm 2.4$  GeV uncertainty for the tagged selection.

### 8.3.3 Event Model

As in the case of gluon radiation, the number of top quark events seen in data is very small. Therefore, the model of the kinematic properties of the events is taken purely from Monte Carlo simulation. Since the Monte Carlo simulation is used to produce the templates for the mass fit, if the Monte Carlo event model is incorrect

this could lead to an uncertainty on the top quark mass measurement. In order to conservatively estimate the size of this effect, two samples were generated. The first is a Monte Carlo sample where along with  $t\bar{t}$  production an extra hard quark was produced in the sample ( $t\bar{t} + 1 \text{ jet}$ ). The second sample was generated with the underlying event (the remnants of the proton-anti-proton collision) suppressed. Specifically, the nominal Monte Carlo sample uses an underlying event model known as Tune A [85]. This underlying event model was produced using collider data to tune the Monte Carlo to best represent the soft interactions at the Tevatron. These samples were then used to form ensembles and fit using the nominal templates.

In the topological analysis the ensemble average for events with the underlying event turned off was 173.4 GeV and for the tagged analysis the average was 174.3 GeV. For the ensembles formed with an extra hard quark produced the ensemble average was 177.5 GeV in the topological analysis and 178.4 GeV in the tagged analysis. For both event selections this lead to a variation of 1.8 GeV and 2.3 GeV for the underlying event uncertainty and the  $t\bar{t} + 1 \text{ jet}$  uncertainty, respectively. Added in quadrature the total uncertainty for the signal model is found to be 3.0 GeV.

As well, a Monte Carlo sample W+jet sample was generated with a different dynamical scale. The default W+jets samples were generated using  $Q^2 = M_W^2 + \sum p_{T_j}^2$ . In order to test the dependency on this scale the alternate sample was generated with  $\sum p_{T_j}^2$ . The ensemble average was 174.5 GeV. A variation of 0.7 GeV was found forming ensembles using this sample for the background using the template with the default dynamical scale.

### 8.3.4 Trigger Bias

In order to write events to tape for further analysis, a trigger must be constructed and used to select the events online (see section 3.7). Because of the coarse nature of

the information available and the short timing budget, the objects used for the trigger are not as well understood as the objects after full event reconstruction. Hence, when one asks for an event with at least one jet with transverse energy of 15 GeV at the trigger level, not all the events containing a jet with transverse energy greater than 15 GeV will be selected. This is because the energy of the trigger level jets is not as well calibrated as jets that fully reconstructed jets offline. A simpler scale and offset for calorimeter towers at the trigger level. The algorithm at the trigger level is also more simplistic and does not capture the entire jet energy. As well, the final event yield in data is a biased sample. It is biased because in order for it to be analyzed offline at all it must have passed some trigger requirement. In the limiting case, imagine that the trigger required all events to have all jets with greater than 20 GeV transverse energy. Just looking at the final event  $p_T$  spectrum one would come to much different conclusions about the transverse momentum of the jets than if there was no requirement at all on the jets. In order to simulate the efficiency and possible bias of the trigger requirement, a probability for the Monte Carlo events was constructed [72] to pass the trigger.

This probability is calculated using the final state objects in each event and represents the best estimate of the probability of the event to pass the actual trigger that was used in data. Events were thrown out at random according to this probability. The events that survived this selection thus have the (simulated) bias that the trigger produces on data. In order to evaluate the systematic due to a possible trigger bias, a selection of events without the trigger efficiency selection was prepared. This sample was then used in ensemble tests relative to the nominal templates which were constructed using the simulated trigger efficiency. In the case of the topological analysis the ensemble average was 174.8 GeV and in the tagged analysis the 175.8 GeV. In both cases the variation is less than the statistical uncertainty on the mean value of the

ensembles  $\approx 0.5\text{GeV}$ . Conservatively, the uncertainty was taken to be the statistical uncertainty on the ensemble average as  $0.5\text{ GeV}$ .

### 8.3.5 Limited Monte Carlo Statistics

After full event selection the number of events used to construct the various templates is of the order of a few thousand. Ideally, the templates would be generated from an 'infinite' number of Monte Carlo events. In the limit of infinite statistics the templates would not have any statistical fluctuations and would represent the best estimate of what the event distribution looks like in data. Although the number of Monte Carlo events is more than an order of magnitude larger than the number of events in data, there may still be some uncertainty associated with statistical fluctuations in the templates. In order to estimate this effect, the Monte Carlo samples were split into four subsamples. One sample was used as the template while another was used to form the ensembles. This procedure was repeated through all permutations and the variation of the average ensemble mass for the different ensembles computed. For the topological analysis the four subsamples led to ensembles with averages of 175.5, 175.6, 174.9, and 174.6 GeV. The variation from the nominal value were 0.3, 0.4, 0.3, and 0.6 GeV. The uncertainty was computed as the RMS of the results for the four sets of templates divided by the square root of the number of different templates  $\sqrt{N-1}$  (e.g.  $N = 4$ ). The uncertainty was found to be 0.4 GeV. In the case of the tagged analysis the four subsamples led to ensembles with averages of 176.3, 176.4, 175.8, 175.7 GeV. The variation from the nominal values was thus found to be 0.2, 0.3, 0.3, 0.4 GeV. Calculating the uncertainty in the same way, the total uncertainty was found to be 0.3 GeV. As in the case of the systematic uncertainty associated with the trigger this was found to be less than the statistical uncertainty on the mean of the ensembles and so the uncertainty was taken to be  $0.5\text{ GeV}$ .

### 8.3.6 Calibration

Although the calibration of the method is seen to have a unit slope and close to zero offset in both cases at the template point closest to the fitted mass seen in data a slight positive bias was seen (of 0.5 GeV). Although this is most likely a statistical fluctuation, an uncertainty of 0.5 GeV was conservatively assigned to the calibration of the method.

### 8.3.7 Jet Resolution

The energy resolution of the jets in data and Monte Carlo are known to differ. In order to correct for this, the jets in Monte Carlo were smeared so that the resolution was closer to that seen in data. To understand if this introduced any uncertainty in the mass extraction the jet energy smearing was varied by  $\pm 1\sigma$ . For the ensembles where the jet energy smearing was reduced by 1  $\sigma$  the ensemble average was found to be 174.8 GeV, and when jet energy smearing was increased by 1  $\sigma$  the ensemble average was 174.4. The variation from the nominal is found to be 0.4 and 0.8 GeV. Added in quadrature the uncertainty is 0.9 GeV.

### 8.3.8 $b$ Tagging

In the tagged event selection, as discussed in section 6.4, the background is expected to be composed essentially of heavy flavor quark production in conjunction with a W boson. The heavy quarks tend to have a slightly harder  $p_T$  spectrum than the light quarks. As well, the fragmentation process is different for heavy and light quarks [84] with heavy quarks tending to form hadrons that carry most of the energy of the jet. Finally, the efficiency for the identifying the heavy quarks is strongly dependent upon the  $p_T$  and  $\eta$  of the jet. All of these lead to the fit mass distribution for W +

heavy quark events having a somewhat larger average mass as shown in Fig. 8.13. The nominal background template for the tagged analysis was taken from the combination of Monte Carlo  $W + \text{jet}$  events in the fraction that is expected from the cross-section [86] in section 6.4. In order to ascertain the uncertainty due to this assumption, Monte Carlo ensembles were formed using only  $W + \text{light flavor}$  events with a background template composed of the nominal fractions stated in section 6.4. Then ensembles using only  $W + b \text{ jets}$  were created and fit using the same background template. The ensemble average for the events composed of  $W + \text{light flavor}$  events only was 175.3 GeV and the average of the ensembles composed of events with  $W + b \text{ jets}$  was found to be 176.5 GeV. The difference between the two is 1.2 GeV which is taken to be the uncertainty associated with  $b$ -tagging.

Another approach that can be taken to estimate this uncertainty is to vary the tagging efficiency in Monte Carlo up and down by the uncertainties obtained when creating the sample for the ensemble. Similar results were found using this technique which resulted in a 0.7 GeV variation. In either case, the largest effect from  $b$  tagging is the final background composition. If the tagging efficiency were lower, less heavy flavor would be selected and more of the background would be from misidentification. If the tagging efficiency were higher, the heavy flavor fraction would be larger. The effect on the mass measurement is that the background composition would be slightly different and hence the background model slightly different as reflected in Fig. 8.13. Note that this is a very conservative approach since the expected uncertainty on the tagging methods is expected to be of the order of 10%.

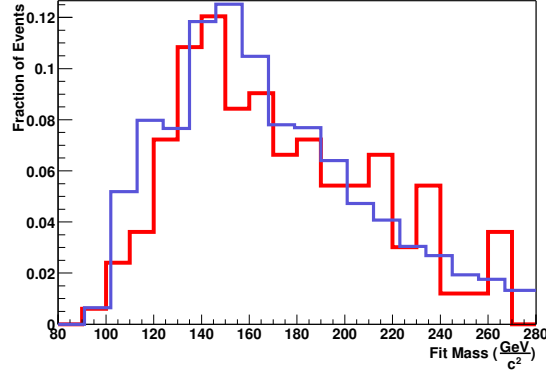


Figure 8.13: Fit mass distribution for W+light jet events (red) and W+heavy flavor (blue).

## 8.4 Systematic Uncertainty Summary

For both the topological and tagged event selection the dominant systematic uncertainty is the jet energy scale. Several other sources of uncertainty have also been considered and evaluated rather conservatively. This choice was made because the jet energy scale dominates the systematic uncertainty evaluation and represents approximately 85 % of the total systematic uncertainty (i.e. A more aggressive approach would not reduce the total systematic uncertainty by more than a few percent.)

The total systematic uncertainty for the topological selection is found to be +8.0 GeV -7.8 GeV. For the tagged event selection the total systematic uncertainty is found to be +6.3 GeV -6.8 GeV . The results are tabulated in Tables 8.4 and 8.4.

## 8.5 Cross Checks

In order to cross check the results obtained, a slightly different fitting method was used. In this case, the constraint in the likelihood function to constrain the signal fraction to that expected from the cross-section measurement was removed. In the

Source	-1 $\sigma$ (GeV)	+1 $\sigma$ (GeV)
Jet Energy Scale	6.8	6.5
Signal Model	3.0	3.0
Background Model	0.7	0.7
Gluon Radiation	2.6	2.6
Limited Monte Carlo Statistics	0.5	0.5
Trigger Bias	0.5	0.5
Calibration	0.5	0.5
Jet Resolution	0.9	0.9

Table 8.3: Summary of the Systematic Uncertainty for the Topological Selection.

Source	-1 $\sigma$ (GeV)	+1 $\sigma$ (GeV)
Jet Energy Scale	4.7	5.3
Signal Model	3.0	3.0
Background Model	0.7	0.7
Gluon Radiation	2.4	2.4
Limited Monte Carlo Statistics	0.5	0.5
Trigger Bias	0.5	0.5
Calibration	0.5	0.5
Jet Resolution	0.9	0.9
b Tagging	1.2	1.2

Table 8.4: Summary of the Systematic Uncertainty for the Tagged Selection.



tagged selection the results we find the top quark mass to be  $171.8 \pm 4.8$  GeV with  $39.9 \pm 11.6$   $t\bar{t}$  events in the sample. With the topological selection the result we determine the top quark mass to be  $170.7 \pm 6.5$  with  $40.2 \pm 13.3$   $t\bar{t}$  events. Both are within a GeV of the constrained results indicating that result is quite stable with respect to presumed signal fraction. As well, the discriminant requirement was varied from 0.25 to 0.55, the results of which are tabulated in Table 8.5. In summary the result is robust with respect to variations of the event selection and assumed signal fraction.

Discriminant Requirement	Extracted Top Mass (GeV)
0.25	$170.5 \pm 5.5$
0.3	$170.6 \pm 5.5$
0.4	$169.9 \pm 5.7$
0.45	$170.3 \pm 6.5$
0.5	$169.2 \pm 5.6$
0.55	$167.0 \pm 6.5$

Table 8.5: Fit results for variations of the topological discriminant requirement.

	Constrained	Unconstrained
Topological Analysis	$169.9 \pm 5.8$ GeV $44.2 \pm 6.6$ $t\bar{t}$	$170.7 \pm 6.5$ GeV $39.9 \pm 11.6$ $t\bar{t}$
Tagged Analysis	$170.6 \pm 4.2$ GeV $49 \pm 6.3$ $t\bar{t}$	$171.8 \pm 4.8$ GeV $40.2 \pm 13.3$ $t\bar{t}$

Table 8.6: Summary of the Fit Results with the Topological and Tagged Fit Results.

## 8.6 Events

Tables 8.7 - 8.10 list the topologically selected events that were used in the analysis and Tables 8.11 -8.12 list the events that were used in the tagged selection.

Run Number	Event Number	Discriminant	Fit Mass (GeV)	$\chi^2$
175916	2071133	0.10	116.24	4.03
178424	47233802	0.09	153.90	1.67
178466	29925637	0.85	124.57	0.678
178483	30954054	0.96	173.77	0.95
178483	35497013	0.82	167.11	3.19
175905	12730166	0.45	175.45	3.09
178151	15522349	0.45	113.90	0.31
179235	50467423	0.52	126.50	1.41
178790	34841003	0.38	224.03	7.72
179039	19461961	0.65	220.76	5.31
178721	5038322	0.38	141.48	0.18
179594	8336042	0.12	207.39	4.83
179329	588830	0.0001	291.94	4.24
178790	30505094	0.76	165.07	0.73
178788	4283453	0.60	185.38	2.08
178733	3210112	0.97	145.93	3.13
179617	15465924	0.93	172.84	1.22
178760	2636922	0.93	138.72	0.48
178841	20294830	0.30	182.48	0.64
179329	1664034	0.066	184.07	0.64
180879	13061356	0.16	173.12	0.44
179760	25881319	0.35	440.02	2.10
180081	22278985	0.29	137.66	7.98
176727	15939258	0.75	199.21	0.31
180335	51564517	0.96	180.82	1.26
177275	5302321	0.55	181.94	0.66
180081	26426003	0.34	139.34	3.02
176843	30412438	0.98	195.94	0.81
177820	11683841	0.32	137.78	0.74
178152	32384663	0.91	117.94	0.35
176988	40644379	0.38	336.71	4.94
176989	55809923	0.741	161.65	1.11
169923	16396718	0.91	144.9	0.28
175334	17307158	0.61	140.53	0.18

Table 8.7: Events in the Topological Selection.

Run Number	Event Number	Discriminant	Fit Mass (GeV)	$\chi^2$
174214	13846526	0.51	108.03	0.13
176766	12252003	0.91	146.43	0.37
176482	38905634	0.37	178.55	3.03
167010	846729	0.88	175.31	6.11
164040	19265127	0.97	278.14	1.50
164539	47070569	0.98	244.59	0.81
163529	13790415	0.53	176.28	0.87
168506	13851107	0.81	127.46	0.044
168515	23452583	0.791	165.50	1.2
168136	2215240	0.85	190.37	2.45
163101	24478983	0.75	110.60	0.16
164406	17643092	0.71	168.42	1.70
168516	26242720	0.18	242.86	0.26
175131	2179495	0.77	201.61	0.52
173079	19273915	0.14	154.73	3.79
172591	10663175	0.51	189.76	2.97
166114	41171628	0.92	111.68	2.05
166313	30859270	0.32	109.19	2.67
166830	17709325	0.31	196.24	1.23
189561	40245544	0.58	168.14	0.10
189776	861212	0.21	115.95	0.46
190088	216446693	0.37	118.18	2.87
190080	141702197	0.88	157.91	1.16
187230	68673121	0.36	194.38	1.01
188292	108971	0.66	216.08	1.12
188324	6163900	0.65	214.22	5.15
188550	63435382	0.88	167.95	0.69
188904	21333789	0.28	411.68	3.92
188904	22473727	0.92	175.92	2.24
188928	56161054	0.44	121.09	0.18
189225	7021050	0.69	140.18	0.09
189142	74154764	0.58	183.98	2.53
178369	4544113	0.12	143.73	2.43
178391	27841293	0.91	117.59	0.28
179330	5842289	0.43	136.31	1.20
178761	12992756	0.69	177.34	0.35
178733	3310651	0.51	172.13	6.26
178844	21156649	0.16	121.97	0.02
178789	25579312	0.86	178.24	0.02
179306	20691712	0.13	160.58	1.85
178733	12397624	0.54	119.43	1.32
179306	25499994	0.95	249.72	5.07
178737	43825826	0.88	153.71	3.17
180428	34042406	0.34	138.2	0.18

Table 8.8: Events in the Topological Selection- continued.

Run Number	Event Number	Discriminant	Fit Mass (GeV)	$\chi^2$
176877	33103694	0.89	170.46	1.27
176877	35121465	0.77	162.63	2.60
178107	31552930	0.19	162.73	8.18
180576	7553414	0.50	196.37	0.23
180040	9696303	0.63	175.62	1.01
177006	5154543	0.76	141.84	0.11
180426	5605678	0.70	152.99	3.0
176566	12815310	0.15	154.03	1.69
177247	16415066	0.28	110.74	1.01
179895	11393420	0.11	440.09	2.05
177247	19871976	0.81	146.42	1.97
180880	31490121	0.64	196.68	0.41
178277	37803550	0.93	101.65	6.10
176973	39850057	0.91	145.76	0.03
163063	26596120	0.28	138.44	6.42
177241	595736	0.34	134.17	1.14
173527	2211127	0.88	154.26	0.33
174424	2828736	0.41	135.0	0.81
175340	11703206	0.27	123.64	0.15
175919	52443569	0.08	140.27	8.14
175322	2093953	0.95	141.48	0.21
176677	8007381	0.54	160.44	0.81
176692	43481086	0.34	151.58	1.05
176874	7852990	0.71	130.99	0.68
175917	22961681	0.42	191.42	1.98
166530	58919354	0.50	622.30	3.19
163069	332821	0.18	113.67	0.64
163524	7542103	0.94	257.74	2.50
166532	61293520	0.65	119.11	0.75
163527	12847872	0.16	201.43	1.29
168393	820328	0.10	136.93	1.28
165899	3461139	0.26	232.58	0.36
168149	2028166	0.93	156.11	0.04
174490	840862	0.84	134.88	1.02
189361	4470667	0.97	165.44	2.14
189318	49101926	0.89	108.36	1.43
189498	56318866	0.95	194.43	0.12
189402	69996854	0.83	171.17	6.28
189393	3200782	0.16	199.23	1.35
189561	43391802	0.51	242.43	3.13
189581	9616139	0.75	137.94	1.36
189614	27058220	0.94	184.04	2.68

Table 8.9: Events in the Topological Selection- continued.

Run Number	Event Number	Discriminant	Fit Mass (GeV)	$\chi^2$
175322	6089373	0.61	142.06	2.03
174797	5863422	0.048	221.90	8.78
174495	19116262	0.02	163.80	2.78
174424	1062769	0.87	173.37	1.37
175640	16889627	0.007	253.9	1.68
175868	15280745	0.15	204.89	1.28
175326	16002373	0.46	196.99	0.70
175335	29822900	0.92	136.81	2.48
177011	49591420	0.10	247.09	4.69
177044	41432229	0.88	171.56	2.07
176875	16966764	0.81	137.30	1.23
175035	25530870	0.09	149.92	2.37
189770	28583149	0.79	243.77	0.44
190059	47479363	0.38	105.45	1.51
190087	197862239	0.28	195.79	2.43
185838	14806368	0.71	263.07	0.68
185787	11851805	0.73	178.37	2.89
190369	31963461	0.58	140.55	1.018
190365	12553715	0.38	184.29	3.57
187223	13511473	0.18	179.73	4.56
187837	17577269	0.20	140.49	2.15
188160	20774737	0.67	200.53	0.60
188298	58551412	0.48	141.39	2.87
188374	57542340	0.57	228.25	4.07
188909	71628903	0.65	174.61	2.95
188925	5787451	0.74	187.53	2.94

Table 8.10: Events in the Topological Selection- continued.

Run Number	Event Number	Discriminant	Fit Mass (GeV)	$\chi^2$	# of tags
178424	47233802	0.09	141.34	10.13	2
178483	30954054	0.96	169.26	1.13	1
178483	35497013	0.82	231.59	5.51	1
175905	12820774	0.57	126.28	0.08	1
178516	20986229	0.22	146.08	4.56	1
178790	36160717	0.06	159.64	1.55	1
178790	30505094	0.76	112.57	2.59	1
179300	7733435	0.02	157.95	218.43	1
178733	3210112	0.97	176.44	24.81	2
178760	2636922	0.93	155.92	2.071	1
179270	10328371	0.21	119.27	8.92	1
180081	22278985	0.29	170.49	14.38	1
180335	51564517	0.96	180.82	1.25	1
177275	5302321	0.55	144.87	0.86	1
178124	45583615	0.55	260.90	16.53	1
169923	16396718	0.91	149.18	0.42	1
175343	34082130	0.84	233.45	1.89	1
174424	1062769	0.87	173.37	1.37	1
175326	16002373	0.46	196.99	0.71	1
175335	29822900	0.92	136.81	2.48	1
176875	16966764	0.81	137.30	1.23	1
176766	13289995	0.19	143.32	14.63	1
176882	6025400	0.60	228.31	15.58	1
175055	23659766	0.74	188.93	33.97	1
165777	61290084	0.40	174.47	26.48	1
164040	19265127	0.97	278.12	1.50	2
164539	47070569	0.98	244.59	0.81	1
168465	4399234	0.08	247.26	1.07	1
168506	13851107	0.81	127.46	0.04	1
168515	23452583	0.79	165.50	1.2	1
168516	26242720	0.18	242.86	0.26	1
172591	10663175	0.51	189.76	2.97	1
190080	141702197	0.88	309.50	3.58	2
185868	13687332	0.92	321.30	0.32	1
188031	34878256	0.11	168.29	25.41	1
187863	48985942	0.66	150.93	0.28	1
188292	108971	0.66	216.08	1.13	1
188324	6163900	0.65	178.77	10.49	1
188550	63435382	0.88	186.60	3.06	2
188904	21333789	0.28	411.68	3.92	1
188904	22473727	0.92	175.93	2.24	1
189225	7021050	0.69	152.10	2.31	2

Table 8.11: List of the Tagged Events.

Run Number	Event Number	Discriminant	Fit Mass (GeV)	$\chi^2$	# of tags
178733	3310651	0.51	177.55	15.74	1
178789	25579312	0.86	178.24	0.02	2
179229	12874690	0.55	136.0	1.38	1
176877	33103694	0.89	194.27	13.33	2
176877	35121465	0.77	195.95	2.78	1
177006	5154543	0.76	153.73	1.38	1
176566	12815310	0.15	222.18	6.29	1
178310	11225287	0.90	205.20	0.89	1
176973	39850057	0.91	171.48	0.48	1
177034	8492167	0.78	215.43	9.4	1
173527	2211127	0.88	154.26	0.33	1
175340	11703206	0.27	123.64	0.15	1
163524	7542103	0.94	257.74	2.50	2
167003	27714859	0.90	225.35	16.16	1
189318	49101926	0.89	108.36	1.43	1
189498	56318866	0.95	170.52	0.26	2
189402	69996854	0.83	171.17	6.28	1
189614	27058220	0.94	184.04	2.68	1
189770	28583149	0.79	215.77	1.60	1
190059	47479363	0.38	126.75	1.53	1
190087	197862239	0.28	161.74	8.02	1
185787	11851805	0.73	178.37	2.90	1
187221	5035077	0.86	171.84	5.43	1
187861	14837455	0.57	212.33	26.52	1
187837	17577269	0.20	140.49	2.15	1
188298	58551412	0.48	141.40	2.87	2
188925	5787451	0.74	187.53	2.94	1

Table 8.12: List of the Tagged Events-continued.

# Chapter 9

## SUMMARY AND OUTLOOK

*'Prediction is very difficult, especially if it's about the future.'*

Niels Bohr

### 9.1 Summary

Two methods have been used to measure the mass of the top quark. This is one of the first measurements of the top quark mass made at the DØ experiment during Run II of the Tevatron. The first, based on a topological event selection, yields a result of  $m_{top} = 169.9 \pm 5.8$  (*statistical*)  $+8.0 -7.8$  (systematic) GeV with  $44.2 \pm 6.6$  top quark events. The second method, based on the identification of hadronic jets from b quarks, yields a result of  $m_{top} = 170.6 \pm 4.82$ (*statistical*)  $+6.3 - 6.8$  GeV with  $49 \pm 6.3$  top quark events. Along with being one of the first measurements during the new run, this is the first measurement to utilize the identification of b-jets to measure the top quark mass at the DØ experiment. The current world average is  $m_{top} = 178.0 \pm 4.3$  GeV. The total error on the more precise measurement presented in this thesis (with the tagged event selection) is 7.8 GeV. The measured value of the



top quark mass, while slightly lower than the world average, are completely consistent with the world average within  $0.95\sigma$ . Using all the other precision electroweak data, the current prediction from the Standard Model for the top quark mass is 178.1 GeV [2]. Obviously, the results in this thesis are consistent with the Standard Model electroweak fit as well.

## 9.2 Outlook

The outlook for the future of top quark mass measurements can be split into short term, medium term, and long term prospects. This section briefly discusses what improvements can be made to the top quark mass measurement for each of these periods.

### 9.2.1 Short Term

As of this writing, the plan is to operate the Tevatron until at least 2009. The analysis presented in this thesis was based on approximately  $230\text{ pb}^{-1}$  of data collected with the DØ detector. In the coming years, the experiment is expected to collect several inverse femto barns of data- possibly as much as  $8\text{ fb}^{-1}$ . This represents approximately 35 times the data already collected. Assuming no improvement in the event selection, so that the signal to background ratio is the same, one would expect the statistical error to scale as  $\frac{1}{\sqrt{N_{events}}}$ . The expected statistical error for  $8\text{ fb}^{-1}$  would be approximately 0.75 GeV. Compared to the current systematic error this would be essentially negligible. In this regime, the systematic error would clearly be the dominant factor. One can expect that with more photon + jet events the jet energy scale could be better understood. In addition to this, there are several other ways to improve the jet energy scale error:

- Better modeling of the detector response to decrease the difference of  $\Delta S$  between data and Monte Carlo.
- Use of track information in the jet objects.
- Reconstructing the invariant mass of resonances in the hadronic decay modes.

High momentum particles are better measured with the calorimeter as the resolution can be approximated by the formula  $\frac{\sigma_E}{E} = \frac{50\%}{\sqrt{E}}$ . On the other hand, the resolution of low momentum particles is better measured by the spectrometer formed by the silicon and fiber trackers and the solenoid magnet. The fractional resolution of the inner tracker momentum measurement is proportional to the particles' momenta.

Jets are composed of many hadronic particles of varying energy. For the work discussed in this thesis, the energy of jets was measured by the calorimeter. By using the inner tracker as well, one could use the detector that has the best resolution for the given energy range in order to more accurately measure the energies of the particles in the jet. This should lead to an improved jet resolution. Also the tracking information could be used to constrain the energy scale at low momenta where the resolution of the central tracker is more precise.

Finally, by explicitly reconstructing particles of known mass one could improve the jet energy scale. Although there is a large background, with a clever trigger one should be able to extract the  $Z \rightarrow b\bar{b}$  [94]. Heintz and Narain have shown that after background subtraction, one could fit the invariant mass spectrum for  $Z \rightarrow b\bar{b}$  to potentially reduce the jet energy scale error to  $\frac{1}{3}\%$  leading to a four fold reduction in the jet energy scale error on the top quark mass measurement [94].

In the data set used for this analysis, there are only 12 events which have two jets identified as coming from b quarks. With an increase in the data set size, one could expect this number to be close to  $\approx 500$  events (assuming no improvements in

tagging efficiency or event selection). With two jets identified as b jets, there are only two jet permutations. Hence, in principle, the invariant mass of the two untagged jets should reconstruct to the mass of the W boson. With a large number of double tagged events, one could consider relaxing the constraint that two jets should reconstruct to the invariant mass of the W and use the data to constrain the jet energy scale.

With other improvements such as an increase in the Monte Carlo statistics (more template points), a better understood background model (by identifying W+heavy and W+light flavor in data and constraining the Monte Carlo simulation to match the data) most other systematic errors could be significantly reduced. With a larger number of events, the properties of gluon jets could be better understood and hence the effect of their presence on the top quark mass measurement reduced. Estimates have been made that the total systematic error could be reduced to 1.0 GeV - 2.0 GeV [94]. Depending on the accuracy achieved one could then expect the total error on the top quark mass to be reduced to 2.0 GeV at the Tevatron.

## 9.2.2 Intermediate Term

Even at the highest luminosities achievable at the Tevatron, the number of top quark events passing all event requirements will be on the order of a few thousand. This is simply a consequence of cross-section for  $t\bar{t}$  production at the center-of-mass energy at which the Tevatron operates. The Large Hadron Collider (LHC) is the next generation hadron collider with a center of mass energy of 14 TeV. Next-to-Leading order calculations estimate the  $t\bar{t}$  cross-section to be around 833 pb [95]. Because of this greatly enhanced cross-section, the LHC will produce several million  $t\bar{t}$  events per year. Using selection criteria similar to that presented in this thesis, one could expect almost 100,000 lepton + jet events with  $10fb^{-1}$  of data [96]. Even requiring two jets to be identified as b-jets, the statistics are (with respect to the number

of top quark candidate events in the work presented here) quite staggering, with an estimated 30,000 double tagged events per year. For these experiments, clearly the challenge will be in understanding the systematics. Although the statistical error is utterly negligible, systematic errors from gluon radiation and the jet energy scale are expected to limit the precision to about 1.0 GeV [96].

### 9.2.3 Long Term

The most precise measurements made at collider experiments are typically made at electron-positron machines. With an electron-positron collider one does not need to worry about the complicated structure of the particles that are colliding. In particular, if an electron-positron linear collider with a center-of-mass energy large enough to produce  $t\bar{t}$  pairs were built many of the underlying systematic issues associated with hadron machines would not be present. Most notably there would be no underlying event, initial state gluon radiation, or parton distribution functions (all the energy of the electron and positron would be in the hard scattering event). As mentioned in chapter 2, the top quark is heavy enough that it decays before it has time to hadronize. At an electron-positron collider the cross-section,  $\sigma(e^+e^-) \rightarrow t\bar{t}$ , near threshold is expected to rise at the center-of-mass energy where the lowest bound state of the top-anti-top meson would have been formed [13]. The value for the mass of the top quark determines the location of this threshold. It is believed that from the line-shape near threshold one could extract the top quark mass with a precision on the order of 150 MeV [97], [98]. Finally, if a  $\mu^+\mu^-$  collider were to be built the same technique could be applied. Because of the relatively larger mass of the muon, a muon collider is expected to have negligible amounts of 'Beamstrahlung'. 'Beamstrahlung' is the emission of radiation by one beam due to the effective magnetic field of the other beam. The absence of this at a muon collider is expected to increase the precision of

the location of the rise of the  $t\bar{t}$  cross section in the threshold region. Potentially, a measurement of the top quark mass could be made with a precision on the order of a hundred MeV [99]. However, our current understanding of the strong interactions place a 'theoretical error' on the relationship between the pole mass of the quark and the mass measured by the line shape on the order of 100-200 MeV [100].

# Bibliography

- [1] S.L. Glashow, *Nucl. Phys.*, **22**,579 (1961); S. Weinberg, *Phys. Rev. Lett.* **19** 1264 (1967); A. Salam, Elementary Particle Theory, ed. N Svarholm (Almquist and Wiksells, Stockholm) p.367 (1969).
- [2] LEP Electroweak Working Group, <http://lepewwg.web.cern.ch/LEPEWWG/> (2004).
- [3] Chris Quigg. *Gauge Theories of the Strong, Weak, and Electromagnetic Interactions*. Addison-Wesley (1983).
- [4] Gordon L. Kane. *Modern Elementary Particle Physics*. Addison-Wesley, (1993) Updated Edition.
- [5] Peskin and Schroeder. *An Introduction to Quantum Field Theory*. Westview Press (1995).
- [6] Particle Data Group, Review of Particle Physics, *Particle Physics B* **592**, 246 (2004).
- [7] The Super Kamiokande Collaboration, Evidence for Oscillations of Atmospheric Neutrinos, *Phys. Rev. Letter* **81**, 1562-1567 (1998).
- [8] N. Arkani-Hamed, S. Dimopoulos, G. Dvali, The Hierarchy Problem and New Dimensions at a Millimeter, *Phys. Lett. B* **436**, 257 (1998).

- [9] Scott Willenbrock, The Standard Model and the Top Quark, *hep-ph 0211067*, (2002).
- [10] I. Efthymiopolous, M.L. Mangano, J. Womersley, et. all, Top Quark Physics, *CERN Workshop on Standard Model Physics (and more) at the LHC*, (1999).
- [11] D. Chakraborty, J. Konigsberg, D. Rainwater, Review of Top Quark Physics, *Ann Rev Nucl Part Sci*, **53**, 301-351, (2003).
- [12] S. Dawson, SUSY and such, *hep-ph 9712464*, (1997).
- [13] E. Simmons, The Top Quark: Experimental Roots and Branches of Theory, *hep-ph 0211335*, (2002).
- [14] P. Chankowski, S. Pokorski, and J. Rosiek, Charged and neutral supersymmetric Higgs boson masses. Complete one-loop analysis, *Phys. Lett. B*, **274**, 191, (1992).
- [15] S. Weinberg, Implications of dynamical symmetry breaking: An addendum, *Phys. Rev D*, **19**, 1277 (1979).
- [16] E. Eichten and K. Lane, Dynamical breaking of weak interaction symmetries, *Phys. Lett B*, **90** 125 (1980).
- [17] K. Lane, Two Lectures on Technicolor, *ph-0202255*, (2002).
- [18] C.T. Hill, M. A. Luty, and E. A. Paschos, Electroweak symmetry breaking by fourth-generation condensates and the neutrino spectrum, *Phys. Rev. D*. **43** 1647-1660 (1990).
- [19] J. Pumplin et. all, New Generation of Parton Distributions with Uncertainties from Global QCD Analysis, *hep-ph 0201195*, (2002).

- [20] R. Bociani, S. Catani, M. L. Mangano and P. Nason, 'NLL resummation of heavy-quark hadroproduction', *Nucl. Phys. B* **529**, 424 (1998).
- [21] Gordon L. Kane. Top quark topics. Gauge Bosons and Heavy Quarks: Proceedings of the Eighteenth SLAC Summer Institute on Particle Physics, pages 123–142. *SLAC-REPORT-378* (1990).
- [22] M. L. Mangano, M. Moretti, and R. Pittau, ALPGEN, a generator for hard multiparton processes in hadronic collisions, *ph-0206293*, (2003).
- [23] S. Abachi *et al.*, Observation of the Top Quark, *Phys. Rev. Letters*, **74**, 2632 (1995).
- [24] F. Abe *et al.*, Observation of Top Quark Production in p anti-p Collisions with the Collider Detector at FermiLab, *Phys. Rev. Letters*, **74**, 2626 (1995).
- [25] S. Abachi *et al.*, Direct Measurement of the Top Quark Mass, *Phys. Rev. Letters*, **79**, 1197, (1997).
- [26] F. Abe *et al.*, Measurement of the Top Quark Mass with the Collider Detector, *Phys. Rev. Letters*, **82**, 271 (1999).
- [27] F. Abe *et al.*, Measurement of the Top Quark Mass with the Collider Detector at FermiLab, *Phys. Rev D*, **63**, (2001).
- [28] F. Abe *et al.*, Measurement of the Top Quark Mass, *Phys. Rev. Letters*, **80**, 2707 (1998).
- [29] S. Abachi *et al.*, Measurement of the Top Quark Mass using Dilepton Events, *Phys. Rev. Letters*, **80**, 2063 (1998).



- [30] V.M. Abazov *et al.*, Direct Measurement of the Top Quark Mass in All-Jet Events, to be published in *Phys Rev. D*.
- [31] V.M. Abazov *et al.*, An Improved Measurement of the Top Quark Mass, *Nature*, **429** (2004).
- [32] The Tevatron Electroweak Working group, <http://tevewwg.fnal.gov/top/> (2004).
- [33] T. Cole *et al.* *Design report, superconducting accelerator*. Technical report, Fermi National Accelerator Laboratory (1979).
- [34] Joey Thompson. Introduction to colliding beams at fermilab. Technical report, FermiLab TM-1909 (1994).
- [35] C.W. Schmidt and C.D. Curtis, A 50 mA Negative Hydrogen-Ion Source, *IEEE Transactions on Nuclear Science* **NS-26**, 4120 (1979).
- [36] D. Patterson. *The FNAL Linac*. Technical report, Fermi National Accelerator Laboratory, Internal Note (unpublished) (1986).
- [37] C.D. Curtis *et al.*, Linac H-Beam Operation and Uses at FermiLab, *IEEE Transactions on Nuclear Science*, **NS-26**, 3760 (1979).
- [38] E.L. Hubbard *et al.* *Booster synchrotron*. Technical report, Fermilab TM-405 (1973).
- [39] C.S. Mishra. *The Fermilab Main Injector*. Technical report, Fermilab Conf-92/372 (1992).
- [40] *Design Report, Tevatron 1 Project*. Technical report, Fermi National Accelerator Lab, internal note, (1984).

- [41] S. Abachi *et al.*, The DØ Detector, *Nuclear Instruments and Methods* **A338**, 185 (1994).
- [42] The DØ Upgrade Collaboration. *DØ silicon tracker technical design report*. Technical report, FermiLab, (1994).
- [43] The DØ Upgrade Collaboration. *The DØ upgrade central fiber tracker*. Technical report, FermiLab, (1999).
- [44] The DØ Upgrade Collaboration. *Conceptual Design of a 2 Tesla Superconducting Solenoid for the Fermilab DØ Detector Upgrade*. Technical report, Fermilab (1994).
- [45] The DØ Upgrade Collaboration, *Design Report of the Central Preshower for the DØ Detector*, DØ Note 3104 (1996).
- [46] The DØ Upgrade Collaboration. *Technical Design of the Central Muon System* Technical Report, Fermilab, (1998).
- [47] The DØ Upgrade Collaboration. *Technical Design Report for the DØ Forward Trigger Scintillation Counters* Technical Report, Fermilab, (1997).
- [48] J. Blazey, *The DØ Run II Trigger* Technical Report, Fermilab (1999).
- [49] H. Evans *et. al* *A Silicon Track Trigger for the DØ Experiment in Run II - Technical Design Report* Technical Report, FermiLab, (1998).
- [50] R. Angstadt, The DZERO Data Acquisition System, *IEEE Transactions on Nuclear Science*, **51**, No 3, (2004).

- [51] R. Illingsworth, *Development of Trigger Software for the Silicon and Fiber Trackers and a study of B meson lifetimes for the DØ experiment*, Ph.D Thesis, Imperial College, London (2002).
- [52] O. Boeriu, M. Hildreth, S. Jabeen, *CFT Light Yield Studies*, DØ Note 4602, (2004).
- [53] A. Khanov, *HTF: histograming method for finding tracks. The algorithm description.*, DØ Note 3778 (2000).
- [54] G. Borrisov, *Technical Details of AA Tracking*, FermiLab, to be made a DØ technical note.
- [55] The DØ Collaboration, *Beam Tests of the DØ Uranium Liquid Argon End Cap Calorimeters*, Nucl. Instr. and Methods, A324, 53 (1993).
- [56] E. Varnes, *Measurement of the Top Quark Mass at DØ Experiment*, Ph.D. Thesis, U.C. Berkeley (1997).
- [57] G. Alvarez, *Beauty at DØ*, Ph.D. Thesis, Indiana University (1996).
- [58] C. Luo, *Muon Reconstruction and B Physics Studies at the Tevatron Collider Experiment DØ*, Ph.D. Thesis, Indiana University (2003).
- [59] O. Peters, *Muon Segment Reconstruction: A Linked List Algorithm*, DØ Note 3901 (2001).
- [60] L. Chevalier *et. al.*, *Track Parameter Error Matrix Propagation in Matter and Magnetic Fields, Error Matrices Combination*, DØ Preliminary (2001).
- [61] A. Schwartzman and M. Narain, *Primary Vertex Selection*, DØNote 3906 (2001).

- [62] A. Garcia-Bellido *et. al.* *Primary Vertex certification in p14*, DØNote 4320 (2004).
- [63] A. Schwartzman and M. Narain *Probabilistic Primary Vertex Reconstruction*, DØNote 4025 (2004).
- [64] J. Kozminski *et al.*, *Electron Likelihood in P14*, DØ Note 4449, (2004).
- [65] L. Phaf and D. Whiteson, *Electron Likelihood*, DØ Note 4184 (2003).
- [66] G. Steinbruk, *Measurement of the Angular Distribution of Electrons from W boson decays at DØ*, Ph.D Thesis, University of Oklahoma (1999).
- [67] Top Production Group, *Measuement of the  $t\bar{t}$  Production Cross-section at  $\sqrt{s} = 1.96$  TeV in the Lepton + jets Final State using a Topological Method*, DØ Note 4419 (2004).
- [68] C. Clement *et. al.*, *Muon Certificaton for p14*, DØ Note 4350 (2004).
- [69] U. Bassler and G. Bernardi, *Towards a Coherent Treatment of Calorimetric Energies: Missing Transverse Energy, Jets, E.M. Objects and the T42 Algorithm*, DØ Note 4124 (2003).
- [70] G. Blazey *et. al.*, *Run II Jet Physics*, DØNote 3750 (2000).
- [71] G. Davis, *First Measurement of the Differential Inclusive Cross Section for Jet Production at DØ Run II*, Ph.D Thesis, University of Rochester (2004).
- [72] M. Angelou, *DØ Top Analysis and Data Sample for the Winter Conference 2004*, DØNote 4419 (2004).
- [73] A. Schwartzman and M. Narain *b-quark jet identification via Secondary Vertex Reconstruction*, DØNote 4080.

- [74] L. Feligioni *et. al.*, *Update on b-quark jet identification with Secondary Vertex reconstruction using DOREco version p14*, DØ Note 4414, (2004).
- [75] T. Sjostrand, L. Lonnblad, S. Mrenna, *PYTHIA 6.2 Physics and Manual*, hep-ph 0108264 (2004).
- [76] S. Jadach, Z. Was, R. Decker, and J.H. Kuhn, *The tau decay library Tauola: version 2.4* Comput. Phys. Commun. **76** , 361 (1993).
- [77] D. Lange, A. Ryd et al., *The EvtGen Event Generator Package*, in Proceedings of CHEP (1998).
- [78] D. Stump et al. *Inclusive Jet Production, Parton Distributions, and the Search for New Physics*, MSU-HEP-030303, hep-ph 0303013 (2003).
- [79] CERN. *Detector Description and Simulation Tool*, CERN Program Library Number Q123.(1993).
- [80] R. Raja, Q. Li, and S. Kunori. *DØGEANT*, DØ Note 1007, (1990).
- [81] Y. Fisyak, J. Womersley, *DØgstar: DØGEANT Simulation of the Total Apparatus Response*, DØ Note 3191, (1997).
- [82] DØ Top Production Group, *Measurement of the  $t\bar{t}$  Production Cross-Section at  $\sqrt{s} = 1.96$  TeV in the Lepton+Jets Final State Using a Topological Measurement*, to be submitted to PRL.
- [83] M. Strovink, *Details of Run 1 "Top Likelihood" Estimation for Top Quark Mass Analysis in the Lepton+Jets Channel* , DØ Note 3989, (2002).
- [84] V. Barger and R. Phillips *Collider Physics*, Addison-Wesley, NY, (1987).

- [85] R.D. Field, *Sources of  $b$  Quarks at the Tevatron and Their Correlations*, Phys. Rev. D **65**, 094006 (2002).
- [86] The DØCollaboration, *Measurement of the  $t\bar{t}$  Production Cross-Section in  $p\bar{p}$  Collisions at  $\sqrt{s} = 1.96$  TeV Using  $b$ -tagged lepton + jet events*, DØ Conference Note 4565, August 2004.
- [87] J. Kvita, *Effects of Top Quark and  $W$  Boson Finite Width on the Measurement on the Top Quark Mass*, Diploma Thesis, Charles University, Czech Republic (2003).
- [88] S. Snyder, *Measurement of the Top Quark mass at DØ* Doctoral Thesis, State University at Stony Brook, NY, (1995).
- [89] O. I. Dahl, T. B. Day, F. T. Solmitz, and N. L. Gould. *SQUAW kinematic fitting program*. Technical Report P-126, Lawrence Radiation Laboratory, Berkeley, California, (1968).
- [90] C. Macesanu, L. H. Orr, *Gluon Radiation and in Top Production and Decay*, hep-ph 0001138 (1999).
- [91] C. Macesanu, L. H. Orr, *Gluon Radiation and in Top Production and Decay*, Phys. Rev. D. **65** (2002).
- [92] L.H. Orr, T. Andre, and T. Stelzer, *Gluon Radiation in Top Mass Reconstruction: Effect of Hadronic  $W$  Decays*, hep-ph 9811424 (1998).
- [93] F. James. *Minimization Package Reference Manual*, CERN Program Library Number D506 (1994).
- [94] U. Heintz, M. Narain, *Observability of the Decay  $Z \rightarrow b\bar{b}$  in Run II*, DØ note 3604 (1999).

- [95] R. Bonciani et al., Nucl. Phys. B **529**, 424 (1998).
- [96] I. Borjanovic et al., *Investigation of top mass measurements with the ATLAS detector at LHC*, hep-ex 0403021 (2004).
- [97] S. Heinemeyer et al., *Physics Impact of a Precise Determination of the Top Quark Mass at an  $e^+e^-$  Linear collider*, hep-ph 0306181.
- [98] A.H. Hoang et al., *Top-Antitop Pair Production close to Threshold: Synopsis of recent NNLO Results*, hep-ph 0001286 .
- [99] M.S. Berger and B.L. Winer, *Top Quark Physics at Muon and other Future Coliders*, hep-ph 9802296 (1998).
- [100] J.L. Lopez, *Theoretical expectations for the top-quark mass*, hep-ph 9408279 (1994).